CHALMERS
UNIVERSITY OF TECHNOLOGY

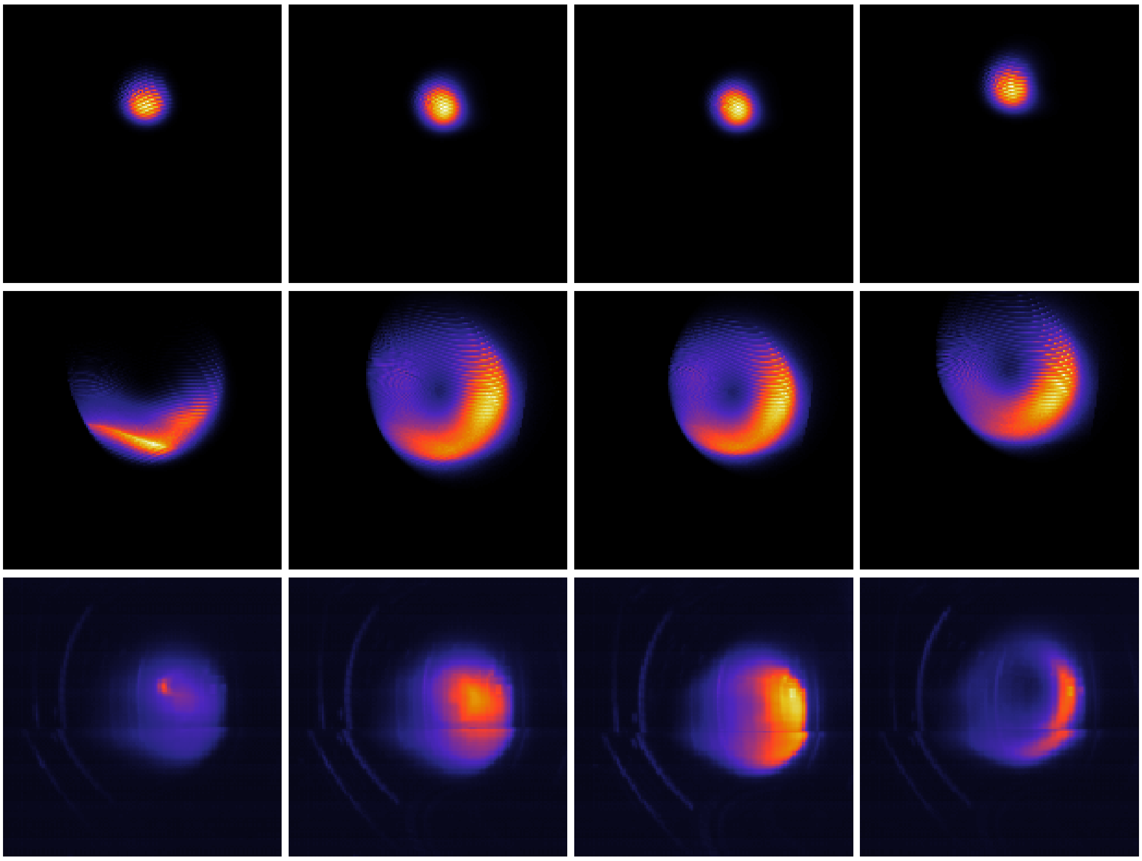

Spatio-temporal analysis of runaway electrons in a JET disruption with material injection

Thesis for the degree of Master of Science in Physics

BOEL BRANDSTRÖM

Department of Physics
CHALMERS UNIVERSITY OF TECHNOLOGY
Gothenburg, Sweden 2021

MASTER'S THESIS 2021

Spatio-temporal analysis of runaway electrons in a JET disruption with material injection

BOEL BRANDSTRÖM

CHALMERS
UNIVERSITY OF TECHNOLOGY

Department of Physics
Division of Subatomic, High Energy and Plasma Physics
CHALMERS UNIVERSITY OF TECHNOLOGY
Gothenburg, Sweden 2021

Spatio-temporal analysis of runaway electrons in a JET disruption with material injection
BOEL BRANDSTRÖM

Supervisor: Mathias Hoppe, Department of Physics
Examiner: Tünde Fülöp, Department of Physics

Master's Thesis 2021
Department of Physics
Division of Subatomic, High Energy and Plasma Physics
Chalmers University of Technology
SE-412 96 Gothenburg
Telephone +46 31 772 1000

Cover: synthetic synchrotron images from JET discharge #95135 generated with SOFT (top two rows) shown together with the corresponding experimental synchrotron images (bottom row).

Typeset in LaTeX
Printed by Chalmers Reproservice
Gothenburg, Sweden 2021

Title
Spatio-temporal analysis of runaway electrons in a JET disruption with material injection
BOEL BRANDSTRÖM
Department of Physics Chalmers University of Technology

Abstract

One of the outstanding issues of the tokamak, the magnetic confinement device on the forefront of fusion energy research, is that of relativistic electrons (so called runaway electrons) generated during disruption events. These energetic particles may cause significant damage to plasma-facing components if they escape confinement on a short timescale, and pose an even bigger threat to the next-generation tokamaks with larger toroidal plasma currents (such as ITER), since the runaway electron generation is exponentially sensitive to the plasma current in the tokamak. The runaway electron dynamics depend on a large variety of parameters, but current machines only have access to a small region of that parameter space. Numerical modeling of disruptions allows us to bridge the gap between what we have learned from present day machines and how their successors will behave. Such numerical models must be validated against available experimental data.

In this thesis, an argon gas injection induced disruption in the Joint European Torus (JET) was modeled with the kinetic equation numerical solver DREAM. With a thermal quench model where the temperature decay was assumed to be instantaneous and a runaway seed was prescribed, DREAM was able to reproduce the plasma current evolution through the disruption. DREAM allowed for simulations with a conducting wall, enabling us to reproduce the net increase in total plasma current seen after the current quench in the experimental data. Coupling the output from DREAM to the synthetic synchrotron diagnostic tool SOFT gave synthetic synchrotron signals from the modeled discharge.

To investigate the effect of the radial distribution of the runaways on the plasma current dynamics and resulting synchrotron images, the disruption was modeled two times in DREAM: once with a runaway density profile which was peaked around the magnetic axis, and once with a 'hollow' density profile with its maximum close to the plasma edge.

Comparisons of the experimental and simulated diagnostic signals allowed us to conclude that different qualitative features of the experimental synchrotron images could be reproduced with the two respective runaway seeds, indicating that in the experiment, the runaway population was radially redistributed as the disruption progressed.

Keywords: nuclear fusion, runaway electrons, numerical modeling, tokamak, Joint European Torus, disruption, synchrotron radiation

Acknowledgements

First and foremost I would like to thank Tünde Fülöp, who for almost two years has been a tireless supporter (and enabler) of my dream to be involved in fusion research. I have also been fortunate enough to have had my work supervised by Mathias Hoppe, who has not only internalized all of Stack Exchange and written much of the software upon which the work in my thesis is based, but also known the answer to pretty much every question I have asked; he has with endless patience and enthusiasm guided me through both runaway theory and computer issues. I would also like to thank to István Pusztai, who did not only spend part of his summer as my private tutor in plasma physics, but has also proofread my thesis. A special thanks to Ola Embreus for the many hours he spent remotely troubleshooting my simulations, and for providing insight into simulation results. To the other members, past and present, of the plasma theory research group at Chalmers not mentioned by name: thank you for providing a warm and supportive working environment!

This thesis would not be what it is without Alex Tinguely, who has both given invaluable feedback on the text and helped me acquire experimental data, and who has also shown great interest for my work since the very beginning.

Finally, I would like to thank my parents and my sisters for patiently listening to me rant about things firmly outside their sphere of interest during these last five years, and for a lifetime of love, support and good advice.

This work has been carried out within the framework of the EUROfusion Consortium and has received funding from the Euratom research and training programme 2014-2018 and 2019-2020 under grant agreement No 633053. The views and opinions expressed herein do not necessarily reflect those of the European Commission.

Boel Brandström, Gothenburg, June 2021

Contents

1
Introduction

Today, there can be little doubt that mankind is charging head first into what is likely to become one of its largest crises yet. Rising global temperatures are melting ice caps, changing seasons and threaten to launch a chain of irrevocable events which would most likely change the world we live in beyond recognition. Researchers have even expressed concerns about the onset of the sixth mass extinction [1, 2]—an event that entails the eradication of millions of species as natural habitats and the delicate balance of ecosystems are thrown onto the ever consuming fire of humanity's hunger for resources. We cannot know for sure how the globe's changing climate will impact human existence, but there is no doubt that this condition is one we caused ourselves [3]. The issue of climate change is further complicated by society's dependence on cheap and readily available energy; we burn oil, coal and gas to warm our houses, fuel our factories and to power the technology we have become reliant on. Removing fossil fuels from the equation without a replacement source of energy would likely cause tremendous suffering and loss of life worldwide.

Arguably, the fact that humans are responsible for the greenhouse effect has been public knowledge since at least the late 1980's [4, 5], but the dream of clean and cheap energy is older than that. Fission energy, where a heavy atomic nucleus is split to yield two lighter nuclei, free neutrons and excess energy which can be used to generate power, is evidence of this. It was first commercialized in 1956, when Calder Hall nuclear power station in the UK was connected to the public grid. Today, fission power still stands for a significant portion of the energy production in many countries—during 2020, 30% of Sweden's energy production originated from nuclear fission [6].

Over the last decade, technologies such as solar panels and wind turbines have become more affordable: the cost of solar photovoltaic electricity decreased by 82% between 2010 and 2019, while the cost of electricity from onshore wind decreased by 47% during the same period of time [7]. Despite this, sources of sustainable energy[1] only represented just below 11% of the world's total energy production in 2018 [8].

Before technologies like solar panels and wind turbines can serve as viable replacements for fossil fuels, there are substantial issues which must be amended. One of these issues is that of energy production vs. demand; as long as the wind blows and the sun shines when the electricity is needed, solar panels and wind turbines are excellent sources of energy, but what about cold, dark winter afternoons in Sweden when energy use surges? Today, Sweden responds to such temporary increases in energy consumption by importing electricity from Europe, or by starting up fossil

[1] In Ref. [8], these energy sources are solar, wind, geothermal, hydro and biomass.

fuel plants which are usually idle. It is reasonable to assume that the occasional and sudden need for on-demand energy will not subside in the future. Fossil fuels have given us the opportunity to tailor energy production to our needs, but the cost has been grave. The need for clean, reliable and readily available sources of energy remains.

Nuclear fission allows for power production without greenhouse gas emissions, but splitting the atom has not only provided us with carbon free energy. It has also resulted in a number of serious accidents (notably the Chernobyl disaster in 1986 and the Fukushima Daiichi nuclear disaster in 2011) and vast amounts of radioactive waste—some of which will be harmful to living creatures for tens of thousands of years. However, this is not the full story of the elusive atom. Nuclear fission might not be the remedy to our energy issues, but what about nuclear *fusion*?

Nuclear fusion, where light nuclei are fused together into heavier elements, has tremendous potential to become the clean source of energy the world sorely needs; powerful enough to fuel the stars above us, the fusion process is free of greenhouse gas emissions and does not produce long lived radioactive waste. The most well known and well researched concept for nuclear fusion for power production purposes is the so called *tokamak*, a device where the fusion plasma is contained inside a toroidal vacuum chamber by strong magnetic fields. A strong toroidal (long way around the torus) plasma current provides a necessary poloidal (short way around the torus) 'twist' to the otherwise predominantly toroidal magnetic field, so that the charged particles in the plasma cannot escape their magnetic cage. Although the confinement concept of a tokamak is easy to grasp, reliable and continuous containment of fusion plasmas by magnetic fields has proven to be highly complex. So far, no tokamak (or any other magnetic confinement device) has reached the much coveted *breakeven*—the point where the output power produced in the fusion process is greater than the input power needed to heat and control the plasma.

As the fusion plasma confinement concept that has come closest to reaching breakeven, the tokamak holds significant promise as a means of achieving commercial fusion power plants, but it is not without issues. One of the major hurdles are so-called *disruptions*, when plasma control is lost in such a way that the energy content of the plasma is released to plasma facing components or to the machine walls. During a disruption, the plasma temperature rapidly drops. This increases the resistivity of the plasma, which in turn leads to a decrease of the plasma current. The decaying current induces a large electric field that is capable of accelerating the electrons in the plasma to relativistic speeds. Such electrons are known as *runaway electrons* (or simply runaways). Runaways can carry significant amounts of energy, and if this energy is deposited to plasma facing components on a short timescale, it can cause devastating damage. For fusion via magnetic confinement in tokamaks to be a viable option for reliable power production, the potentially disastrous runaways must be dealt with: their energy must either be safely dispersed or their formation avoided altogether. In next generation tokamaks with larger toroidal plasma currents (like ITER, currently under construction in France through an international collaboration), runaways will be an even bigger issue since the generation of the energetic particles is exponentially sensitive to the plasma current [9]. A lot of effort is currently going into developing strategies for runaway mitigation; numerical modeling of disruption scenarios can be used as a means to bridge the gap between data from existing experiments and the behavior of machines that are planned or under construction. It also offers means of benchmarking theories and models against experimental results, and gaining deeper insight into disruption dynamics.

In this thesis, we model a disruption in the JET (Joint European Torus) tokamak in order to validate the state of the art modeling tool Dream. Dream is capable of self-consistent modeling of many plasma quantities—including the runaway electrons—during tokamak disruptions. Furthermore, by coupling output from Dream to the synthetic synchrotron radiation diagnostic tool Soft, we obtain synthetic synchrotron radiation—the radiation emitted by runaway electrons in a tokamak—diagnostic signals. Together, Dream and Soft provide us with a number of signals we can compare to the experimental data from the JET discharge in question.

1.1 Thesis outline

In this thesis, we model the argon gas induced disruption in JET discharge #95135 with the numerical tool Dream [10]—a self-consistent kinetic equation solver also capable of fluid modeling. By doing so, we aim to validate the physics models used in Dream against experimental data. A novel feature of Dream is the inclusion of a conducting wall in the simulations; the effect of this conducting wall on the plasma current dynamics will also be investigated. Output from Dream is coupled to the synthetic synchrotron radiation diagnostic tool Soft [11], which provides synthetic synchrotron radiation diagnostic signals which can be compared to experimental synchrotron radiation data. Using Soft, we can also see the effect of the radial distribution of the runaway electron population on the synchrotron radiation diagnostic signals.

This chapter introduces the principles of nuclear fusion (Section 1.2) and the basics of the tokamak (Section 1.3). Chapter 2 provides an introduction to the necessary physics concepts, starting with some fundamental plasma physics in Section 2.1. In Section 2.2, particle trajectories in tokamaks are treated, and in Section 2.3 disruptions in tokamaks are discussed. Section 2.4 deals with runaway electrons, while the kinetic theory necessary to capture the momentum dynamics of the relativistic particles is introduced in Section 2.5.

After establishing the necessary foundation of plasma physics, we move on to the numerical tools Dream and Soft. These are presented in Chapter 3; first Dream and its underlying physics models are introduced in Section 3.1, and then we give Soft a similar treatment in Section 3.2.

Chapter 4 begins by presenting the experimental data from JET discharge #95135 in Section 4.1. After this, the procedures used to simulate the disruption in Dream and Soft are presented in Section 4.2, while Section 4.3 presents the results from these simulations.

In Chapter 5 we investigate how the assumptions and parameters used in the simulations impacts the resulting data, and in Chapter 6 the conclusions of this work are presented.

1.2 Nuclear fusion

Nuclear fusion, as rare as it is here on Earth, is a common feature on the cosmic scale, fuelling the billions upon billions of stars in the universe. It is no trivial task, however, to get atomic nuclei to fuse together. The atoms must be heated to thermonuclear temperatures—at which they will have been ionized into a plasma—while a high enough density must be maintained for a sufficiently long time for the fusion reaction to take place. In a star, the high temperature—around 1 keV or 1.16×10^7 K in the core of our own Sun—in combination with immense gravitational force from the mass of the star itself sustain the necessary circumstances. But even under these conditions, the probability of two atoms fusing together is low: in the Sun, hydrogen nuclei can live for a million years before they fuse into helium [12], releasing excess energy as they do so.

Humanity cannot wait millions of years for energy. Instead, we must either raise the temperature of the fuel to well over 10 keV (corresponding to 1.16×10^8 K), or in some other way increase the inertia of two colliding ions enough for them to overcome their respective electrostatic potential barriers. We also do not have the luxury of letting gravity confine our fusion plasma for us, and so we need to find other ways to maintain the necessary conditions. For fusion power generation in tokamaks, the goal is to fuse together nuclei in a plasma consisting of 50% deuterium (D) and 50% tritium (T) yielding an α-particle (a ^{4}He nucleus), a neutron and net energy [12]:

$$\mathrm{D} + \mathrm{T} \rightarrow \alpha + n + 17.6\ \mathrm{MeV}.$$

At the temperatures currently achievable in magnetically confined plasmas here on Earth, the fusion reaction between deuterium and tritium is much more likely to occur than such a reaction between any other combination of elements or isotopes; this is why deuterium and tritium are currently the primary fuel candidates for future fusion power plants.

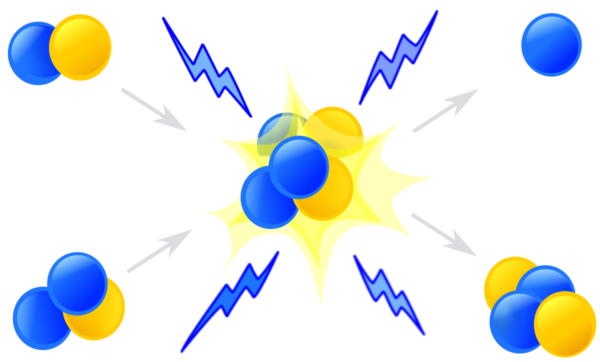

Figure 1.1: A fusion reaction between deuterium and tritium. The neutrons are depicted in blue.

Confining the fusion plasma is one of the largest obstacles between us and clean energy, but the benefits, should we succeed, are numerous. The fuel intended to power future fusion reactors is very energy dense (1500 kg of a fifty-fifty mixture of D-T would be enough to provide Sweden with all the energy it consumed during 2020 [6]), there is no long lived radioactive waste to deal with, and the operation of fusion reactors will be inherently safe: as opposed to fission reactors, there is no risk of a chain reaction causing a meltdown.

During the last seven decades, great efforts have gone in to researching different methods for confinement of fusion plasmas here on Earth. The so far most well researched and successful method for production of controlled fusion power is achieved via magnetic confinement in devices known as *tokamaks*.

1.3 Tokamaks

At the temperatures required for fusion, the atoms that are to be fused together are ionized: the electrons have separated from their nuclei and together they form a plasma. Since the constituent particles of this plasma are charged, they can be confined by a magnetic field. The particle trajectories will closely follow the magnetic field lines, implying that as long as said field lines are confined to a finite volume, the particles will be trapped. This is the idea behind toroidal magnetic confinement devices, in which the plasma is confined in a toroidal (doughnut shaped) magnetic configuration by strong magnetic fields.

In a toroidal magnetic confinement device, a purely toroidal magnetic field is not enough: due to the configuration of the magnetic field, a field strength gradient arises. The result is a weaker magnetic field on the outboard side of the torus—the low-field side (LFS)—while the field strength grows closer to the axis of symmetry, the high-field side (HFS). This field gradient causes a drift in the particle trajectories. Adding to this effect is the curvature of the device: the centrifugal forces felt by the particles as they travel around the torus cause their trajectories to deviate from the magnetic field lines. Unfortunately, these two drifts add up, and if left unchecked, they lead to a deconfinement of the plasma. This is bad news for those hoping to create a star on Earth, but luckily there is a remedy. By twisting the magnetic field slightly in the poloidal direction, the drifts can be counteracted and the particles kept in place. There are different approaches to accomplishing this twist: *stellarators* (such as the Wendelstein 7-X in Germany) use magnetic coils to create magnetic fields with complex 3D shapes, while the idea behind the *tokamak* is to superimpose a weaker poloidal magnetic field—induced by a strong toroidal plasma current—with a strong toroidal magnetic field. Additional field coils are used in a tokamak to shape and control the plasma.

The word *tokamak* is an acronym for the Russian phrase 'toroidal chamber with magnetic coils', and the merit of the device was first proven in the late 1960's by Soviet scientists at the Kurchatov Institute in Moscow. Reaching higher temperatures and confining the plasma for longer periods of time [13], they demonstrated that the tokamak design was superior to previous and contemporary machines. Researchers across the world put their efforts into building and advancing such machines; other concepts were put to the side. Today, over 50 years after the Soviets first demonstrated the virtues of the tokamak, it remains the most well researched concept for magnetic confinement fusion. A schematic drawing of a tokamak plasma is shown in Fig. 1.2, where the coordinates typically used to parametrize the machine are also shown: ϕ is the toroidal angle, R the major radius (measured from the axis of symmetry), Z the elevation, r the minor radius (measured from the magnetic axis at $R = R_m$) and θ is the poloidal angle. In Fig. 1.2, the flux surfaces—the surfaces on which the magnetic field is constant—are indicated as contours on the poloidal cross sections of the plasma; in a tokamak, the flux surfaces are arranged as nested tori.

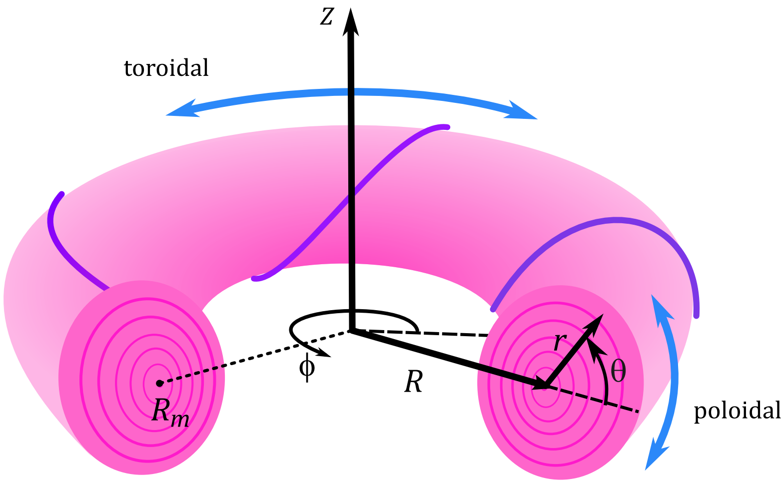

Figure 1.2: A toroidal plasma. The blue arrows show the toroidal and poloidal directions respectively, while the directions of the coordinates R, Z, r, ϕ and θ are shown as black arrows. A magnetic field line is also shown: note that the poloidal twist is exaggerated. The magnetic axis is located at $R = R_m$, where $r = 0$.

For fusion to become a viable means of energy production, the fusion plasma must yield more power than is needed to sustain it. The ratio of net fusion power to input power is referred to as *Q-factor*; it is not until $Q > 1$ that we actually gain energy from fusing nuclei together in a machine. So far, no tokamak (past or present) has reached $Q \geq 1$. At high enough Q—well above the so-called *scientific breakeven* at $Q = 1$, where the output power equals the input power—it is expected that a fusion plasma would reach so-called *ignition*. Once this has been achieved, the need for auxiliary heating vanishes: the plasma is able to sustain itself through the excess energy produced in the fusion reactions, much like firewood burning continuously once it is warm enough and while there is fuel available.

Today, there are a number of tokamaks in operation around the globe. The Joint European Torus (JET), located in the United Kingdom, is currently the largest tokamak in the world with its major radius of 2.96 m [14]. Finished during the late 1970's, JET is a collaboration between a number of European nations and holds the world record for most fusion energy produced. This record was set in 1997, when researchers managed to produce enough output power to reach $Q = 0.67$ by fusing deuterium and tritium together. JET has been in operation since the early 1980's, but the record breaking tokamak is nearing the end of its lifetime. At the time of writing, JET is scheduled to shut down operations during the mid 2020s.

As for future experiments, the most notable are perhaps ITER and SPARC. ITER is a collaboration between China, the European Union, India, Japan, Korea, Russia and the United States, and will with its major radius of 6.2 m [15] replace JET as the largest tokamak in the world. ITER is currently under construction in France, with first plasma scheduled for December 2025 [16]. It is designed to be able to produce an output power of 500 MW from 50 MW of input power [16] (i.e. $Q = 10$, well above scientific breakeven), thus demonstrating the viability of tokamaks as power production plants.

SPARC is a strong magnetic field machine designed by Commonwealth Fusion Systems (CFS), a US company sprung out of research performed at the Massachusetts Institute of Technology (MIT) Plasma Science and Fusion Center (PSFC). Its construction is planned to begin in 2021 [17]. SPARC aims to reach $Q > 2$ [18] by scaling up the magnetic field rather than the linear size of the machine. By constructing the magnetic field coils out of novel high-temperature superconducting materials, the aim is to produce fields as strong as 12.2 T [18] on the magnetic axis. This is significantly higher than both ITER (predicted 5.3 T on magnetic axis) and JET (3.45 T on magnetic axis [14]). Since the fusion power scales as the magnetic field strength to the fourth power, the strong magnetic fields of SPARC present a promising means of reaching $Q > 1$ and well above.

2
Theory

Due to its constituents being charged particles, the dynamics of a plasma is governed both by collective electromagnetic interactions as well as by collisions between particles. A fluid model—where volume elements in the plasma rather than particle dynamics are considered—is often sufficient to describe much of the plasma's behavior, despite its coarser resolution of reality. However, if we want more detailed information about the momentum dynamics of the particles in the plasma, a kinetic theory—which accounts for the flow of particles in six-dimensional position and momentum space—is required. After a brief introduction to relevant plasma theory and concepts, this chapter dives into the world of tokamak disruptions, runaway electrons and kinetic theory.

2.1 Plasma—the fourth state of matter

A plasma is a gas in which the atoms have been ionized. In fusion plasmas, the high temperatures give bound electrons sufficient energy to break free from the nuclei; their departure turns the previously neutral atoms into charged ions. Since a plasma is nothing but previously neutral atoms 'decomposed' into negatively and positively charged components, the net charge of the plasma is zero on large length scales. This is referred to as *quasi-neutrality*—the number of negative and positive charges cancel each other on the macroscopic scale.

If a point-like test charge was introduced in a plasma, the constituent particles would either be attracted to or repulsed by it. Eventually, enough particles with charges opposite to the test charge would congregate around it to effectively shield it from the rest of the plasma. This effect is called *Debye shielding*, and the distance at which the Coulomb force from the test charge is shielded out is called the *Debye length*. The Debye length λ_D is calculated as [19]

$$\lambda_D = \sqrt{\frac{\varepsilon_0 T_e}{n_e e^2}}, \tag{2.1}$$

where ε_0 is the vacuum permittivity, n_e is the electron particle number density (number of particles per unit volume), e the elementary charge and T_e is the electron temperature. Note that temperatures are typically measured in energy units in plasma physics: to convert between kelvin and energy units, Boltzmann's constant is used.

What is true for the test charge is true for any charged particle in the plasma: it will attract a shield—of thickness λ_D—of particles with charges opposite to its own.

Since the electrons are much lighter and therefore more mobile than the ions, the electrons will typically be the ones forming charge shields around the ions.

For Debye shielding to work, there must be enough particles to form the charge shield. We can statistically assume that this is fulfilled if the number of particles inside a sphere with radius λ_D is large: $4\pi n_e \lambda_D^3/3 \gg 1$. For an ionized gas to be considered a plasma, we require that Debye shielding is indeed in effect, and that the characteristic length scale L of the plasma is such that $L \gg \lambda_D$. In a typical tokamak plasma, these criteria are easily met.

The Debye length is tightly linked with the *Coulomb logarithm* $\ln\Lambda$:

$$\ln\Lambda = \ln\left(\frac{\lambda_D}{b_{\text{min}}}\right) \tag{2.2}$$

where b_{min} the smallest impact parameter, the limit for how close two particles with given velocities in the plasma can get to each other. In a typical tokamak plasma, $\ln\Lambda$ will be of the order of 10 [12], and the majority of the collisions in the plasma will be small-angle, or grazing, collisions. In such collisions, the velocities of the colliding particles are only changed by very little: the Coulomb forces between the particles nudge them slightly away from their original trajectories. The numerous such events can be statistically treated and described as drag and diffusion.

The frictional drag felt by a particle thus depends on the frequency with which the particle collides with the other plasma constituents; for collisions between non-relativistic electrons, the Coulomb collision frequency ν is proportional to the the Chandrasekhar function $G(x)$ [19] depicted in Fig. 2.1, where $x = v/v_{\text{th}}$: v is the velocity of the particle and $v_{\text{th}} = \sqrt{2T_e/m_e}$, where m_e is the electron mass, is the *thermal velocity*, defined so that $3T_e/2$ is the average kinetic energy for electrons at temperature T_e [19]. For collisions between electrons with velocities v such that $v \gg v_{\text{th}}$ the collision frequency is [20]

$$\nu = \frac{e^4 n_e \ln\Lambda}{4\pi\varepsilon_0^2 m_e^2 v^3}. \tag{2.3}$$

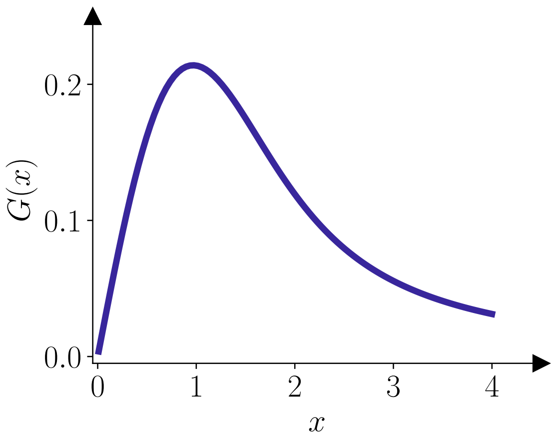

Figure 2.1: The Chandrasekhar function, to which the Coulomb collision frequency for collisions between non-relativistic particles is proportional.

Equation (2.3) tells us that a very fast particle will collide less frequently with the other constituents in a plasma than a slower particle would—the drag from friction decreases with increasing velocity.

In a fully ionized plasma, the number of free electrons N_e^{free} is equal to the total number of electrons N_e^{tot}:

$$N_e^{\text{free}} = N_e^{\text{tot}} = \sum_i Z_i N_i, \tag{2.4}$$

where N_i is the number of ions of species i, and Z_i is the atomic number—the number of protons in the nuclei—of that species. The sum over i accounts for all ion species precent in the plasma.

If the plasma is *not* fully ionized, we must for each species of ion account for the fact that the ions may not have lost all their electrons. Let $Z_i^{(j)}$ be the charge number—denoting which charge the ion has—for an ion of species i occupying the charge state j, and $N_i^{(j)}$ the number of ions of species i which occupy that charge state. The number of free electrons is then

$$N_e^{\text{free}} = \sum_i \sum_j Z_i^{(j)} N_i^{(j)}. \tag{2.5}$$

Above, the sum over i accounts for all different species of ions, while j runs from $j = 0$ for neutral atoms to $j = Z_i$ for fully ionized material (so that $Z_i^{(j)} = j$).

The quantity N_e^{free} is defined as the volume integral over the free electron (number) density n_e^{free} and similarly, the total number of electrons in the plasma is the volume integral of n_e^{tot}:

$$\begin{aligned} N_e^{\text{free}} &= \int n_e^{\text{free}} V' \,\mathrm{d}r\,\mathrm{d}\theta\,\mathrm{d}\phi \\ N_e^{\text{tot}} &= \int n_e^{\text{tot}} V' \,\mathrm{d}r\,\mathrm{d}\theta\,\mathrm{d}\phi \end{aligned} \tag{2.6}$$

where V' is the radial derivative of the plasma volume and r, θ and ϕ are the coordinates shown in Fig. 1.2. The ratio between total and free electron density is important in fusion plasmas since the bound electrons cannot conduct current—they do not contribute to the plasma conductivity σ. The total to free electron ratio is also important for the generation of runaways via so called *avalanche*, a phenomena we will discuss in Section 2.4.1.

A fusion plasma is an excellent conductor. Due to the high temperatures in a plasma, the resistivity $\eta = 1/\sigma$ is small: one estimate of the resistivity is [12]

$$\eta \approx \frac{\pi e^2 \sqrt{m_e}}{(4\pi\varepsilon_0)^2 T_e^{3/2}} \ln\Lambda, \tag{2.7}$$

where we see that η is inversely proportional to $T_e^{3/2}$. This expression is derived from an estimate of the collision frequency between ions and electrons, and the factor $\ln\Lambda$ accounts for the cumulative effect of the numerous small angle collision in the plasma.

2.2 Particle motion in a tokamak

The equations of motion for a particle of species i with charge q and mass m_i in a plasma are given by [19]

$$\boldsymbol{v} = \dot{\boldsymbol{r}} = \frac{\partial \boldsymbol{r}}{\partial t} \quad \text{and} \tag{2.8}$$

$$\boldsymbol{a} = \dot{\boldsymbol{v}} = \frac{q}{m_i}(\boldsymbol{E} + \boldsymbol{v} \times \boldsymbol{B}), \tag{2.9}$$

which tells us that the particles will be accelerated by the Lorentz force, proportional to $\boldsymbol{E}+\boldsymbol{v}\times\boldsymbol{B}$. This will result in helical particle trajectories along the magnetic field lines as is illustrated in Fig. 2.2. The particle velocity vector $\boldsymbol{v}$ can be decomposed into two components: $\boldsymbol{v} = v_{\parallel}\hat{\boldsymbol{b}}_{\parallel} + v_{\perp}\hat{\boldsymbol{b}}_{\perp}$. Here, $\hat{\boldsymbol{b}}_{\parallel}$ is a unit vector in the direction parallel to the magnetic field lines, and $\hat{\boldsymbol{b}}_{\perp}$ is a unit vector perpendicular to the magnetic field lines. The superposition of these two velocity components results in a gyrating motion around the so-called *guiding-center*, and the radius of the circular component of the trajectory is the *Larmor radius* r_{L} [12]

$$r_{\mathrm{L}} \equiv \frac{v_{\perp}}{\omega_c} = \frac{m_i v_{\perp}}{|q|B}, \tag{2.10}$$

where $\omega_c \equiv |q|B/m_i$ is the cyclotron frequency, m_i is the mass of the particle, $|q|$ is the absolute value of the charge of the particle and $B = |\boldsymbol{B}|$ the magnitude of the magnetic field. The relationship between the parallel and perpendicular momentum

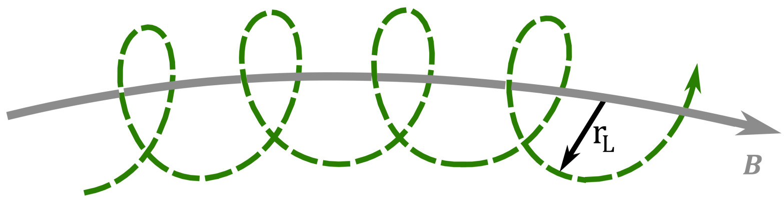

Figure 2.2: A particle gyro-orbit (dashed green) around an magnetic field line (solid grey). The Larmor radius of the orbit is indicated by the black arrow.

is captured in θ_p, the *pitch angle*. This parameter is defined as $\theta_p \equiv \arctan\left(p_{\perp}/p_{\parallel}\right)$. Using the pitch angle, the perpendicular and parallel components of the momentum can be expressed via the particle *pitch* $\xi \equiv \cos\theta_p$: $p_{\perp} = p\sqrt{1-\xi^2}$ and $p_{\parallel} = p\xi$, where $p = |\boldsymbol{p}|$.

2.3 Disruptions in tokamaks

A disruption in a tokamak is an off-normal, unwanted event where the energy confinement of the plasma is lost on a short time scale. One cause of disruptions is the introduction of some foreign material into the plasma. In some instances, these materials are impurities originating from the machine wall. Other times, they have been deliberately injected into the plasma as part of an experiment. Either way, the foreign particles can trigger the chain reaction of events leading to a disruption.

The first stage of a disruption is the *thermal quench*: due to a variety of energy loss mechanisms (such as ionization losses and heat and particle transport due to broken up magnetic field lines), the plasma temperature decays. This phase is characterized by the *thermal quench time* t_{TQ}: the time it takes for the temperature to decay to its post-disruption value. For JET, t_{TQ} is typically on the order of a few milliseconds, and the post-disruption temperature a few eV [21]. Since the plasma resistivity η is proportional to $T_e^{-3/2}$, the decrease in temperature results in an increased resistivity and thus initiates a decay of the plasma current—the so-called *current quench*. As the resistivity increases and the plasma current decays, Ohm's law tells us what must happen: the electric field must grow for the current to be maintained, and as a result, the light electrons in the plasma will be accelerated. Some electrons might reach relativistic energies and become *runaway electrons* (or just runaways). This means that the total plasma current I_p is then a sum of two current components: the ohmic component I_Ω carried by the thermal bulk electrons, and the runaway component I_{RE} carried by the runaway electrons in the plasma. The generation of runaways might thus ensure that the total plasma current does not decay all the way to zero: the runaway component will halt the current decay at some platform value. This platform is the so-called *runaway plateau*, where the ohmic component of the current is negligible compared to the current carried by the runaway electrons. The time it takes for the plasma current to decay to its post-disruption value—which will in this thesis be the runaway plateau—is referred to as the *current quench time* t_{CQ}. A current quench in JET typically lasts for a few milliseconds [21].

In order to study runaways in tokamaks, disruptions are intentionally triggered so that runaway beams may form. Massive gas injections (MGI) can be used to this end; cold gas of a relatively high-Z material (e.g. argon with $Z_{\mathrm{Ar}} = 18$) is injected into the thermal plasma, where the onslaught of increased losses and instabilities it causes results in a disruption. If a large portion of the electrons in the plasma are converted into runaways during a disruption, and control of said electrons is lost on a short timescale, significant damage could be inflicted on the machine by the energetic particles.

2.4 Runaway electrons

Since electrons are so light, they are excellent targets for the growing electric field induced during the current quench in a tokamak disruption. We noted in Section 2.1 that the friction force acting on particles traversing through a plasma depends on their collision frequency ν, and in Eq. (2.3), we saw that for particles with $v \gg v_{\mathrm{th}}$, ν is inversely proportional to v^3. Due to the velocity dependence of ν, particles travelling at high speeds experience very little drag from friction; once a runaway is created, it can be quite difficult to slow it back down to a thermal electron.

Since the deceleration force decreases with increasing particle momentum, there is a threshold at which any additional acceleration, e.g. from an external electric field induced during a disruption, is enough to overcome the friction forces acting on a particle and cause it to run away. This threshold for the momentum is called the *critical momentum*.

2.4.1 Runaway generation in tokamaks

All runaway electrons travel at relativistic speeds, but not all runaways are created in the same way; there are a number of ways thermal electrons can be converted into runaways in tokamaks.

Dreicer generation is the process where thermal electrons are accelerated to relativistic momenta by the growing electric field induced by the current quench in a disruption. Typically, not all bulk electrons are energetic enough to be converted into runaways by the electric field—the acceleration is balanced by the friction forces felt by the particles—but for the faster thermal electrons, with $p \geq p_c$ where p_c is the critical momentum, even a small electric field can be enough to overcome the drag from friction. The electric field strength required to overcome the friction forces acting on the bulk electrons in a plasma scales with the so-called *Dreicer field* E_D [19]

$$E_D = \frac{n_e e^3 \ln \Lambda}{4\pi\varepsilon_0^2 T_e} = \frac{n_e e^3 \ln \Lambda}{2\pi\varepsilon_0^2 v_{\mathrm{th}}^2 m_e}. \tag{2.11}$$

If $E > 0.21 E_D$ [22], every free electron in the plasma would be converted into a runaway.

Accounting for the fact that the drag on the particles does not go all the way to zero as $v \to c$ (where c is the speed of light) gives another threshold for the electric field required to create runaways—the *critical electric field* E_c given by [20]

$$E_c = \frac{n_e e^3 \ln \Lambda}{4\pi\varepsilon_0^2 m_e c^2} = E_D \frac{v_{\mathrm{th}}^2}{2c^2}. \tag{2.12}$$

The condition that $E > E_c$ also gives us an estimation of the critical momentum p_c—at which a thermal electron is susceptible to being converted into a runaway—as $p_c/(m_e c) \sim 1/\sqrt{E/E_c - 1}$; at $p \geq p_c$, the drag from the collisions on the electron in is not enough to balance out the acceleration from an external electric field. For large electric fields we can estimate the critical momentum to $p_c/(m_e c) \sim \sqrt{E_c/E}$. Once an electron has been accelerated to relativistic energies, collisions will ensure that the 'gap' in momentum space left behind by the newly created runaway electron is filled by another electron. But this means that the electron which collisions have forced to fill the gap now has $p \sim p_c$ and is susceptible to acceleration by the electric field. In plasmas where $E_c < E \ll E_D$ this continuous gap-filling process will lead to a diffusive leak of particles from the thermal population into the runaway region of momentum space.

Avalanche generation (or avalanche multiplication) is the mechanism where already existing runaways help create new runaways via large-angle Coulomb collisions [23]. When a relativistic electron collides with a thermal electron, it will transfer some of its momentum to the slower particle. The energy gained by the non-relativistic electron is on its own typically not enough to convert it into a runaway. However, the impact might impart the thermal particle with enough momentum for it to reach the critical momentum, making it susceptible to being converted into a runaway electron. A small seed population of runaways can thus trigger an avalanche of runaway generation. The number of electrons created via avalanche generation is exponentially sensitive to the plasma current: it scales as $\exp(\Gamma_{\mathrm{ava}} t)$, where an estimate of $\Gamma_{\mathrm{ava}} t$ is given by [9]

$$\Gamma_{\mathrm{ava}} t \approx \frac{eEt}{m_e c \ln \Lambda} \approx \frac{I_p e}{m_e c^3 \ln \Lambda}. \tag{2.13}$$

Above, I_p is the toroidal plasma current required to twist the magnetic field in a tokamak. In machines such as ITER, where plasma currents will be as high as 15 MA [24], this would yield $\Gamma_{\mathrm{ava}} t \sim 50$ while in JET, where $I_p \sim 1$ MA, we instead obtain $\Gamma_{\mathrm{ava}} t \sim 2$ [9].

Hot-tail generation takes place during a fast (enough) thermal quench. In such a scenario, the temperature drops too quickly for the more energetic of the bulk electrons to have time to thermalize to the new temperature [25]. Instead, these electrons will be accelerated to relativistic energies when the electric field rises. In Ref. [25], the hot-tail mechanism was found to dominate over Dreicer generation for thermal quench times $t_{\mathrm{TQ}} \lesssim 0.3\,\mathrm{ms}$ in simulations of JET disruptions. Hot-tail generation only occurs during the thermal quench, while Dreicer generation and avalanche multiplication can happen at any time during the disruption, as long as the electric field is sufficiently strong.

2.4.2 Synchrotron radiation from runaway electrons

Due to their trajectories, the charged particles in a tokamak plasma will emit cyclotron radiation: the acceleration of the particles will cause them to radiate electromagnetic energy. The cyclotron radiation emitted by relativistic particles, such as runaway electrons, is referred to as *synchrotron radiation* [26].

Synchrotron radiation from runaway electrons is emitted in a broad spectrum of frequencies (ranging from IR to UV light), and mainly in the forward direction of the particles [26]. These two traits ensure that the presence of runaways can be detected with cameras in tokamaks: synchrotron spots—bright blobs of light—will appear on one side of the center column of the tokamak but not on the other, and these synchrotron spots can be observed with detectors registering light in the visual or IR spectral range. The electric field of the synchrotron radiation emitted by the runaways can be written as [26]

$$\tilde{\boldsymbol{E}} = \hat{\boldsymbol{e}}_\perp \tilde{E}_\perp + i\hat{\boldsymbol{e}}_\parallel \tilde{E}_\parallel, \tag{2.14}$$

where $\hat{\boldsymbol{e}}_\perp$ and $\hat{\boldsymbol{e}}_\parallel$ are unit vectors. Above, $\hat{\boldsymbol{e}}_\parallel$ is parallel to the direction of the acceleration—for runaways with velocity $\boldsymbol{v}$ in the presence of an electric field $\boldsymbol{E}$ and a magnetic field $\boldsymbol{B}$, this acceleration is caused by the Lorentz force: $\hat{\boldsymbol{e}}_\parallel \propto (\boldsymbol{E}+\boldsymbol{v}\times\boldsymbol{B}) \approx \boldsymbol{v}\times\boldsymbol{B}$, since the electric field term is negligible for runaway electrons in tokamaks. The second unit vector, $\hat{\boldsymbol{e}}_\perp$, will then be orthogonal to the plane spanned by $\hat{\boldsymbol{e}}_\parallel$ and a unit vector $\hat{\boldsymbol{n}}$ which points from the electron emitting the radiation to an observer: $\hat{\boldsymbol{e}}_\perp \propto \hat{\boldsymbol{n}} \times \hat{\boldsymbol{e}}_\parallel$. For the relativistic runaways the parallel component is much larger than the perpendicular component, $\tilde{E}_\parallel \gg \tilde{E}_\perp$, and the result is that the synchrotron radiation is almost completely linearly polarized in the direction of $\hat{\boldsymbol{e}}_\parallel$ [27]. Furthermore, it can be shown that the circularly polarized synchrotron radiation emitted by the runaway electrons vanishes [28]—the synchrotron radiation is either unpolarized or linearly polarized.

Another diagnostic which can be used to register synchrotron light from runaways is the Motional Stark Effect (MSE) detector. Registering radiation from runaway electrons is however not the primary purpose of this diagnostic. In tokamaks, an MSE detector typically registers the polarized line radiation from the excitation of deuterium atoms—in JET, the most prominent such transition gives off radiation with wavelength $\lambda = 656.3\,\mathrm{nm}$ [29] and corresponds to a $3 \to 2$ transition. In the presence of a magnetic field, the Stark effect will cause the spectral lines to split. Using measurements from the MSE diagnostic in JET, the q-profile—the ratio between the poloidal and toroidal twist in the magnetic field lines—can be calculated during normal operation [29]. In Ref. [30], the MSE diagnostic in Alcator C-Mod was used to measure the polarized synchrotron radiation from runaways; both the fraction of linearly polarized light and the polarization angle of the synchrotron light can be measured using this diagnostic.

2.4.3 Runaway electron mitigation

Runaway electrons are bound to pose an even bigger threat as tokamak sizes increase; the energy content of the plasma is greater in larger machines, implying that more energy will be available to be converted into runaway electron energy. More importantly, as is evident from Eq. (2.13) the stronger plasma currents in such machines will lead to exponentially higher runaway multiplication rates. For a tokamak like ITER, where plasma currents will be as strong as 15 MA, there must be mechanisms in place to safely deal with any runaway electrons that might be generated during its operation; the runaway beams must be dispersed in a manner that does not cause damage to the tokamak. One method considered for runaway mitigation in ITER is *shattered pellet injection* (SPI) [31], where frozen pellets of some material (e.g. deuterium or neon) are shattered into small pieces prior to or while they are being injected into the plasma. Firing an SPI into the plasma could disperse the runaway energy via a multitude of mechanisms: energy will be radiated away as the injected neutral atoms are ionized, and the resulting increase in electron density results in more collisions taking place. The presence of high-Z material also leads to *pitch angle scattering*: collisions with other plasma constituents result in increased perpendicular momentum $p_\perp$ for the runaway electrons, so that their pitch angle θ_p grows. Increased pitch angles lead to more energy lost via synchrotron emission: the emitted synchrotron power scales as $\sin^2\theta_p$ [11]. However, recent results indicate that the SPI approach might not solve the runaway issue all the way: if the plasma is cooled enough by the injected material for the ions to begin to recombine, the number of target electrons for avalanche multiplication increases—something that might balance out and even overshadow the slowing-down effect the increased collisionality and pitch angle scattering has on the particles [32, 33].

2.5 Kinetic theory

When treating the plasma as a fluid, the governing equations are dealt with in three-dimensional position space $\boldsymbol{r}$. The kinetic approach allows us to take the particles' momenta into consideration: we do not only consider plasma quantities in three-dimensional space, but in the three-dimensional velocity (or momentum) space as well. In kinetic theory, particles of species i are typically represented by their *distribution function*, a six-dimensional function describing how the particles are distributed in space and velocity space. A central part of kinetic runaway theory is the *kinetic equation* for the electrons, which describes the evolution of the particle distribution function in time. It accounts for the influence of external electromagnetic fields as well as the effects of collisions, and includes source terms for adding new particles when applicable. We will familiarize ourselves further with the kinetic equation for electrons in Section 2.5.2, but before that, we will introduce the distribution function.

2.5.1 The distribution function

Each particle in the plasma has, at a given time, a certain position and travels at a certain velocity; at time t, the particles of species i are distributed in position and velocity space according to a six-dimensional *distribution function* $f_i(t, \boldsymbol{r}, \boldsymbol{v})$. Here, $\boldsymbol{r}$ is the three dimensional position vector and $\boldsymbol{v}$ the three dimensional velocity vector; the six-dimensional space consists of possible positions $\boldsymbol{r}$ and velocities $\boldsymbol{v}$ and is referred to as *phase space* (note that considering $\boldsymbol{p}$ rather than $\boldsymbol{v}$ yields an equivalent representation of the distribution function). The number of particles at position $\boldsymbol{r}$ with velocities such that $\boldsymbol{v} \in [\boldsymbol{v}, \boldsymbol{v} + \mathrm{d}\boldsymbol{v}]$ is then $f_i(t, \boldsymbol{r}, \boldsymbol{v})\mathrm{d}\boldsymbol{v}$, and the total (number) density of particles at $(t, \boldsymbol{r})$ is

$$n_i(t, \boldsymbol{r}) = \int f_i(t, \boldsymbol{r}, \boldsymbol{v})\, \mathrm{d}\boldsymbol{v}. \tag{2.15}$$

In a plasma, collisions drive the velocity distribution functions of the constituent particles toward a Maxwellian shape (so that the particles are isotropic in velocity space) [19]. A purely Maxwellian velocity distribution function for the particle species i can be uniquely specified by the population's temperature T_i and density n_i [12]:

$$f_i = n_i(t, \boldsymbol{r}) \left(\frac{m_i}{2\pi T_i} \right)^{3/2} \exp\left[-\left(\frac{v - v_{\text{flow}}}{v_{th}} \right)^2 \right], \tag{2.16}$$

where v_{flow} is a flow velocity which shifts the maximum of the Maxwellian away from $v = 0$, and $v^2 \equiv (v_x^2 + v_y^2 + v_z^2)$.

In a tokamak plasma where runaway electrons are present, the distribution function of the electron population deviates from the purely Maxwellian shape. Although the bulk of the electrons are still Maxwellian, the relativistic particles reside in the 'tail' of the distribution function: it is not enough to know the bulk electron temperature T_e and density n_e to characterize the runaway electrons.

A number of quantities can be obtained by taking different moments of $f_i(t, \boldsymbol{r}, \boldsymbol{v})$; we already saw an example of this in Eq. (2.15), where the lowest moment of the distribution function gave us the density of particles. Generally, for a quantity A we have [19]

$$\langle A \rangle_f \equiv \frac{1}{n_i(t, \boldsymbol{r})} \int A f_i(t, \boldsymbol{r}, \boldsymbol{v}) \mathrm{d}\boldsymbol{v}, \tag{2.17}$$

where $\langle A \rangle_f$ is the quantity A integrated over velocity space and weighted with the distribution function for species i.

2.5.2 The kinetic equation

The electron distribution function $f_e(t, \boldsymbol{r}, \boldsymbol{v})$—which will be denoted f_e for brevity—evolves in time according to an equation which will in this thesis be referred to as the *kinetic equation*. This equation is essentially a conservation equation for the number of electrons in phase space. Letting $\boldsymbol{z} \equiv (\boldsymbol{r}, \boldsymbol{v})$, we can write the velocity with which the particles flow in phase space as $\dot{\boldsymbol{z}} = (\dot{\boldsymbol{r}}, \dot{\boldsymbol{v}})$. The conservation equation for the number of electrons is then [19]

$$\frac{\partial f_e}{\partial t} + \frac{\partial}{\partial \boldsymbol{z}} \cdot (\dot{\boldsymbol{z}} f_e) = 0, \tag{2.18}$$

where the second term on the left hand side describes the six-dimensional particle flux divergence. Using the definition of $\dot{\boldsymbol{r}}$ and $\dot{\boldsymbol{v}}$ from Eq. (2.8) and Eq. (2.9), the fact that $\nabla \cdot \boldsymbol{v} = 0$ (since $\boldsymbol{r}$ and $\boldsymbol{v}$ are independent variables), and that $(\partial/\partial \boldsymbol{v}) \cdot \dot{\boldsymbol{v}} = 0$ [19] (since $\boldsymbol{v} \times \boldsymbol{B}$ is perpendicular to $\boldsymbol{v}$, and $\boldsymbol{E}$ is independent of $\boldsymbol{v}$), the particle flux divergence term can be written as

$$\frac{\partial}{\partial \boldsymbol{z}} \cdot (\dot{\boldsymbol{z}} f_e) = \boldsymbol{v} \cdot (\nabla f_e) + \frac{e}{m_e}(\boldsymbol{E} + \boldsymbol{v} \times \boldsymbol{B}) \cdot \frac{\partial f_e}{\partial \boldsymbol{v}} \tag{2.19}$$

On a macroscopic scale, we can regard $\boldsymbol{E}$ and $\boldsymbol{B}$ as slowly fluctuating, but on length scales comparable to λ_D these fields fluctuate wildly; on small length scales we have to account for electromagnetic fields from individual charged particles. For this reason, the term in Eq. (2.19) containing $\boldsymbol{E}$ and $\boldsymbol{B}$ is split into two: one term which looks identical to the original term with $\boldsymbol{E}$ and $\boldsymbol{B}$, but where these fields are now the large-scale fields (averaged over many Debye lengths), and the so called *collision operator* $C\{f_e\}$ [19]. The collision operator is typically relocated to the right-hand side of Eq. (2.18), and accounts for the interactions between particles due to the short-range fluctuations of the electromagnetic fields—the collisions between particles—so that

$$C\{f_e\} = \left.\frac{\partial f_e}{\partial t}\right|_{\text{collisions}}. \tag{2.20}$$

Allowing for a source term S describing how electrons are added or disappear (for example due to ionization or recombination of ions respectively), and using what we found about the particle flux divergence term gives the kinetic equation for electrons as [19]

$$\frac{\partial f_e}{\partial t} + \boldsymbol{v} \cdot (\nabla f_e) + \frac{e}{m_e}(\boldsymbol{E} + \boldsymbol{v} \times \boldsymbol{B}) \cdot \frac{\partial f_e}{\partial \boldsymbol{v}} = C\{f_e\} + S. \tag{2.21}$$

This equation describes the evolution of the electron distribution function in time, and it is one of the equations solved in DREAM.

3
Numerical tools

Since present day tokamaks only have access to a small region of the parameter space which will be available to future machines, numerical modeling is an important tool to make predictions for runaway generation in the next generation of tokamaks. Over the years, a number of codes for numerical modeling of tokamak plasmas and runaway electron dynamics in disruptions have been developed. Examples of such codes are Go [34, 35], which models the plasma as a fluid, and Code [36, 37], capable of kinetic modeling of the electron distribution function. To self-consistently model both the plasma dynamics and the momentum dynamics of the runaway electrons, kinetic codes must be coupled to numerical tools capable of self-consistent modeling of the plasma during a tokamak disruption. Such coupled simulations are however computationally expensive. A new addition to the family of disruption modeling software is the numerical solver Dream, which can self-consistently model both the plasma and the runaway electrons during a tokamak disruption.

Dream (Disruption Runaway Electron Analysis Model) [10] is capable of solving a set of coupled equations describing a fusion plasma during a tokamak disruption. It is specialized in modeling runaway electrons during such scenarios and is one-dimensional in the spatial direction, meaning that it resolves the variation of plasma parameters across the magnetic flux surfaces parametrized by the minor radius coordinate r, and two-dimensional in momentum space: $\boldsymbol{p} = (p, \xi)$. Fluid models are used to evolve background plasma parameters, such as ion and electron temperatures, toroidal electric field and the densities of various ion charge states, while the electrons can be modeled kinetically via their distribution function. Dream thus outputs two different kinds of quantities: *fluid* quantities which depend on (t, r), and *kinetic* quantities depending on (t, r, p, ξ).

Apart from fully kinetic modeling of the electrons, several approximate electron models are also available. The latter allow for more efficient modeling than with the fully kinetic approach, often without significant loss of accuracy. Dream supports arbitrary axisymmetric toroidal geometry; simulations in this thesis were performed in a cylindrical geometry, thus ignoring effects from toroidicity. This is a reasonable approximation for $\epsilon \ll 1$, where ϵ is the inverse aspect ratio: $\epsilon \equiv r/R_0$ where r is the (minor) radial coordinate of the plasma and R_0 the major radius of the torus.

The electron distribution functions obtained from Dream simulations can be given as input to the synthetic synchrotron diagnostic tool Soft (Synchrotron-detecting Orbit Following Toolkit) [11]. By using such distribution functions, Soft is capable of generating synthetic synchrotron diagnostic signals, such as camera images and signals from an MSE detector, from events modeled in Dream. By coupling results from Dream to Soft, we get a novel way of validating the physics models used in DREAM: the synthetic synchrotron data from SOFT gives us an additional synthetic diagnostic signal to compare against experimental data. Since the synchrotron radiation is sensitive to the details of the distribution function [38] (where signals such as the plasma current is less so), the synchrotron data can reveal more about the runaways than the amount of current they are carrying. If DREAM can be successfully validated against current experimental data, it can be used to reliably model disruption scenarios in future machines such as ITER to predict how runaways might form, behave and be mitigated [33].

3.1 DREAM

As established above, DREAM uses the (minor) radial coordinate r, denoting the radial location in the cylindrical plasma (measured from the magnetic axis R_m). We also saw that instead of representing the momentum $\boldsymbol{p}$ by its three components in the (x, y, z)-directions, DREAM uses the two phase space coordinates $p = \sqrt{p_x^2 + p_y^2 + p_z^2}$ and $\xi = \boldsymbol{B} \cdot \boldsymbol{p}/Bp = \cos\theta_p$. This a representation of the momentum in spherical coordinates, under the assumption that the modeled dynamics are independent of the azimuthal angle φ, also referred to as the gyro angle. In DREAM, the coordinates (r, p, ξ) are constants of motion.

Stated in its most general form, DREAM solves an advection-diffusion equation for various quantities; for the purposes of this thesis, one such central quantity will be the electron distribution function $f_e \equiv f_e(r, p, \xi, t)$. This means that DREAM solves the advection-diffusion equation [10]

$$\frac{\partial f_e}{\partial t} = \frac{1}{\mathcal{V}'}\frac{\partial}{\partial z^m}\left[\mathcal{V}'\left(- A^m f_e + D^{mn}\frac{\partial f_e}{\partial z^n}\right)\right] + S. \tag{3.1}$$

Above, repeated indices are summed over, and z^i is a vector of phase-space coordinates: in our case $\boldsymbol{z} = (r, p, \xi)$. S is a source term. We also have $A^m = (\partial z^m/\partial \boldsymbol{z}) \cdot \boldsymbol{A}$ and $D^{mn} = (\partial z^m/\partial \boldsymbol{z})(\partial z^n/\partial \boldsymbol{z}) : \mathtt{D}$ (in dyadic notation). In Eq. (3.1), the term containing $\boldsymbol{A}$ is an advection term and contains contributions from electric field acceleration, collisional friction and the synchrotron radiation reaction force. $\mathtt{D}$ is the diffusion tensor accounting for diffusion in momentum space stemming from collisions. The phase space Jacobian is given by

$$\mathcal{V}' = V'p^2, \tag{3.2}$$

$$V' = 4\pi^2 R_m r, \tag{3.3}$$

where R_m is the magnetic axis (a constant) and r the minor radial coordinate. DREAM solves Eq. (3.1) in a static axisymmetric magnetic geometry: in the cylindrical geometry of DREAM, the magnetic field is constant and perpendicular to the plane spanned by r and θ.

3.1.1 Momentum regions and the electron grids

When DREAM is run in the fully kinetic mode, all of phase space is resolved kinetically. Even though this approach is often the most accurate, it might not be necessary: similar results can be achieved with approximate electron models that allow for much more efficient modeling. To support such approximate electron models, DREAM divides momentum space into three separate regions. In the first region, thermal electrons with momentum $p \sim p_{\mathrm{th}} \sim 0.01 m_e c$ reside: these electrons belong to the *cold* electron population. The second region contains the *hot* electron population, where particles have momentum $p_{\mathrm{hot}} \leq p < p_{\mathrm{RE}}$. The lower bound p_{hot} is $p_{\mathrm{hot}} \sim p_c \sim 0.1 m_e c$, i.e. the momentum at which the electrons are susceptible to be accelerated by an external electric field and become runaways. Finally, the *runaway* population lives in the third region, where $p_{\mathrm{RE}} \leq p \leq p_{\mathrm{max}}$ where p_{max} defines the upper limit for the momentum grid in DREAM. Since the electron dynamics will typically differ between the three regions, dividing the electrons into three separate populations ensures each population can be given specialized treatment in DREAM.

When the fully kinetic model is used, DREAM resolves the electron population on two different momentum grids: the *hot* grid and the *runaway* grid. The cold and hot electron population, i.e. electrons with $0 \leq p < p_{\mathrm{RE}}$, are modelled on the hot grid. These electrons are represented by their common distribution function f_{hot}. Electrons with $p \geq p_{\mathrm{RE}}$ are instead modelled on the runaway grid, and are described by their own distribution function f_{RE}.

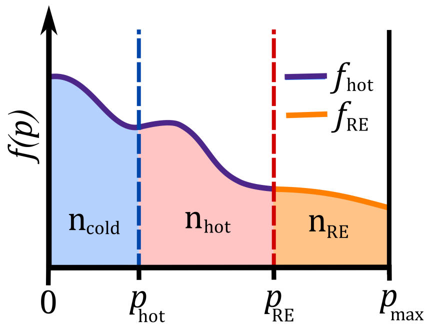

Figure 3.1: The three momentum regions used in the fully kinetic mode in DREAM.

The densities associated with each of the electron populations are such that $n_{\mathrm{free}} = n_{\mathrm{cold}} + n_{\mathrm{hot}} + n_{\mathrm{RE}}$, where the hot and runaway densities are defined as

$$n_{\mathrm{hot}} = 2\pi \int_{p_{\mathrm{hot}}}^{p_{\mathrm{RE}}} \int_{-1}^{1} f_{\mathrm{hot}} p^2 \,\mathrm{d}\xi\,\mathrm{d}p, \qquad \text{hot electron density} \tag{3.4}$$

$$n_{\mathrm{RE}} = 2\pi \int_{p_{\mathrm{RE}}}^{p_{\mathrm{max}}} \int_{-1}^{1} f_{\mathrm{RE}} p^2 \,\mathrm{d}\xi\,\mathrm{d}p, \qquad \text{runaway electron density.} \tag{3.5}$$

Above, the factor p^2 in the integrals is the Jacobian determinant for the momentum space and the factor 2π comes from the integration over the gyro angle φ of the particles. The cold electrons are defined by the following fluid quantities:

$$n_{\mathrm{cold}} = n_{\mathrm{free}} - n_{\mathrm{hot}} - n_{\mathrm{RE}}, \qquad \text{cold electron density} \tag{3.6}$$

$$T_{\mathrm{cold}} = \frac{2}{3}\frac{W_{\mathrm{cold}}}{n_{\mathrm{cold}}}, \qquad \text{temperature} \tag{3.7}$$

$$j_\Omega = \sigma E_\parallel, \qquad \text{parallel ohmic current density} \tag{3.8}$$

where W_{cold} in Eq. (3.7) is the heat content of the electrons. Note that the definition of n_{cold} in Eq. (3.6) is only used when the cold electrons are not modeled kinetically; when the cold population is modeled via f_{hot}, n_{cold} is defined similar to n_{hot} (i.e. via the integral of f_{hot} over gyro angle and phase space, but for momenta $0 \leq p \leq p_{\mathrm{hot}}$). In Eq. (3.8), $E_\parallel$ is the component of the toroidal electric field which is parallel to the magnetic field: $\boldsymbol{E} = E_\perp \hat{\boldsymbol{b}}_\perp + E_\parallel \hat{\boldsymbol{b}}_\parallel$ where $\hat{\boldsymbol{b}}_\perp$ and $\hat{\boldsymbol{b}}_\parallel$ are the unit vectors in the directions perpendicular and parallel to the magnetic field respectively. The conductivity σ is the Braams-Karney conductivity [39], and it is a function of the density, temperature and impurity content of the plasma.

The parallel current densities for the hot and runaway populations are defined as

$$j_{\mathrm{hot}}(r) = -2\pi e \int_{p_{\mathrm{hot}}}^{p_{\mathrm{RE}}} \int_{-1}^{1} v\xi f_{\mathrm{hot}} p^2 \,\mathrm{d}\xi \,\mathrm{d}p, \tag{3.9}$$

$$j_{\mathrm{RE}}(r) = -2\pi e \int_{p_{\mathrm{RE}}}^{p_{\mathrm{max}}} \int_{-1}^{1} v\xi f_{\mathrm{RE}} p^2 \,\mathrm{d}\xi \,\mathrm{d}p, \tag{3.10}$$

where again the factor 2π stems from integrating over the gyro angle, and p^2 is the momentum space Jacobian.

3.1.2 Electron models

As previously established, DREAM not only allows for kinetic modeling—it also supports a number of approximate electron models. Two such models are relevant for this thesis:

1. *Fluid electrons*: the kinetic grids are *not* used, and all electrons are modeled as fluid quantities via the two electron densities n_{cold} and n_{RE}. Electrons with $p \geq p_{\mathrm{RE}}$ belong to the runaway electron population, while all other electrons belong to n_{cold}.
2. *Kinetic runaway, fluid generation*: the kinetic runaway grid is used, meaning that electrons with $p \geq p_{\mathrm{RE}}$ are modeled kinetically via f_{RE}. Electrons with $p < p_{\mathrm{RE}}$ are belong to n_{cold}, which is modeled as a fluid quantity. Fluid growth rates are used for the runaway generation at the boundary p_{RE}.

Most simulations in this thesis were performed using the second approximate electron model describe above. This model yields a distribution function for the runaway electrons while dealing with the bulk electrons in the fluid mode, which is less computationally expensive than the fully kinetic approach. When fitting parameters, the fluid electron model was used—simulations using the fluid model were much faster than simulations including the runaway grid, why they were better suited for parameters scans.

Runaway generation processes are accounted for differently in DREAM depending on which electron model is used. In the fully kinetic mode—when all three electron populations are modeled kinetically—Dreicer and hot-tail runaway generation is included automatically since DREAM then solves the full kinetic equation. A Rosenbluth-Putvinski avalanche source term [9] can be included in the kinetic equation for f_{RE} to account for runaways created via avalanche multiplication. If the electrons are instead modeled with the approximate electron models described above, we must explicitly tell DREAM which kinds of runaway generation we want to include in the simulations. In the fluid model, runaway generation rates for Dreicer and avalanche generation are available—hot-tail generation can be accounted for via an additional source term.

3.1.3 Ions

In DREAM, the user can choose to either prescribe the ions to be (and remain) in some arbitrary charge state j or completely neutral (i.e. $j = 0$), or model them dynamically. The latter case means that the ion population is modeled self-consistently; to achieve this, we must know which charge states the ions occupy.

DREAM evolves each charge state j of an ion species i via its density $n_i^{(j)}$. The rate of change of the charge state density $n_i^{(j)}$ is

$$\frac{\partial n_i^{(j)}}{\partial t} = \Big[I_i^{(j-1)} n_i^{(j-1)} - \Big(I_i^{(j)} + R_i^{(j)}\Big) n_i^{(j)} + R_i^{(j+1)} n_i^{(j+1)}\Big] n_{\mathrm{cold}}, \tag{3.11}$$

where $I_i^{(j)}$ denotes the ionization rate coefficient for charge state j of species i, and $R_i^{(j)}$ denotes the recombination rate coefficients for ions of species i in charge state j. Both $I_i^{(j)}$ and $R_i^{(j)}$ are extracted from the OpenADAS database [40].

Equation (3.11) tells us that the number of ions of species i in charge state j *grows* as the ions in charge state $(j-1)$ are ionized into charge state j and ions in charge state $(j+1)$ recombine into charge state j. Similarly, $n_i^{(j)}$ *decreases* as ions in charge state j are ionized to state $(j+1)$ and ions in charge state j recombine and enter charge state $(j-1)$.

3.1.4 Current, electric field and poloidal flux

The self-consistent electric field in DREAM is evolved via the poloidal flux. The evolution of the electric field is governed by

$$\frac{\partial \psi}{\partial t} = -V_{\mathrm{loop}} = -2\pi R_m E_{\parallel}, \tag{3.12}$$

where ψ is the poloidal magnetic flux. The total plasma current density is a sum of the ohmic, hot and runaway component: $j_{\mathrm{tot}}(r) = j_{\Omega}(r) + j_{\mathrm{hot}}(r) + j_{\mathrm{RE}}(r)$. In DREAM, j_{tot} evolves according to the induction equation

$$j_{\mathrm{tot}}(r) = \frac{1}{2\pi\mu_0 r}\frac{\partial}{\partial r}\left(\frac{r}{R_m}\frac{\partial \psi}{\partial r}\right). \tag{3.13}$$

The total plasma current is given by the surface integral of j_{tot} over the poloidal cross section:

$$I_p = 2\pi \int_0^a j_{\mathrm{tot}} r \,\mathrm{d}r, \tag{3.14}$$

where a is radial coordinate of the last closed flux surface in the plasma, the factor 2π originates from integration over the poloidal angle, and r is the Jacobian for the radial coordinate.

For the boundary condition for ψ at the wall of the vacuum vessel, $\psi_{\mathrm{edge}} = \psi(r = a)$ where a is the radial coordinate of the plasma edge, and $\psi_{\mathrm{wall}} = \psi(r = r_0)$, where r_0 denotes the radial location of the conducting wall, are introduced. Both a and r_0 are defined at the machine midplane on the low-field side of the tokamak.

The wall poloidal flux ψ_{wall} couples to the conducting wall via the approximate edge-wall mutual flux inductance $M_{\text{we}} = \mu_0 R_m \ln(r_0/a)$, and we get $\psi_{\text{edge}} = \psi_{\text{wall}} - M_{\text{we}} I_p$ where I_p is the total toroidal plasma current defined in Eq. (3.14). The wall poloidal flux ψ_{wall} evolves according to

$$\frac{\partial \psi_{\text{wall}}}{\partial t} = V_{\text{loop}}^{(\text{wall})}, \tag{3.15}$$

where $V_{\text{loop}}^{(\text{wall})}$ is the loop voltage at the machine wall—a boundary condition for the poloidal flux. $V_{\text{loop}}^{(\text{wall})}$ can be either prescribed or modelled self consistently, yielding two options for the poloidal flux wall boundary condition:

1. *Prescribed boundary condition*: $V_{\text{loop}}^{(\text{wall})}$ is a prescribed time-dependent input, with the initial condition $\psi_{\text{wall}}(t = 0) = 0$.
2. *Self-consistent boundary condition with circuit equation*: $V_{\text{loop}}^{(\text{wall})}$ is modelled with an external inductance L_{ext} and a wall resistivity R_{wall}.

In the second boundary condition, the external inductance L_{ext} and the wall resistance R_{wall} are given by

$$L_{\text{ext}} = \mu_0 R_m \ln\left(\frac{R_m}{r_0}\right), \tag{3.16}$$

$$\tau_{\text{wall}} = \frac{L_{\text{ext}}}{R_{\text{wall}}}, \tag{3.17}$$

where μ_0 is the magnetic permeability in vacuum, and τ_{wall} is the characteristic wall time. This gives us

$$V_{\text{loop}}^{(\text{wall})} = R_{\text{wall}} I_{\text{wall}}, \tag{3.18}$$

where the wall current I_{wall} is obtained from $\psi_{\text{wall}} = -L_{\text{ext}}(I_p + I_{\text{wall}})$.

3.2 Soft

Soft (Synchrotron-detecting Orbit Following Toolkit) [11] is "...a synthetic radiation diagnostic designed to be used to study synchrotron radiation and bremsstrahlung from runaway electrons in tokamaks..." [41]. In essence, Soft calculates the synchrotron radiation received by a detector; this radiation depends on a number of parameters such as the energy of the radiating particles, their radial distribution and the position of the detector: all these dependencies and more are accounted for in Soft. Soft factors in the energy and momentum of the particles via their distribution function, which can either be a model distribution function defined in Soft, or a numerical distribution function from software specialized on modeling particles kinetically, such as Dream.

3.2.1 Phase space in Soft

By approximating particle orbits by their guiding centers, Soft allows for numerical efficiency without significant loss of accuracy as long as the Larmor radii of the particles are small: the length scale of the variations in the magnetic field must be much larger than r_L defined in Eq. (2.10). The following six guiding-center coordinates are used in SOFT [11]:

- ρ – maximum major radius visited by guiding-center along orbit
- τ – time coordinate: at $\tau = 0$ the guiding center is at ρ
- ϕ – toroidal angle of guiding center at $\tau = 0$
- $p_\parallel$ – guiding-center parallel momentum at $\tau = 0$
- $p_\perp$ – guiding-center perpendicular momentum at $\tau = 0$
- φ – gyro angle

The coordinates $p_\parallel$ and $p_\perp$ can be replaced by the momentum p and the pitch angle θ_p (or any of the other set of equivalent coordinates available in SOFT).

Another benefit of using the guiding center parameterization of phase space (as opposed to, for example, Cartesian coordinates), is that we only need to know the electron distribution function f_e at a single point on the particle orbit. Liouville's theorem states that the distribution function is constant along any trajectory in phase space, as long as variations in the plasma and magnetic field happen on a much longer timescale than that of the orbits: the distribution function can be taken as independent of time. In an axisymmetric magnetic field, f_e is also independent of the toroidal angle ϕ. Finally, assuming that the timescale of the gyration is faster than any time scales of interest in the problem considered, the distribution function is independent of the gyro angle φ of the orbit [19]. This leaves us with a distribution function which only depends on the radial location, the momentum, and the pitch of the particles: $f_e \equiv f_e(\rho, p_\parallel, p_\perp)$.

3.2.2 The synthetic detector and the response function

Let us denote the intensity of radiation measured by a detector by I. At a given time t, I is a function of the particle distribution function $f_e(\rho, p_\parallel, p_\perp)$. It is also a function of detector properties such as the detector area and detectors position relative to the emitting particle. The intensity I can be written as a triple integral over phase space, where the integrand can be separated into two factors. These two factors are the particle distribution function $f(\rho, p_\perp, p_\parallel)$, and the so-called *response function* or *Green's function* of the detector: $G \equiv G(\rho, p_\perp, p_\parallel)$. The response function G represents the emission received by the detector, and is defined in terms of integrals over the detector area, wavelength of the radiated emission, the toroidal angle, the orbit time and the gyro angle.

With $f(\rho, p_\perp, p_\parallel)$, and $G(\rho, p_\perp, p_\parallel)$, we can express the total amount of detected radiation I as

$$I = \int G(\rho, p_\perp, p_\parallel) f(\rho, p_\perp, p_\parallel) \mathcal{J} \,\mathrm{d}\rho \,\mathrm{d}p_\perp \,\mathrm{d}p_\parallel, \tag{3.19}$$

where the factor $\mathcal{J}$ is the momentum space Jacobian.

Since highly relativistic particles will emit radiation almost entirely in the direction of their velocity vector $\boldsymbol{v}$, we can assume that the radiated power per unit solid angle $\mathrm{d}P/\mathrm{d}\Omega$ from a particle is

$$\frac{\mathrm{d}P}{\mathrm{d}\Omega} = \frac{P(p_\perp, p_\parallel)}{2\pi} \delta(\hat{\boldsymbol{v}} \cdot \hat{\boldsymbol{n}} - 1). \tag{3.20}$$

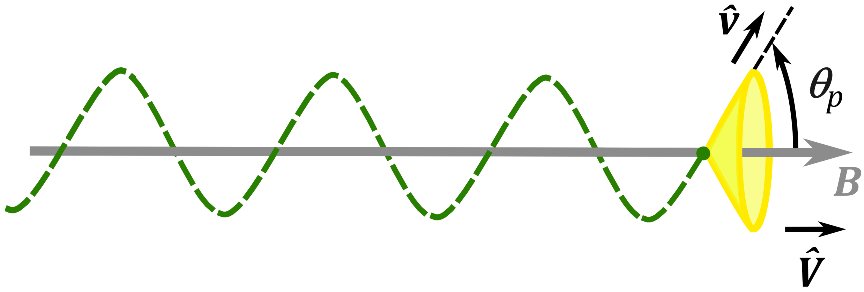

Figure 3.2: Schematic view of a helical electron trajectory (dashed green) around a magnetic field line (solid grey). Shown as black arrows are $\hat{\boldsymbol{v}}$ and $\hat{\boldsymbol{V}}$, unit vectors in the direction of the instantaneous particle velocity and guiding center velocity respectively. The cone with opening angle θ_p illustrates how the particle emits synchrotron radiation.

In Eq. (3.20), $P(p_\perp, p_\parallel)$ is the total power radiated by the particle, $\hat{\boldsymbol{v}}$ is the unit vector pointing in the direction of motion of the particle and $\hat{\boldsymbol{n}}$ is a unit vector along the line of sight of the detector; the delta function singles out the radiation emitted in the forward direction which is aligned with the line of sight. Transforming Eq. (3.20) to guiding center coordinates and integrating over the gyro angle φ gives

$$\int_0^{2\pi} \frac{\mathrm{d}P}{\mathrm{d}\Omega}\mathrm{d}\varphi = P(p_\perp, p_\parallel)\delta(\hat{\boldsymbol{V}}\cdot\hat{\boldsymbol{n}} - \cos\theta_p), \tag{3.21}$$

where $\hat{\boldsymbol{V}}$ is a unit vector in the same direction as the motion of the guiding center. This means that in the guiding center coordinate system, we can approximate the synchrotron radiation as being emitted from the guiding-center in a circular cone. The radiation is emitted in a thin shell—the thickness of the shell scales as $\gamma^{-1} = \sqrt{1 - v^2/c^2}$ where γ is the relativistic factor—and has an opening angle θ_p as depicted in Fig. 3.2. SOFT can use a similar model, the *cone model* where the radiation cone is assumed to be infinitely thin, to approximate the emitted synchrotron radiation. The cone model can significantly reduce the computational power required—it is typically faster than complete models by a factor of between 2-100.

Approximating the emitted radiation to a cone also provides some insight into which particles will emit radiation that the detector will register: the delta function in Eq. (3.21) tells us that only particles with trajectories such that $\hat{\boldsymbol{V}}\cdot\hat{\boldsymbol{n}} = \cos\theta_p$ will emit radiation towards the detector. Solving this equation reveals a so-called *surface-of-visibility*: a 3D surface in space from which particles can emit radiation which will be registered by the detector [11]. Since $\hat{\boldsymbol{V}} = \boldsymbol{B}/B$ to lowest order, the surface-of-visibility will be heavily dependent on the magnetic field configuration.

The Green's function G allows SOFT to account for the geometry of the magnetic field and detector setup when calculating the intensity of the radiation received by the detector. Since the configuration of these quantities have been shown to have a significant effect on synchrotron images [42, 43, 44], G is central to the resulting simulated data: it is not necessarily the most common particles in the distribution function which radiate most to the detector. This is mainly because most particles have very small pitch angles, such that $\xi = \cos\theta_p \sim 1$, and as we saw in Section 2.4.3

the amount of emitted synchrotron radiation is proportional to $\sin^2\theta_p = 1-\xi^2$. The Green's function allows us to determine which points in phase space contribute most to the radiation registered by the detector: it can be visualized as a contour plot, where the different levels reveal how much a particular region of phase space contributes to the radiation received by the detector. The particular point which contributes most is obtained by integrating G over the phase space parameters $(\rho, p_\perp, p_\|)$, and is referred to as the *dominant particle*. To include the effects of the particle energy and pitch on the dominant particle, we can multiply the Green's function by the distribution function before integrating over phase space; SOFT can output both the Green's function on its own (which then depends on the phase space variables, the magnetic field configuration and the detector setup) or the Green's function multiplied by the electron distribution function, which gives a function that is also dependent on the energy and pitch angle of the particles.

3.2.3 Polarized synchrotron light in SOFT

SOFT can output information about the polarization of the synchrotron radiation via the *Stokes parameters* I, U, V and Q. These parameters are functions of the complex radiation field vector given in Eq. (2.14):

$$
\begin{aligned}
I =& |\tilde{E}_\perp|^2 + |\tilde{E}_\||^2, \\
Q =& |\tilde{E}_\perp|^2 - |\tilde{E}_\||^2, \\
U =& 2\mathrm{Re}(\tilde{E}_\perp \tilde{E}_\|^*), \\
V =& -2\mathrm{Im}(\tilde{E}_\perp \tilde{E}_\|^*).
\end{aligned}
\tag{3.22}
$$

Here, I is the total intensity of emitted light. Using the Stokes parameters, we can also obtain the intensity of linearly polarized light L, given by $L = \sqrt{Q^2+U^2}$, and the polarization angle θ_{pol}, since $2\theta_{\mathrm{pol}} = \arctan(U/Q)$. Comparing L and I gives the fraction of linearly polarized light: $f_{\mathrm{pol}} = L/I$. We will not consider the fraction of circularly polarized light, given by V/I, since $V = 0$ for synchrotron radiation from runaways.

4 Simulations

Having introduced the necessary theory and numeric tools, we now turn our attention to the simulations performed for this thesis. Dream was used to model the current quench and runaway plateau in a JET disruption induced by a material injection. With a simplified model for the thermal quench and the second approximate electron model described in Section 3.1.2, where the cold electron population was treated as a fluid quantity, the number of free parameters in the model could be reduced and the computational cost decreased. Coupling the Dream output to Soft gave synthetic synchrotron data, thus providing additional synthetic diagnostic signals which could be compared to corresponding experimental data.

This chapter begins by presenting the experimental data from the JET discharge #95135 in Section 4.1. Section 4.2 provides descriptions of the JET disruption simulations in Dream and the subsequent Soft simulations, and we conclude the chapter by presenting the simulation results in Section 4.3.

4.1 Diagnostic data from JET discharge #95135

When modeling the JET disruption scenario, experimental data together with machine and detector properties was used to set up Dream and Soft. Dream mainly made use of plasma parameters from the discharge in question, while Soft required specifications on detector viewing directions, aperture sizes, etc.

Specific JET synchrotron detector properties are listed in Table 4.1; the experimental synchrotron images were captured with the camera in JET registering light in the IR spectrum (E5WC), while the MSE detector registered light in the visible spectral range. The spectral ranges given in Table 4.1 are those used in Soft; note that a single wavelength in the MSE diagnostics's spectrum was used.

Detector positions are given in (x, y, z)-coordinates, as is the viewing direction of the camera. For the MSE detector, the viewing directions of the first and last of its 25 lines-of-sight (LoS) are instead specified by R_t, the (major) tangential radius. R_t is measured from the axis of symmetry (i.e. from $R = 0$ where R is the major radial coordinate shown in Fig. 1.2), and tells us where a given LoS of the MSE detector is tangent to a circle with radius R_t and origin at $R = 0$. The field-of-view is the (half) opening angle of the camera; in the case of the MSE detector, it is that of the individual LoS.

In Fig. 4.1, a schematic top-down view of JET is given. The machine major and minor radii, R_0 and r_0 respectively, are both shown as arrows: R_0 is measured from the axis of symmetry while r_0 is measured from $R = R_0$ to the vacuum vessel walls

Table 4.1: JET synchrotron detector properties.

Detector	Camera (E5WC)	MSE
Spectral range	3.0-3.5 μm (IR)	660 nm (visible)
Number of lines-of-sight	1	25
Aperture size	1.4×10^{-3} m	1.0×10^{-3} m
Detector position	$(-0.89, -4.00, -0.33)$ m	$(-4.18, 0.83, 0.28)$ m
Viewing direction	(-0.50, 0.86, -0.01) m	-
R_t, MSE line-of-sight 1	-	3.87 m
R_t, MSE line-of-sight 25	-	2.69 m
Field-of-view	0.523 rad	0.001 rad

at $z = 0$. JET has a machine major radius of $R_0 = 2.96$ m, and its machine minor radius is $r_0 = 1.25$ m.

Both the camera and MSE detector positions, as well as their viewing directions, are also visualized in Fig. 4.1. Since the camera is viewing the left side of the tokamak, it registers synchrotron light from runaway electrons travelling counter-clockwise. As for the MSE detector, its first LoS is that closest to the outboard side; the innermost LoS (closest to the inner column) is number 25.

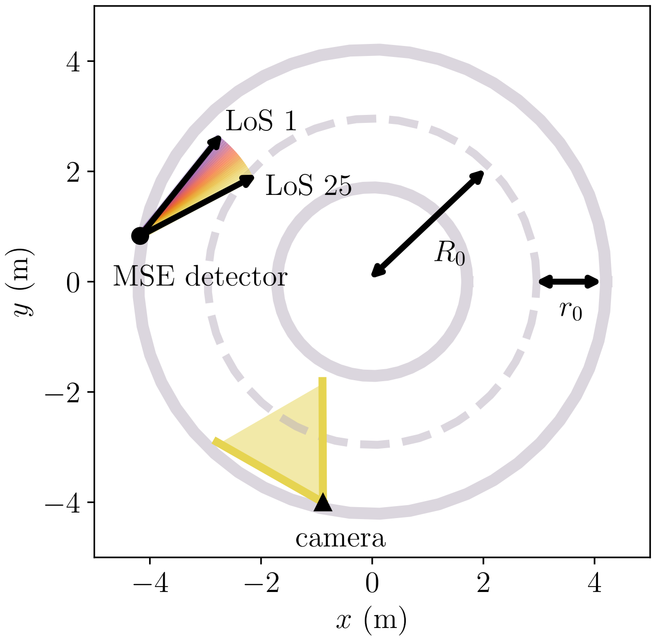

Figure 4.1: Schematic top-down view of JET. The grey contours outline the vacuum vessel walls and the machine major radius (dashed). To the top left in the figure is the MSE: the LoS for the MSE are numbered from 1 to 25, with the first LoS being closest to the outboard side of the vacuum vessel. Close to the bottom is the camera: its field-of-view is shown in yellow. Both the machine minor radius r_0 and the machine major radius R_0 are shown as arrows.

In this thesis, we modeled the disruption in JET discharge #95135. This was a deuterium discharge with a massive gas injection (MGI) induced disruption [45].

Argon gas—a total amount of $N_{\mathrm{Ar}} = 8 \times 10^{20}$ argon atoms—was injected at $t = t_{\mathrm{inj}} = 48.0\,\mathrm{s}$ in the experiment, and the resulting thermal quench caused a runaway beam to form. The amount of injected argon was calculated from the difference in pressure in the injection chamber before and (long) after the gas injection—where the volume of the chamber was 0.35 L—under the assumption that the temperature in the chamber was 300 K. The DREAM simulations used the argon density rather than the number of injected argon atoms. When converting between the two, the plasma volume $V_p = 100\ \mathrm{m}^3$ [14] was used: $n_{\mathrm{Ar}0} = N_{\mathrm{Ar}}/V_p = 8 \times 10^{18}\,\mathrm{m}^{-3}$. Here, we assumed that the argon was uniformly distributed over the plasma volume.

At $t = t_{\mathrm{spike}} = 48.0254\,\mathrm{s}$—about 25 ms after the argon injection—there was a local maximum (current spike) in the plasma current I_p (see Fig. 4.2a), after which the current quench begun; the current spike coincided with the thermal quench. At $t = 48.4\,\mathrm{s}$—circa 375 ms after the current spike—a deuterium SPI was fired, but note that the DREAM disruption simulations performed for this thesis did not extend past the time at which the SPI was fired. All times t in this chapter from here on are measured from the time of the current spike, so that $t \to t - t_{\mathrm{spike}}$, since the DREAM disruption simulations in this thesis began at the current spike.

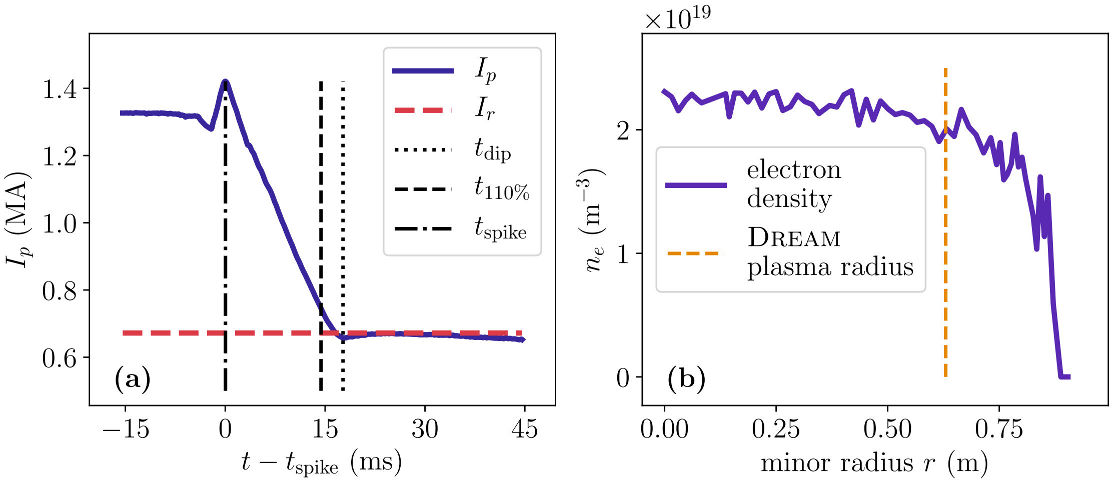

Figure 4.2: Experimental measurements from discharge #95135. In **(a)** is the total plasma current, while **(b)** shows the pre-disruption electron density profile.

Figure 4.2a shows the experimental plasma current I_p from $t = -15.4\,\mathrm{ms}$ and onward. At $t = 0$, we see the current spike where the plasma current is $I_{\mathrm{spike}} = 1.42\,\mathrm{MA}$. This is followed by an approximately linear decrease of the plasma current. After the current quench, I_p reaches the runaway plateau, stabilizing close to the plateau current value $I_r = 672\,\mathrm{kA}$; in order to obtain a single value I_r for the plasma current at the runaway plateau, I_r was estimated as the average of the current data between $t = 30\,\mathrm{ms}$ and $t = 36\,\mathrm{ms}$ (the deuterium SPI was fired approximately 357 ms after the current quench had ended).

Before I_p settles on the runaway plateau, it displays a local minimum, a small dip, at $t = t_{\mathrm{dip}}$. The experimental current quench time was defined as the time it took for the plasma current to decay from the current spike to the local minimum before the runaway plateau: $t_{\mathrm{CQ}} = t_{\mathrm{dip}} - t_{\mathrm{spike}} = 17.7\,\mathrm{ms}$. Both $t = t_{\mathrm{spike}}$ and $t = t_{\mathrm{dip}}$ are marked in Fig. 4.2a with vertical lines (dashed-dotted for $t = t_{\text{spike}}$ and dotted for $t = t_{\text{dip}}$), while the value of the runaway plateau current I_r is shown as a horizontal dashed line. The vertical dashed line marks $t_{110\%}$, where the plasma current is 10% larger than the runaway plateau current value: $I_r^{110\%} = 1.10 \cdot I_r$.

The pre-disruption electron density for discharge #95135 is shown in Fig. 4.2b as a function of the plasma minor radius r. Since discharge #95135 was a deuterium discharge, the electron density profile n_e in Fig. 4.2b was equal to the deuterium density profile n_{D}—we neglected any pre-disruption impurities that might have been present in the experiment when we modeled the disruption in Dream. Dream only used the data for $0 \leq r \leq 0.63\,\mathrm{m}$; the radial location of the cutoff in Dream is visualized by the horizontal dashed line in Fig. 4.2b. EFIT [46] data showed that the pre-disruption plasma radius was larger than the radius of the last closed flux surfaces at the various times shown in Fig. 4.3. The cutoff was then a means of estimating the post-disruption electron content. Even though the post-disruption electron density profile likely had a similar shape to that in Fig. 4.2b, we opted to use the cutoff profile with an abrupt transition to zero at the plasma edge. This was justified by the fact that the exact shape of the electron density was not expected to have a significant impact on the Dream simulations in this thesis, since hot-tail and Dreicer generation—which are sensitive to the electron density profile—were not modelled explicitly but accounted for via a prescribed runaway seed.

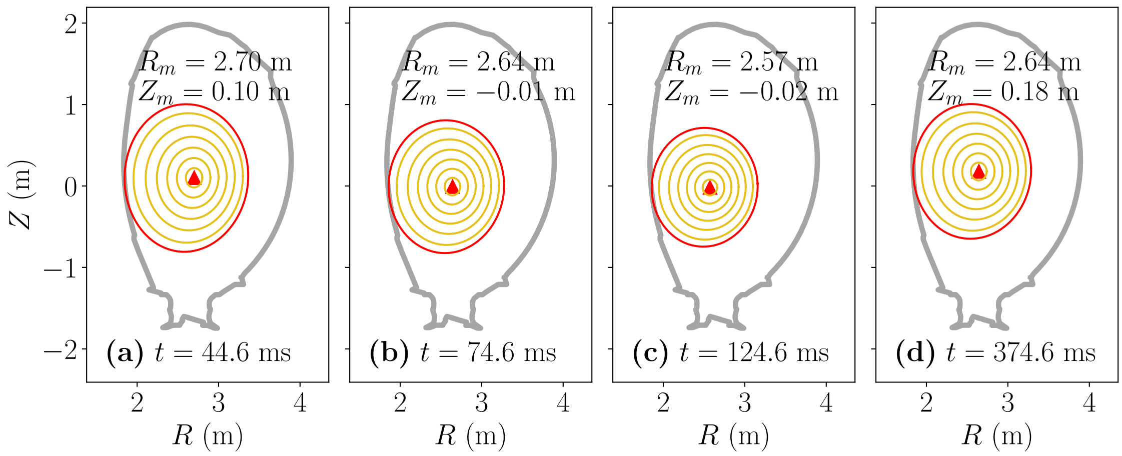

Figure 4.3: Flux surfaces from the EFIT magnetic fields for #95135. The gray contours outline the vacuum vessel, while the red contours depict the limiter flux surfaces. Red triangles mark the magnetic axes, located at coordinates (R_m, Z_m).

Magnetic data from EFIT [46] was used in Soft; the flux surfaces of the reconstructed magnetic fields used in this thesis are shown in Fig. 4.3, where each of Fig. 4.3a-d show the flux surfaces at a time in the experiment for which synthetic synchrotron data was generated with Soft. In Fig. 4.3, the magnetic flux surfaces are depicted as contours: the vacuum vessel wall is outlined in grey while the limiter flux surfaces are shown in red. Red triangles mark the magnetic axes located at coordinates (R_m, Z_m).

Table 4.2: Experimental data from discharge #95135.

B_0, magnetic field strength on axis	3.0 T
a, plasma (minor) radius	0.63 m
R_m, magnetic axis	2.64 m
I_{spike}, current spike	1.42 MA
t_{CQ}, current quench time	17.7 ms
I_r, runaway plateau current	672 kA
$I_r^{110\%}$, 110% of plateau current	738 kA
$t_{110\%}$, where $I_r^{110\%}$ occurs	14.5 ms
n_{Ar0}, injected argon	$8 \times 10^{18}\,\text{m}^{-3}$

Table 4.2 contains select experimental data from discharge #95135. The maximum plasma radius a and the radial coordinate for the magnetic axis, R_m, were extracted from the EFIT data visualized in Fig. 4.3b: the parameter a was used to set up the radial grid in DREAM, and R_m is a normalization constant (as in Eq. (3.12), for instance) when DREAM assumes cylindrical geometry, as was the case for all simulations in this thesis.

4.2 Modeling a JET massive material induced disruption and associated synchrotron data

The disruption and synthetic synchrotron data simulations in this thesis followed the same scheme:

1. Available machine and experimental data (e.g. pre-disruption plasma parameters and detector placements) was used to set up DREAM and SOFT.
2. Using the first approximate electron model in Section 3.1.2, the free parameters in DREAM were fitted so that the simulated current quench matched the experimental data.
3. The disruption was modeled in DREAM using an approximate thermal quench model (described in Section 4.2.1.1), and the second approximate electron model in Section 3.1.2.
4. Using the runaway distribution functions from DREAM, synthetic synchrotron data was generated with SOFT.

A more detailed description of how JET discharge #95135 was modeled in DREAM can be found in Section 4.2.1; the SOFT simulation procedures for the same discharge are presented in Section 4.2.2. Results from these simulations are discussed in Section 4.3.

4.2.1 Modeling disruptions in DREAM

Disruption simulations with DREAM performed for this thesis used an approximate model for the thermal quench: the temperature drop was assumed to happen instantaneously, i.e. so that t_{TQ} was much shorter than all other timescales of interest (such as the current quench time and ionization time). Under this assumption, the temperature was prescribed to be its post-disruption value from the start of the simulation and was assumed to be constant in time. To account for runaways which would otherwise have been created during the thermal quench, a runaway seed was prescribed. This approach also accounts for seed electron losses (mainly transport losses) during the thermal quench—the prescribed seed consists of any runaways which would have been created during and survived the thermal collapse. With the approximate thermal quench model described here, there were three free parameters to fit: the runaway seed, the post-thermal quench temperature and the amount of assimilated injected material.

Modeling the current quench in disruptions by assuming an instantaneous thermal quench and prescribing a runaway seed has previously proven successful; a similar approach was used to model the plasma evolution and runaway distribution functions for a massive material (argon) induced disruption in ASDEX Upgrade [47]. In Ref. [47], the electrons were modeled with the kinetic solver CODE (which models both the thermal and the runaway electrons kinetically), which was coupled to fluid simulations of the plasma from GO, yielding simulation times upwards of several weeks on a small cluster. In comparison, the DREAM disruption simulations performed for this thesis took about a day to run on a desktop computer.

The disruption in discharge #95135 was modeled in three stages in DREAM:

1. *Initialization simulation*: generated a steady-state ohmic plasma (not containing any runaways) by keeping the plasma parameters constant in time.
2. *Current quench simulation*: initiated from the initialization simulation and modeled the rapid decrease of the plasma current following the thermal collapse. Here, plasma parameters were allowed to evolve self-consistently in time.
3. *Plateau simulation*: modeled the runaway plateau by initiating another self-consistent simulation from the output of the current quench simulation.

The short initialization simulation did not model any part of the disruption: it was performed before the actual disruption simulations to ensure that these started from the correct plasma current value. Further details on the initialization simulations can be found in Appendix A.

In the subsequent current quench simulation, the electric field was allowed to evolve self-consistently, as were quantities such as the ion and electron densities. This simulation modeled the current quench and part of the runaway plateau phase. To model the plasma evolution during the runaway plateau, the plateau simulation with self-consistently evolved quantities was initiated from the final timestep of the current quench simulation output.

Below, Section 4.2.1.1 presents the approximate thermal quench model, while Section 4.2.1.2 discusses the current quench and plateau simulation. In Section 4.2.1.3, details specific to the simulation of the disruption in JET discharge #95135 are given.

4.2.1.1 Thermal quench model

The thermal quench is a very complex event which DREAM is not capable of modeling in a fully self-consistent manner, since it can not account for all the energy loss mechanisms in play during a thermal quench; DREAM cannot, for instance, model the stochastization of the magnetic field lines (which causes large transport of heat and particles) taking place during the early stages of a disruption. To overcome this limitation, and reduce the number of free parameters in the model, the thermal quench was approximated as instantaneous, with $t_{\mathrm{TQ}} = 0$: the transition from the initial to the post-disruption temperature was assumed to be made abruptly. When modeling disruptions in DREAM, we thus let the temperature be uniformly and constantly the post-disruption temperature T_f throughout the simulations. In doing so, we began the simulations right before the current quench (although remember that the disruption simulations were initiated from the pre-disruption ohmic plasma modeled by the initalization simulations).

In reality, the thermal quench time is not zero, and the rapid (but not instantaneous[1]) temperature drop typically results in the creation of runaways via hot-tail generation. In addition to this, the induced electric field gives Dreicer and avalanche generation which further contributes to the number of runaways created during the thermal quench. When assuming an instantaneous thermal quench, we accounted for the runaways that would have been generated during a temperature decay where $t_{\mathrm{TQ}} \neq 0$ by prescribing a *runaway seed*. In such a model, we assume that there is a sharp peak in the runaway generation rates during the thermal quench (predominantly due to hot-tail and Dreicer generation), resulting in a runaway seed. During the current quench and runaway plateau, avalanche generation is instead expected to dominate. With a runaway seed present in the simulation, the avalanche generation throughout the current quench and plateau phase could be modeled as usual: runaways in the seed can collide with thermal electrons and impart them with enough momentum to reach p_c.

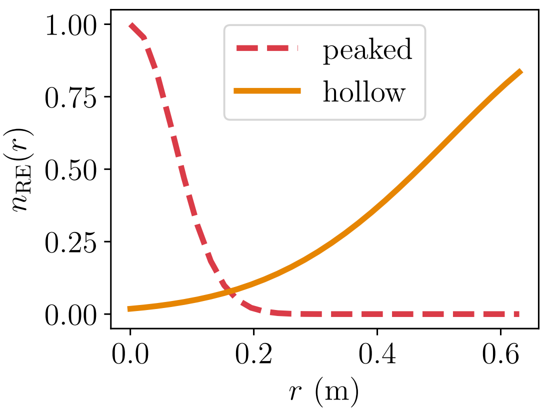

Figure 4.4: Runaway seed density profiles described by Eq. (4.1): in dashed red is profile where $r_{\mathrm{mean}} = 0$, while the profile shown in solid yellow has $r_{\mathrm{mean}} = 1.27a$ where $a = 0.63\,\mathrm{m}$. Both profiles have $A_{\mathrm{RE}} = 1$.

The general form of two runaway seed density profiles used in this thesis is given by

$$n_{\mathrm{RE}}(r) = A_{\mathrm{RE}} \cdot \exp\left[-\left(\frac{r - r_{\mathrm{mean}}}{r_w}\right)^2\right]. \tag{4.1}$$

Equation (4.1) describes a peaked density profile: r is the (minor) radial coordinate of the plasma measured from the magnetic axis to the plasma edge at $r = r_{\max} = a$ (so that $n_{\mathrm{RE}}(r)$ is defined for $0 \leq r \leq a$), r_{mean} is the mean radius (the radial location of the maximum) and r_w is the width of the peak. A_{RE} is a scaling factor (a constant) determining the size of the seed.

[1]In Ref. [48], JET thermal quench times were estimated to $0.085\,\mathrm{ms} \leq t_{\mathrm{TQ}} \leq 0.18\,\mathrm{ms}$.

In Fig. 4.4 we see two seed profiles, both with $A_{\mathrm{RE}} = 1$. The dashed red profile has $r_{\mathrm{mean}} = 0$ and is peaked around the magnetic axis, while the width of the peak is $r_w = 0.16a$ with $a = 0.63$m. If we instead let $r_{\mathrm{mean}} = 1.27a$ and $r_w = 0.63a$, we obtain the profile shown in solid yellow, in Fig. 4.4. This profile is 'hollow', i.e. it has its maximum close the plasma edge and goes to zero as $r \to 0$. Such a runaway density profile might arise when there is large radial transport of runaway electrons in the center of the plasma during the thermal quench. The Dream simulations of JET discharge #95135 in Section 4.2.1.3 used runaway seeds with shapes as in Fig. 4.4.

Although Dream is capable of modeling the transport of runaways, doing so would entail a lengthy analysis to estimate transport coefficients, which is outside the scope of this work. Instead of attempting to estimate these coefficients, we can account for the effect of radial transport of runaway electrons during the thermal quench by specifying the runaway seed density profile. By prescribing a runaway seed density with a certain shape, we effectively assume that any radial transport of the runaways occurs during the thermal quench, and that there is no radial transport during the remainder of the disruption.

Since the synchrotron spot shape is heavily dependent on the radial distribution of the runaways [49], experimental synchrotron images can provide hints as to which shape $n_{\mathrm{RE}}(r)$ should have in simulations of a given disruption scenario. Once the shape of the runaway seed density profile has been determined, the scaling factor A_{RE} must be fitted so that the simulated runaway plateau plasma current matches the experimental runaway plateau.

The other two free parameters in the thermal quench model described above—the post-disruption temperature and the amount of assimilated injected material—could be fitted by trying to match the simulated current quench to experimental data. For a given choice of temperature and amount of assimilated material, A_{RE} could typically be adjusted so that the simulation yielded the correct plateau current. However, not all sets of parameters were capable of reproducing a current quench time matching that of the experiment; adjusting A_{RE} allowed us to obtain the correct plateau current, while resulting current quench times were used to rule out points in parameter space. When scanning for the correct set of parameters, the fluid approximate electron model (the first model described in Section 3.1.2) could be used—such fluid simulations usually took less than one minute each.

4.2.1.2 Current quench and plateau simulations

In the current quench simulations in Dream—which modeled the decay of the plasma current and the beginning of the plateau phase—the prescribed low temperature and added impurities (self-consistently evolved) resulted in a decrease in plasma current. Since the electric field was also self-consistently modeled in Dream, the current quench induced an electric field in the plasma. Since avalanche multiplication was expected to dominate the runaway generation during the current quench and plateau simulation, only avalanche multiplication was modeled explicitly—contributions from hot-tail and Dreicer generation were accounted for via the prescribed runaway seed. To obtain a runaway electron distribution function, the kinetic runaway grid was used—the bulk electron distribution was modeled as a fluid quantity. This meant that the second approximate electron model in Section 3.1.2 was used in the current quench simulations.

After the current quench, the plasma is expected to stabilize in the sense that any changes in plasma quantities are expected to happen on a much longer time scale than during the thermal and current quench. The runaway electrons are however expected to go through pitch angle scattering, giving them larger pitch angles, as time progresses. To model the evolution of the runaway electron distribution function through the plateau phase, the current quench simulations in DREAM were extended with the plateau simulations. These were set up by copying most settings, and initiating the plasma quantities, from the current quench simulation—the simulation duration and time resolution were the only settings changed for the plateau simulations. Splitting the disruption simulations into one current quench simulation and one plateau simulation allowed for more efficient modeling: the relatively slow changes in the plasma during the plateau phase allowed for simulations with much larger time steps.

4.2.1.3 Modeling JET discharge #95135 in DREAM

JET discharge #95135 was modeled in DREAM from $t = 0\,\mathrm{ms}$ to $t = 374.6\,\mathrm{ms}$, i.e. for 374.6 ms after the current spike. To see the effect of radial redistribution of runaways during the thermal quench (assumed to originate from radial transport not explicitly modeled in this thesis) on the plasma current evolution in DREAM and the synchrotron data from SOFT, the disruption was modeled two separate times in DREAM: once with a peaked runaway seed according to Eq. (4.1) with $A_{\mathrm{RE}} = 8.1 \times 10^{15}$, $r_{\mathrm{mean}} = 0$ and $r_w = 0.16a$ (proportional to the dashed red profile in Fig. 4.4), and once with a hollow runaway seed according to Eq. (4.1) with $A_{\mathrm{RE}} = 1.9 \times 10^{13}$, $r_{\mathrm{mean}} = 1.27a$ and $r_w = 0.63a$ (proportional to the solid yellow profile in Fig. 4.4). Both profiles had $a = 0.63\,\mathrm{m}$. The runaway seed density profile was the only thing that differed between the two disruption simulations, which otherwise had identical settings.

Both disruption simulations used the same post-disruption temperature $T_f = 10\,\mathrm{eV}$ (within the range of typical post-disruption temperatures for JET [21]), which was prescribed constant in time and uniform in r. The amount of assimilated argon was $n_{\mathrm{Ar}} = 0.15 n_{\mathrm{Ar0}} = 1.2 \times 10^{18}\,\mathrm{m}^{-3}$, and was assumed to have a uniform radial profile, while the initial deuterium density was taken from the experimental data presented in Fig. 4.2b. Both ion species were modeled self-consistently, as was the electric field. The latter used the second (self-consistent) boundary condition described in Section 3.1.4, and the characteristic wall time—used to account for the finite resistivity of the conducting structures surrounding the plasma in DREAM as in Eq. (3.17)—was $\tau_{\mathrm{wall}} = 5\,\mathrm{ms}$ [50].

Synchrotron radiation losses were accounted for in the two disruption simulations. No Dreicer or hot-tail generation was included, since the prescribed runaway seeds accounted for runaways created during the thermal quench. As discussed in Section 4.2.1.2, the second approximate electron model was used, which meant that DREAM gave runaway electron distribution functions as output. Python scripts used when setting up DREAM to simulate the disruption in JET discharge #95135 can be found in Appendix B.1.

4.2.2 Simulations of synchrotron data from discharge #95135 with Soft

When setting up Soft, the detector properties presented in Section 4.1, Table 4.1, were used, together with the numerical magnetic data from EFIT (whose flux surfaces are shown in Fig. 4.3). Four synchrotron image simulations per runaway seed profile (i.e. a total of eight such simulations) were performed. The synchrotron image simulations used runaway distribution functions from the Dream disruption simulations to generate data.

To generate MSE diagnostic data from discharge #95135, 25 separate Soft simulations—one per line-of-sight—were performed; each such set of 25 simulations will here be referred to as one MSE simulation. All parameters except the viewing direction of the detector were identical for such a set of 25 simulations: the viewing direction was always such that it matched that of the LoS that was being simulated. As with the synchrotron images, four MSE simulations per runaway seed density profile were performed.

The different synchrotron images and MSE simulations used different runaway electron distribution functions. Each such simulation used a distribution function from Dream which was obtained from a timestep corresponding to $t = 44.6\,\mathrm{ms}$, $t = 74.6\,\mathrm{ms}$, $t = 124.6\,\mathrm{ms}$ or $t = 374.6\,\mathrm{ms}$ respectively. Similarly, each of the simulations used the magnetic data from EFIT which matched the times for which synthetic synchrotron data was generated.

An example of a Soft script used to simulate a synchrotron image and corresponding Green's function, as well as a script for simulating data for the first line-of-sight of the MSE, can be seen in Appendix B.2.

4.3 Results

By modeling the disruption in JET discharge #95135 with the two different seed profiles, the impact of the radial runaway density distribution on the diagnostic signals could be investigated. Even if neither of the two runaway seed density profiles succeeded in reproducing all features in the experimental data, some qualitative similarities could be seen in the results from both the respective seed profiles. In Section 4.3.1, results from the Dream simulations of the disruption in JET discharge #95135 are presented, while the synthetic synchrotron data from the subsequent Soft simulations is shown in Section 4.3.2.

4.3.1 Discharge #95135: results from Dream

The two Dream current quench simulations—which used the seed profile in Eq. (4.1) but with different r_{mean} and r_w values—gave the two respective total plasma current evolutions shown in Fig. 4.5. Here, I_p from the Dream simulation with a peaked seed profile (dashed red) and I_p from the simulation with a hollow seed profile (dash-dotted yellow) are shown together with the experimental plasma current (solid blue) for $t = 0\,\mathrm{ms}$ to $t = 44.6\,\mathrm{ms}$.

Table 4.3: Results from DREAM simulations of JET discharge #95135, shown with corresponding experimental values for comparison.

Seed profile	Hollow	Peaked	Experimental
I_r, runaway plateau current	664 kA	674 kA	672 kA
t_{CQ}, current quench time	17.6 ms	-	17.7 ms
$I_r^{110\%}$, 110% of plateau current	737 kA	748 kA	738 kA
$t_{110\%}$, where $I_r^{110\%}$ occurs	10.3 ms	14.2 ms	14.5 ms
I_{seed}, I_{RE} at $t = 0$	5.5 kA	0.2 kA	-

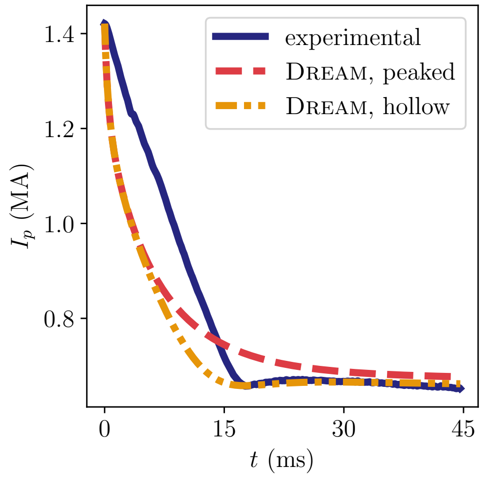

Figure 4.5: I_p from the DREAM current quench simulations of #95135 with the peaked seed density profile (dashed red) and the hollow seed density profile (dash-dotted yellow), shown together with the experimental plasma current (solid dark blue).

The simulated plasma currents reached runaway plateaus matching the experimental plateau quite well, but neither of the DREAM simulations succeeded in recreating the near linear decrease in I_p displayed in the experimental data. With the hollow runaway seed, DREAM was able to reproduce the local minimum before the runaway plateau, whereas the simulation with the peaked runaway seed density profile failed to do so. The runaway plateau current I_r for the simulated plasma currents are shown in Table 4.3 together with $I_r^{110\%}$, t_{CQ} and $t_{110\%}$. To obtain a single value for the runaway plateau current to compare to the corresponding experimental value, I_r was defined as the total plasma current value at the time where the runaway current component I_{RE} reached its maximum in DREAM. With the peaked runaway seed profile, the plateau current value $I_r = 674$ kA was reached at $t = 55.8$ ms. When the hollow runaway seed was used, this maximum was instead reached at $t = 38.8$ ms at which time the total plasma current was $I_r = 664$ kA. Since t_{CQ} is in this thesis defined as the time it takes for the current to decay from the current spike to the dip before the runaway plateau, this parameter was only defined for the simulation with the hollow runaway seed profile (the peaked seed profile did not give this local minimum in the plasma current). The parameter $t_{110\%}$ is however given for both DREAM simulations: this was the time it took for the plasma current to decay from the current spike to $I_r^{110\%} = 1.10 I_r$. Table 4.3 also shows the seed currents I_{seed} from the two simulations. The seed current is defined as the runaway component of the total current I_p at $t = 0$. The seed currents listed in Table 4.3 show that with the peaked seed profile, I_{seed} was more than one of magnitude larger than if the hollow seed profile was prescribed.

Figure 4.6 shows I_p from the two DREAM current quench simulations together with the decomposition of the two respective total plasma currents into the runaway and ohmic component I_{RE} and I_Ω. In Fig. 4.6a, the plasma currents from the simulation which used the peaked runaway seed are shown. Here, $t_{110\%}$ is marked by a vertical dash-dotted line. Figure 4.6b shows I_p and its decomposition into I_{RE} and I_Ω from the current quench simulation that used the hollow runaway seed profile. The dotted line in Fig. 4.6b marks t_{CQ} while the dash-dotted vertical line again marks $t_{110\%}$.

In Fig. 4.6 we see that the runaway component of the current was negligible at the beginning of both simulations; I_{RE} began to rapidly grow around around $t \sim 3\,\mathrm{ms}$ for the peaked runaway seed (Fig. 4.6a) and around $t \sim 10\,\mathrm{ms}$ when the hollow runaway seed profile was used (Fig. 4.6b), although the former displayed a slower growth in I_{RE}. If a large runaway seed survives the thermal quench (as was the case for the peaked seed profile, which had a seed current almost two orders or magnitude larger than for the hollow seed profile), I_{RE} will begin to grow earlier since the avalanche generation will be larger at an earlier stage. The runaway components soon overtook the ohmic components in both cases.

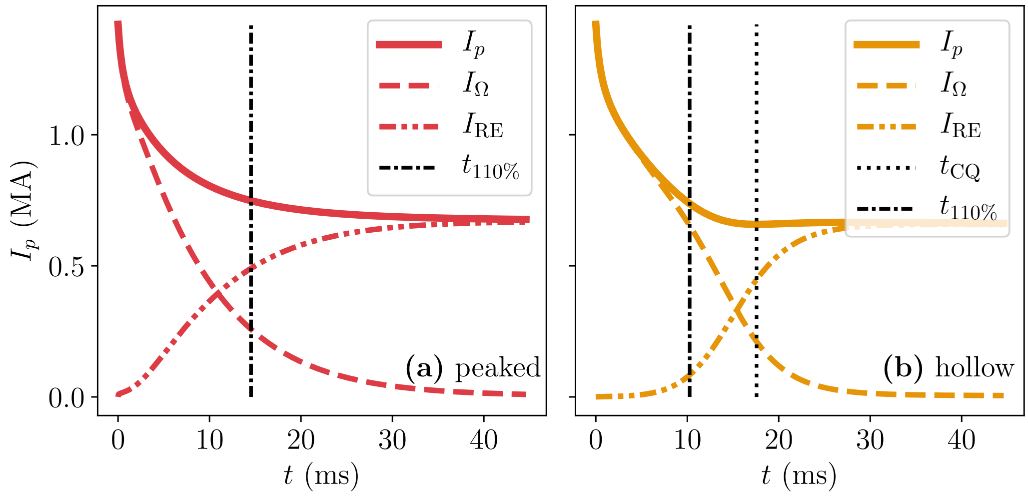

Figure 4.6: I_p from the DREAM current quench simulations of #95135, plus the decomposition into ohmic and runaway components. In **(a)** are the currents from the current quench simulation with the peaked runaway seed while **(b)** shows currents from the simulation with a hollow runaway profile.

The net increase in plasma current we see after the current quench in Fig. 4.6b is owed to the conducting wall. In DREAM, an electric field is induced in the wall. This field will then diffuse into the plasma, providing an energy boost to the electrons—the wall essentially acts as an energy reservoir which allows higher electric fields to be sustained for longer in the plasma. The extra energy from the wall gives higher runaway generation rates than would be possible if the wall was perfectly conducting (in which case no electric fields could be induced in it). In Fig. 4.6a, we see that the peaked runaway seed profile does not give the local minimum before the runaway plateau. This indicates that with such a seed profile, the wall never affects the runways (and vice versa) since the relativistic electrons are centered close to the magnetic axis.

Figure 4.7 shows normalized runaway density profiles at a few selected times from the simulations; Fig. 4.7a shows the normalized $n_{\mathrm{RE}}(r)$ from the disruption

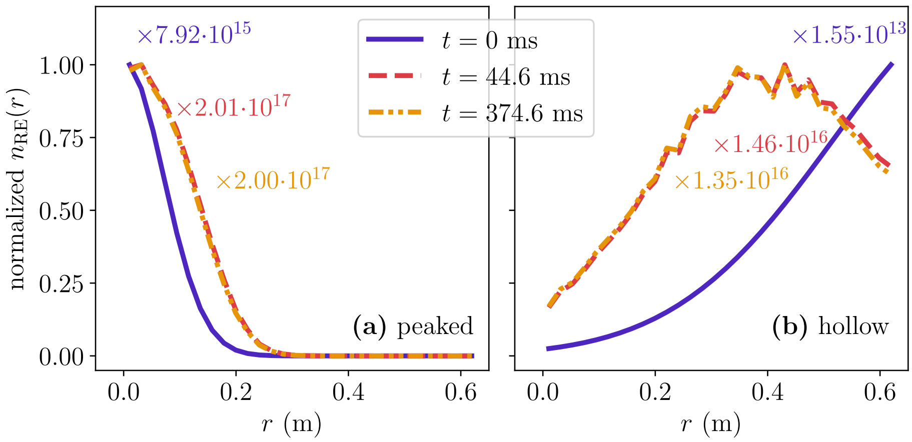

Figure 4.7: Normalized runaway density profiles from the DREAM disruption simulations. In **(a)** are density profiles from the simulations with the peaked seed density profile, while **(b)** shows the normalized $n_{\mathrm{RE}}(r)$ from DREAM simulations where the hollow runaway seed density profile was used.

simulation where the peaked runaway seed density profile was used while Fig. 4.7b shows the same thing for the disruption simulation with the hollow runaway seed profile. The normalized runaway seed density profiles, i.e. $n_{\mathrm{RE}}(t=0,r)$, are shown in solid blue. With the hollow runaway seed, the runaway density profile remained hollow, although the maximum of the distribution moved toward the magnetic axis as the disruption progresses. The runaway density profiles from the disruption simulation with the peaked runaway seed retained their maximum value close to $r=0$. In both cases the shapes of the density profiles changed very little during the latter part of the simulations.

Runaway distribution functions f_{RE} from the DREAM disruption simulation where the peaked seed density profile was used are shown in Fig. 4.8a-c, while Fig. 4.8d-f shows the corresponding distribution functions from the simulation where a hollow seed profile was prescribed. The distribution functions in Fig. 4.8 are shown for $t = 44.6\,\mathrm{ms}$ at a few radial points, and we see that the perpendicular momentum component is such that $p_\perp < 16\ m_e c$ for all values of r shown. For the peaked seed profile, the parallel momentum is such that $p_\parallel < 100\ m_e c$ at $r = 0.01\,\mathrm{m}$, while $p_\parallel$ reaches almost all the way to the grid limit at $p_\parallel = 160\ m_e c \sim 80\,\mathrm{MeV}$ at $r = 0.30\,\mathrm{m}$. At the outmost radial point $r = 0.63\,\mathrm{m}$ (Fig. 4.8c), there are no runaways.

With the hollow seed, the parallel momentum reaches all the way to the runaway-grid limit at $p_\parallel = 160\ m_e c$ for $r = 0.01\,\mathrm{m}$ and $r = 0.30\,\mathrm{m}$. In contrast to the simulation with the peaked seed profile, we do get runaways at $r = 0.63\,\mathrm{m}$ (Fig. 4.8f): their parallel momentum is just below the grid limit at $p_\parallel = 160\ m_e c$.

The fact that the parallel momentum is lower with the peaked seed profile than with the hollow seed profile is due to the fact the conversion into runaway current is faster with the peaked seed profile (as shown in Fig. 4.6). This leads to a lower induced electric field during the current quench, and thus less acceleration of the runaways.

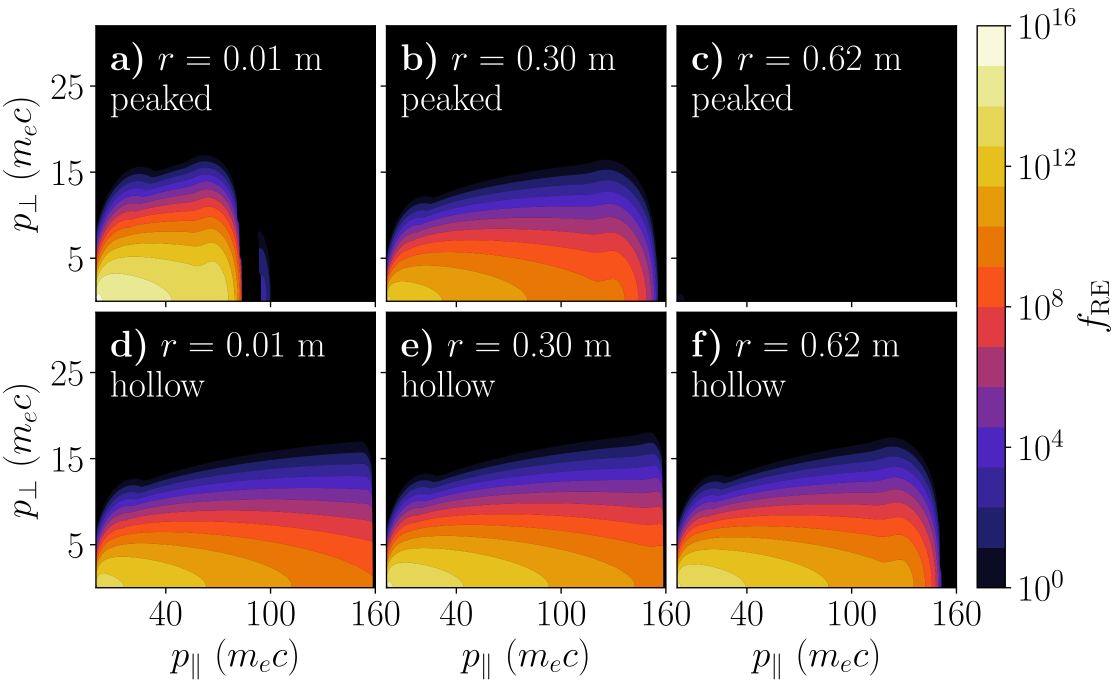

Figure 4.8: Runaway distribution functions at $t = 44.6\,\mathrm{ms}$ for a few values of r. The top row shows distribution functions from the DREAM disruption simulation with peaked seed profile; the blue sliver close to $p_\parallel = 100\ m_e c$ in **(b)** is a numerical artifact. Corresponding distribution functions from the simulation with the hollow seed profile are shown in the bottom row.

4.3.2 Discharge #95135: results from SOFT

Even though both the peaked and the hollow runaway seed profile fared well in reproducing the plasma current evolution seen in the experimental data, the synthetic synchrotron data from SOFT was more sensitive to the radial distribution of the runaway electron population. This is evident in both the synthetic synchrotron images presented in Section 4.3.2.1 and the synthetic MSE diagnostic data discussed in Section 4.3.2.2. In Section 4.3.2.3, we show how the radial distribution of the runaway electrons impacts the evolution of the maximum intensity of the synchrotron spot.

4.3.2.1 Synchrotron images

Synthetic synchrotron images from SOFT are shown together with the corresponding experimental camera images in Fig. 4.9. The first row, Fig. 4.9a-d, shows synthetic synchrotron images which were created using runaway distribution functions from the DREAM disruption simulation with the peaked runaway seed profile. In the middle row (Fig. 4.9e-h) are images which were created using the hollow seed profile. The experimental synchrotron images are displayed in the bottom row (Fig. 4.9i-l): Fig. 4.9i was captured shortly after the argon gas was injected, while Fig. 4.9l was captured as the deuterium SPI was fired, but before the pellet shards entered the plasma. Note that the horizontal distortion in the middle of the experimental synchrotron images is an artifact from the hardware setup; JET camera images are constructed from signals from two separate fibers.

The experimental synchrotron image in Fig. 4.9i indicates that early in the disruption, the runaway beam is narrow and centered around the magnetic axis. Later, as Fig. 4.9j and Fig. 4.9k suggest, the beam grows in intensity and size while migrating toward the inboard side (high-field-side) of the tokamak: the synchrotron spot moves toward the right edge of the camera image. In Fig. 4.9l we see that when the SPI is fired, the synchrotron spot is a narrow crescent at the right edge of the camera's field-of-view.

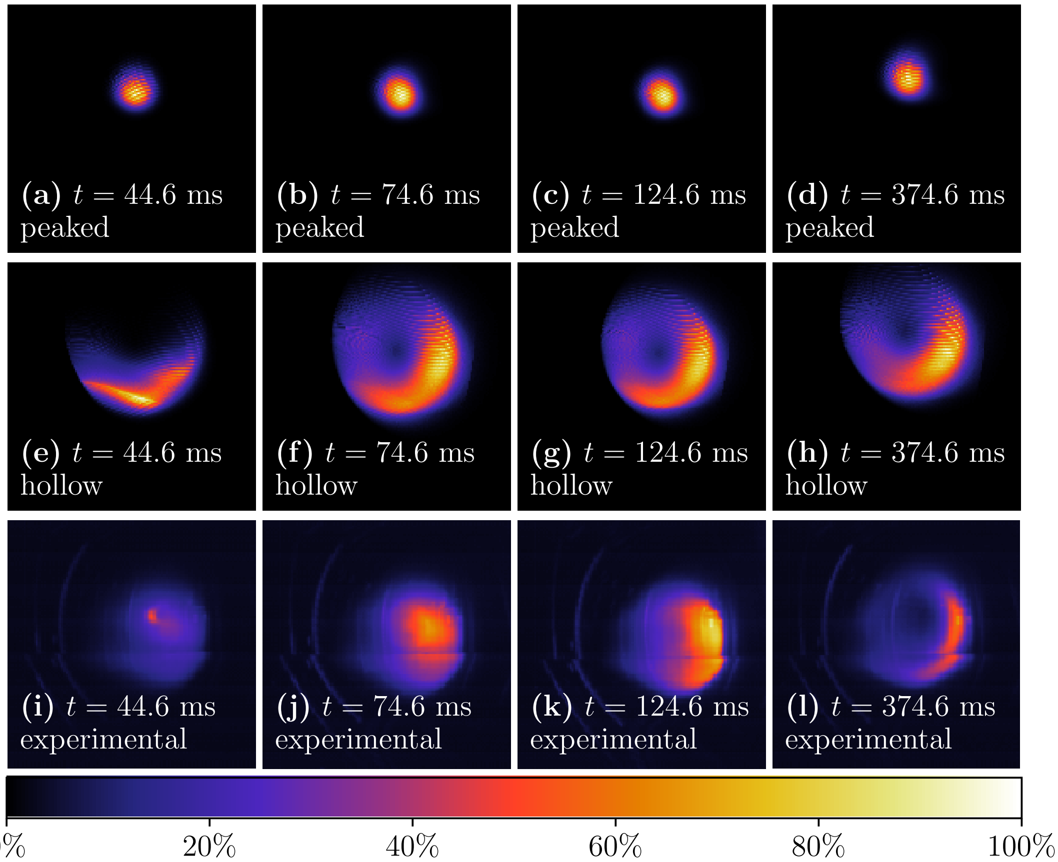

Figure 4.9: Synthetic synchrotron images from Soft: **(a)**-**(d)** were generated using a peaked seed profile while **(e)**-**(h)** were created using f_{RE} from the Dream disruption simulation with the hollow runaway seed profile. The corresponding experimental synchrotron images are shown in **(i)**-**(l)**.

As shown in Fig. 4.9a-d, the peaked runaway seed gives images where the synchrotron spot does not change significantly as time progresses: the bright spot moves slightly in the vertical direction, and its intensity varies some, but the shape remains the same in all four synthetic synchrotron images. Something similar can be said about the synchrotron images in Fig. 4.9e-h, which were generated with the hollow runaway seed density: although the the spot changes its size, intensity and rotates in the poloidal direction between the images, it remains in the shape of a crescent. This crescent shape is qualitatively similar to especially the experimental synchrotron spot in Fig. 4.9l, but also to the less distinct crescent shaped synchrotron spot in Fig. 4.9k. Comparing the synchrotron images from $t = 44.6\,\text{ms}$ we see that the peaked seed profile (Fig. 4.9a) results in the same kind of synchrotron spot as the experimental image in Fig. 4.9i displays—it is small and centered close to the magnetic axis.

All in all, the synthetic synchrotron images in Fig. 4.9a-h show that neither the peaked nor the hollow runaway seed profile is able to reproduce all four experimental synchrotron images in Fig. 4.9i-l. This indicates that the runaway density is redistributed as the disruption progresses: initially, it is narrowly peaked around the magnetic axis but gradually changes shape into a hollow profile with its maximum near the outer edge of the plasma.

Green's functions from the simulations of the synchrotron images in Fig. 4.9a-h are shown in Fig. 4.10. These Green's functions have been multiplied with the respective runaway distribution functions used when generating the corresponding synthetic synchrotron images, and integrated over the radial phase-space coordinate. The brightest areas of the contour plots in Fig. 4.9 reveal which parts of momentum space contributed most to the images in Fig. 4.9a-h.

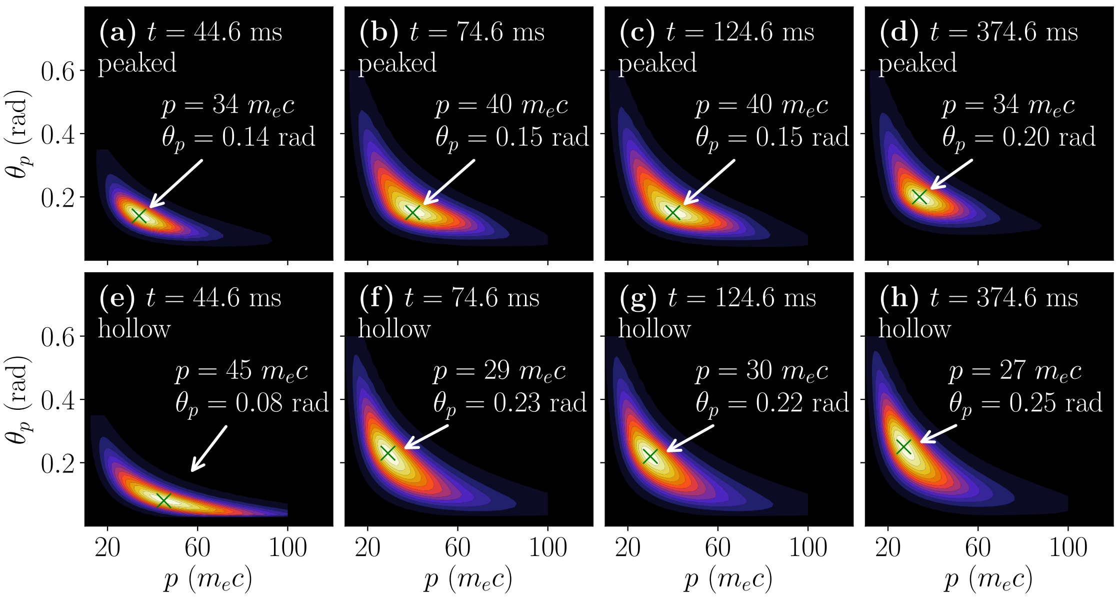

Figure 4.10: Green's functions from the synthetic synchrotron image simulations in SOFT, multiplied by f_{RE} and integrated over the radial coordinate. The green crosses mark the dominant particles.

We see in Fig. 4.10a-d that for the peaked seed profile, the dominant energy increased between $t = 44.6\,\text{ms}$ and $t = 74.6\,\text{ms}$. This indicates that the particles have been accelerated by an electric field present in the plasma. The dominant energy remained the same at $t = 124.6\,\text{ms}$ as at $t = 74.6\,\text{ms}$. At $t = 374.6\,\text{ms}$ the dominant particle had decreased its energy to the same value as at $t = 44.6\,\text{ms}$ due to synchrotron radiation losses. With the hollow seed profile, we see in Fig. 4.10e-h that the dominant particle decreased in energy as the disruption progressed: this decrease in energy is due to synchrotron radiation losses. From the dominant pitch angles from the two disruption simulations we gather that the runaway electrons seem to undergo pitch angle scattering as the disruption progresses, as expected from runaways in plasma where argon has been injected.

4.3.2.2 MSE diagnostic data

In Fig. 4.11 we see the simulated and experimental MSE diagnostic signals. Here, each of Fig. 4.11a-d show the intensity I (normalized to the maximum value of each intensity signal), the fraction of linearly polarized light f_{pol}, and the polarization angle θ_{pol} for the various times for which we generated the synthetic synchrotron images in Fig. 4.9: Fig. 4.11a corresponds to $t = 44.6\,\mathrm{ms}$, Fig. 4.11b to $t = 74.6\,\mathrm{ms}$, etc. The experimental data is shown in blue (dashed with diamond markers), the data from the SOFT simulations using distribution functions from the DREAM disruption simulation where the peaked runaway seed density profile was used is shown in red (circle markers) and data generated using the f_{RE} from the disruption simulation where the hollow seed profile was used is shown in yellow (triangle markers). Due to the time resolution of the MSE diagnostic, the experimental data shown in Fig. 4.11 was captured at $t + 0.5\,\mathrm{ms}$. Comparing the data at $t - 0.5\,\mathrm{ms}$ and $t + 0.5\,\mathrm{ms}$, we saw that there were no significant changes in the signals during this time. Furthermore, some channels of the MSE diagnostic in JET did not give reliable readings, which is why these data points are not included in the plots.

Interpreting synchrotron data from the MSE diagnostic

In JET, the MSE diagnostic registers not only synchrotron radiation emitted in the LoS of the detector, but any other radiation (within the relevant spectral range) in its LoS as well (this might for instance include synchrotron radiation reflected off the walls of the tokamak). Due to this, the experimental intensity I is not a reliable metric for synchrotron light. Since synchrotron light is mainly linearly polarized, f_{pol} can be an important indication as to whether the MSE detector picks up synchrotron radiation or something else, since $f_{\mathrm{pol}} = L/I$, where L is the intensity of the linearly polarized radiation. However, since light reflected off the vacuum vessel walls can also be linearly polarized, and synchrotron radiation can be unpolarized, some caution is required when interpreting the experimental f_{pol} signal.

The experimental measurements of the polarization angle θ_{pol} are very accurate: the MSE diagnostic is capable of measuring θ_{pol} to within 0.15° [29]. A lower bound for the experimental f_{pol}, below which the uncertainty of the measurement of θ_{pol} was estimated to be significant (since there is then only a small amount of linearly polarized light), was applied to the experimental polarization angle data: θ_{pol} on channels where the detector in JET registered $f_{\mathrm{pol}} \leq 0.1$ have been excluded from the plots in Fig. 4.11.

In Section 2.4.2 we established that the synchrotron radiation from runaway electrons is mainly linearly polarized in the direction perpendicular to the plane spanned by $\boldsymbol{v} \times \boldsymbol{B}$. This implies that if the MSE detector registers horizontally polarized light, it sees the top or bottom of the emission cone depicted in Fig. 3.2 (emitted by particles with velocities in the vertical direction), while vertically polarized light (i.e. light with $\theta_{\rm pol} = 90°$) implies that the detector instead sees the sides of the emission cone [30].

Comparing the field-of-view of the MSE and the camera (visualized in Fig. 4.1) we note that the camera's field-of-view extends almost all the way to vacuum vessel wall on both sides of the machine major radius. The MSE detector, however, only sees the vacuum vessel from close to the outer wall and just past the machine major radius. Thus, we do not expect the MSE detector in JET to detect light from the right-hand parts of the synchrotron spots shown in Fig. 4.9, since these are either centered close to or located on the inboard side of the machine major radius.

The total intensity I

The experimental intensity signals in Fig. 4.11 (dashed blue, diamond markers) are generally low on the outer channels. This indicates that the signal registered by the MSE diagnostic in JET on theses channels does not originate from the synchrotron spots shown in Fig. 4.9i-l. The synthetic synchrotron data corroborates this: data from the Soft MSE simulations indicate that no synchrotron light is registered on the outer channels.

If Dream distribution functions from the disruption simulation with the peaked runaway seed was used, Soft generally gave intensities I which grew monotonically towards the innermost channels, indicating that the synthetic MSE diagnostic in this case registers light from the left half of the synchrotron spots depicted in Fig. 4.9a-d. The exception from this trend is seen in Fig. 4.11a, where we see a local minimum in the intensity around channel 21 (owed to the intersection of the inner MSE channels and the synchrotron spot). When Dream distribution functions from the disruption simulation with the hollow runaway seed were used, the synthetic MSE diagnostic intensity data instead displayed growing intensities with local minima on the inner channels at all times depicted in Fig. 4.11. This minimum in I likely corresponds to the hollow center of the synchrotron spots in Fig. 4.9e-h.

In Fig. 4.11a and Fig. 4.11b, we see that the peaked runaway seed profile more accurately reproduces the trends in the experimental signal than the hollow seed profile, while the experimental intensities in Fig. 4.11c and Fig. 4.11d are better reproduced by the hollow seed profile. The intensity data thus seems to support the conjecture that the runaway electron population gets redistributed, from a profile which is peaked around the magnetic axis to a hollow profile with its maximum close to the plasma edge, as the disruption progresses.

The fraction of polarized light and the polarization angle

We established in Section 2.4.2 that synchrotron radiation only consists of unpolarized and linearly polarized components. For the synthetic MSE diagnostic data from Soft (which only simulated synchrotron radiation), this means that the total intensity I is the sum of the linearly polarized component and the unpolarized component, while in the experimental data, I is comprised of various unrecognized background sources with unknown polarization. This implies that comparisons of the experimental and simulated $f_{\rm pol} = L/I$ are ambiguous since the experimental $f_{\rm pol}$ is a ratio between two signals composed of unknown amounts of synchrotron ra-

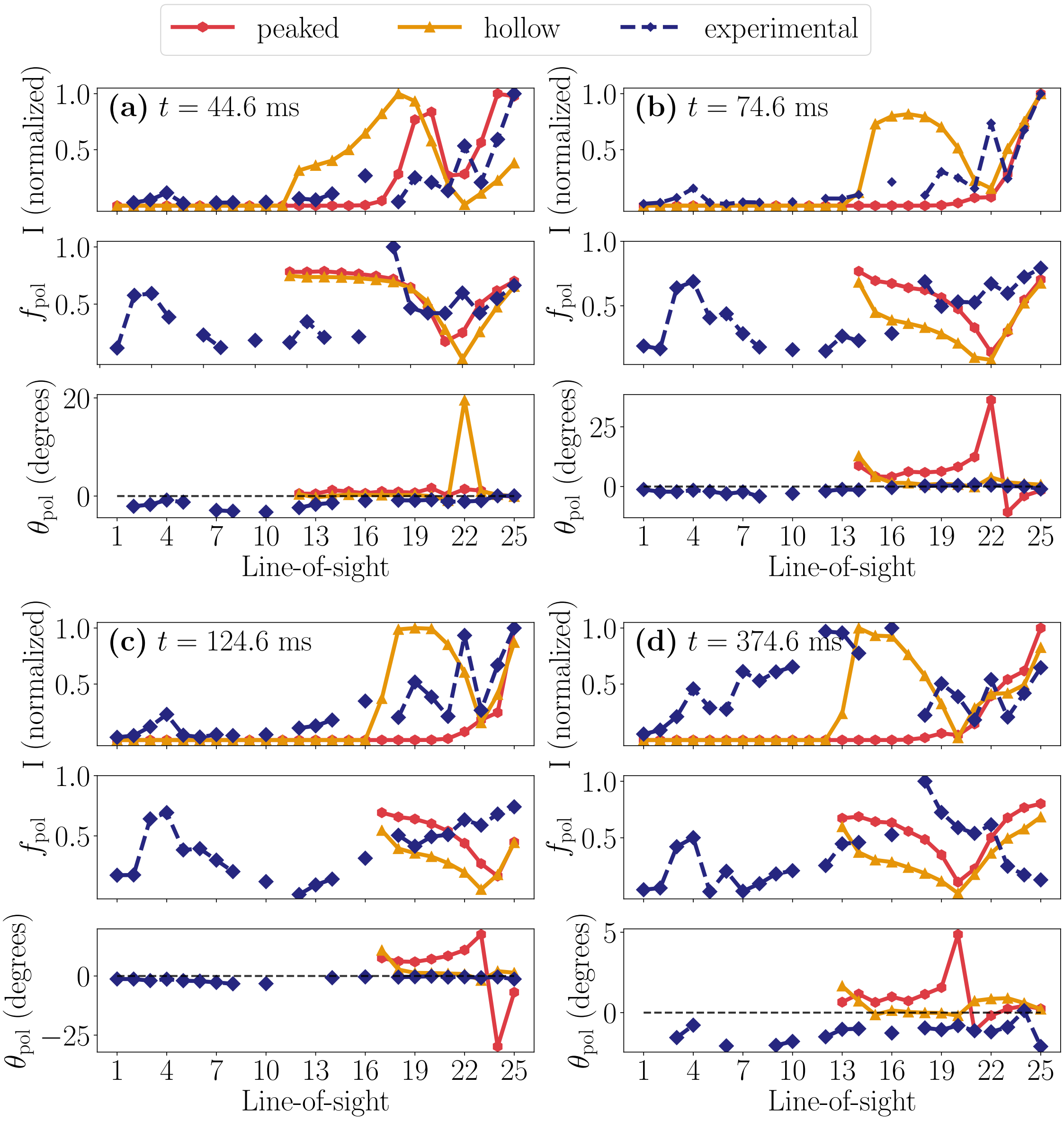

Figure 4.11: Synthetic and experimental MSE diagnostic signals for #95135. Data for the peaked profile is shown in red with circular markers, the hollow profile in yellow with triangular markers and the experimental data in red (dashed) with diamond markers. A dashed horizontal line (black) marks $\theta_{\mathrm{pol}} = 0°$ in each of the figures displaying the polarization angle.

diation, while for the synthetic data from SOFT, we know that both L and I measure only synchrotron radiation from runaway electrons. The poor agreement between the experimental and synthetic f_{pol} could indicate that there is polarized light pollution from unknown background sources in the experimental measurements.

When it comes to the experimental polarization angle, it is clear that the registered light has horizontal polarization: $\theta_{\text{pol}} = 0° \pm 4.5°$ for the experimental data in all four of Fig. 4.11a-d. The same is true for the synthetic polarization angles: most simulated polarization angles in Fig. 4.11 remain in the vicinity of $\theta_{\text{pol}} = 0°$, although note the different scales on the y-axes of the θ_{pol} plots. As we established above, this implies that the detector registers light from the top and bottom of the emission cone. However, both the peaked and the hollow runaway seed gave at least one polarization angle data point which deviated significantly from the others. These data points often coincided with low fractions of polarized light, where the polarization angle is very sensitive to small changes in the SOFT resolution parameters. Furthermore, we expect to see a transition from $\theta_{\text{pol}} = 0°$ to $\theta_{\text{pol}} = 90°$ at $f_{\text{pol}} = 0$ [51], which in SOFT might result in a gradual change from $\theta_{\text{pol}} = 0°$ as the fraction of linearly polarized light approaches zero. Due to the reasons mentioned above, the value of θ_{pol} from SOFT is not really reliable for low values of f_{pol}, and caution is required when interpreting this signal.

4.3.2.3 Intensity evolution

Another means of evaluating the agreement between experimental and simulated synchrotron data is to compare the evolution of the synchrotron spot's intensity over time. To obtain the simulated intensity evolution, a Green's function from SOFT was multiplied with the runaway distribution function and Jacobian (which was given as output by DREAM) at each timestep in the two respective DREAM disruption simulations. The intensity at a given timestep was then the sum of this product over the three phase space coordinates (r, p, θ_p).

Figure 4.12 displays the intensity of the brightest pixel in the experimental synchrotron images from JET discharge #95135 between $t = 20\,\text{ms}$ and $t = 420\,\text{ms}$ (solid blue) together with the simulated intensities for $t = 0\,\text{ms}$ to $t = 374.6\,\text{ms}$: the intensities from the disruption simulations are shown in dashed red (peaked seed profile) and dash-dotted yellow (hollow seed profile). All three intensities have been normalized against their respective maximum values since we are interested in the trends in intensity evolution rather than the absolute intensity values. The times corresponding to those at which the synchrotron images in Fig. 4.9 were captured or simulated are marked by the vertical dashed lines numbered **(1)**-**(4)**.

In Fig. 4.12 we see that the experimental intensity grows until it reaches a maximum at $t = 130.6\,\text{ms}$, after which it decreases again. This observation matches the experimental synchrotron images on the bottom row in Fig. 4.9: the synchrotron spot is brightest in Fig. 4.9k, captured at $t = 124.6\,\text{ms}$. Like the experimental data, the simulated intensities grow—with the hollow seed profile, the initial growth in intensity is similar to that seen in the experimental data—until they reach a maximum, after which they begin to decrease again. For the simulated intensities, however, the respective maxima are reached at later times than for the experimental data: with the peaked seed profile, the maximum intensity is reached at $t = 250.3\,\text{ms}$

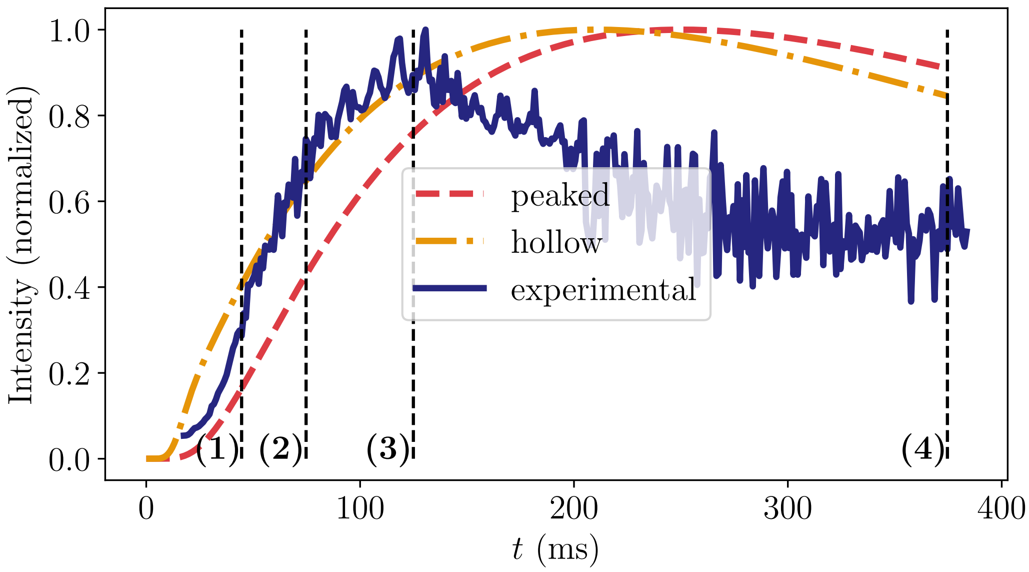

Figure 4.12: Simulated intensity evolution for #95135, modelled using a Green's function from SOFT and distribution functions from DREAM. The experimental intensity evolution for the corresponding interval of time is shown in dashed red. All intensities have been normalized against their respective maximum values. Each of the horizontal lines at **(1)**-**(4)** marks a time for which a synchrotron image was simulated.

while for the hollow seed profile, the intensity is largest at $t = 210.3\,\text{ms}$. Apart from this, the peaked and the hollow runaway seed gave similar intensity evolutions with rapid initial growth followed by a slower decline in the intensities.

5

Variation of the simulation parameters

The disruption simulations in this thesis were successful in reproducing many features of the experimental plasma current from JET discharge #95135, even with the simplified treatment of the thermal quench and the corresponding seed dynamics. One significant advantage of the simplified thermal quench model was that it had relatively few free parameters: we needed to fit the post-disruption temperature, the amount of assimilated injected material and the magnitude and radial distribution of the runaway seed profile.

As the results in Section 4.3.2 indicate, the runaway seed density profile greatly impacts the synchrotron spot shape. This is further corroborated in Section 5.1, where we investigate the effect of four different seed profiles on the plasma current evolution from Dream and the synthetic synchrotron images from Soft. In Section 5.2 we compare a synthetic synchrotron image generated using a model distribution function to a corresponding synthetic synchrotron image where a distribution function from Dream was used.

We established in Section 4.2.1.1 that many sets of parameters could yield the desired runaway plateau current, but that not all such parameter sets successfully reproduced the correct current quench dynamics. To see how the post-disruption temperature and the amount of assimilated argon impacted the resulting plasma current evolution, a number of simulations were performed where these two parameters were varied. Results from these simulations are presented in Section 5.3. In the same section, we also investigate how the conducting wall impacts the plasma current evolution, and the effect that the initial current density profile and the inclusion of Dreicer generation rates has on the plasma current in Dream. Finally, Section 5.4 provides a short discussion on remaining issues and prospects.

5.1 Impact of the runaway seed profile on plasma current and synthetic synchrotron data

Which shape the runaway seed profile has significantly impacts the resulting synthetic synchrotron images, as the results from Soft presented in Section 4.3.2.1 show. The plasma current from Dream is also sensitive to the runaway density profile, but perhaps less obviously so: in Section 4.3.1 we saw that only the disruption simulation with the hollow runaway seed profile gave a local minimum in the plasma current after the current quench, while both the peaked and the hollow seed profiles gave current quench times and plateau currents matching the experimental data quite well. We used the peaked and hollow runaway seed profiles in the DREAM disruption simulations described in Section 4.2.1.3 since the experimental synchrotron images seemed to suggest that this was how the runaways were distributed during the experiment. To see whether or not these seed profiles were the only ones capable of yielding simulation results matching the experimental data, two more disruption simulations were performed. These simulations had a uniform seed density profile and a power profile respectively, allowing us to compare results from disruption simulations with the following four different seed profiles:

$$n_{\mathrm{RE}}(r) = A_{\mathrm{RE}}, \qquad \text{uniform} \tag{5.1}$$

$$n_{\mathrm{RE}}(r) = A_{\mathrm{RE}} \cdot \left[0.63 - \left(\frac{r}{1.43 \cdot a}\right)^3\right], \qquad \text{power profile} \tag{5.2}$$

$$n_{\mathrm{RE}}(r) = A_{\mathrm{RE}} \cdot \exp\left[-\left(\frac{r}{0.16 \cdot a}\right)^2\right] \qquad \text{peaked profile} \tag{5.3}$$

$$n_{\mathrm{RE}}(r) = A_{\mathrm{RE}} \cdot \exp\left[-\left(\frac{r - 1.27 \cdot a}{0.63 \cdot a}\right)^2\right] \qquad \text{hollow profile} \tag{5.4}$$

where $a = 0.63\,\mathrm{m}$ is the plasma radius and r is the (minor) radial coordinate—the profiles described by Eq. (5.3) and Eq. (5.4) correspond to the two seed profiles used in the simulations of the disruption in JET discharge #95135 described in Section 4.2.1.3. Both the prescribed post-disruption temperature and the amount of assimilated argon was the same as in Section 4.2.1.3: $T_f = 10\,\mathrm{eV}$ and $n_{\mathrm{Ar}} = 0.15 n_{\mathrm{Ar0}} = 1.2 \times 10^{18}\,\mathrm{m}^{-3}$.

Plasma current

Figure 5.1a shows total plasma currents, plus the runaway components I_{RE}, from the DREAM simulations with the different seed profiles given by Eq. (5.1)-(5.4), while Fig. 5.1b shows the normalized seed density profiles together with their respective scale factors A_{RE}. In Fig. 5.1a, we see that only the peaked runaway seed profile failed to reproduce the dip in the plasma current before the runaway plateau: the other three seed profiles gave almost identical current decays. This discrepancy in plasma current evolution between the different seed profiles is connected to the conducting wall.

When the characteristic wall time, used to define the wall resistance in DREAM as per Eq. (3.17), is $\tau_{\mathrm{wall}} = 5\,\mathrm{ms}$ as in the DREAM simulations with the four different seed profiles in Eq. (5.1)-(5.4), the wall acts as a sort of energy reservoir: electric fields can be induced in the wall and later diffuse into the plasma. This provides an energy boost to the plasma, which in turn enables the net increase in the plasma current we see for the uniform, power and hollow seed profiles in Fig. 5.1a. With the peaked seed profile, however, DREAM is unable to reproduce the local minimum in I_p. From the simulation results we thus conclude that with the peaked runaway density profile, there is no significant energy boost to the electrons from the wall, while with any of the three seed profiles described by Eq. (5.1), Eq. (5.2) or Eq. (5.4) (where the runaways in the seed are located closer to the wall), the wall has a discernible impact on the plasma current evolution.

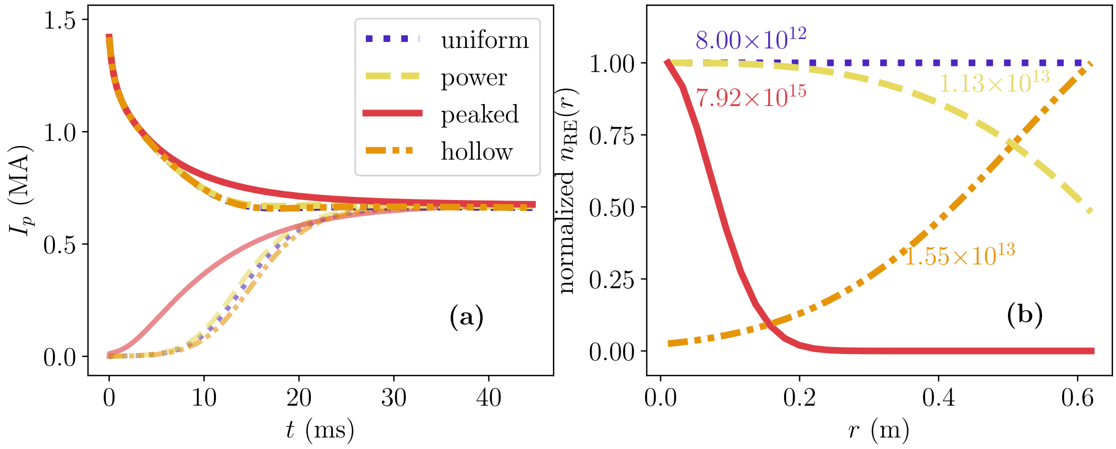

Figure 5.1: (a) Total plasma currents and the runaway current components from Dream current quench simulations with different seed profiles and **(b)** the runaway seed density profiles and seed scaling factors for these simulations.

All four seed profiles give very similar runaway plateaus; at $t = 44.6$ ms the number of runaways (the volume integrated runaway density profile) was almost identical no matter which seed profile had been used. However, when comparing the seed currents—the amount of current carried by the runaway electrons at $t = 0$ in the simulations—we find that with the peaked seed profile, $I_{\rm seed} \sim 13$ kA, while $I_{\rm seed} \sim 0.5$ kA with the uniform, power and hollow seed profiles. This reveals that with the peaked seed profile, a larger portion of the total plasma current was carried by the runaways at the beginning of the current quench, and that there was less avalanche multiplication during the current quench. This is supported by the dynamics of the runaway component $I_{\rm RE}$, shown in less opaque dashed red in Fig. 5.1a. Since the avalanche generation depends on the electric field, we again see that with the peaked seed profile, the energy stored in the conducting wall has a smaller impact on the current dynamics than with the other three seed profiles: flux diffusing from the wall enables higher electric fields to be sustained for longer in the plasma, resulting in more avalanche generation.

Synchrotron images

Since three of the four different runaway seed density profiles gave almost identical plasma current dynamics, I_p alone can not reveal which of the runaway seed profiles is best suited to model the disruption. Luckily, the synthetic synchrotron data from Soft is more sensitive to the radial distribution of runaways.

In Fig. 5.2 are both synthetic and experimental synchrotron images for $t = 44.6$ ms (top row) and $t = 374.6$ ms (bottom row). Comparing the synthetic synchrotron images in Fig. 5.2a-d with the experimental image in Fig. 5.2e, we gather that only the peaked seed profile (Fig. 5.2c), described by Eq. (5.3) gives, a synchrotron spot that is at all reminiscent of its experimental counterpart.

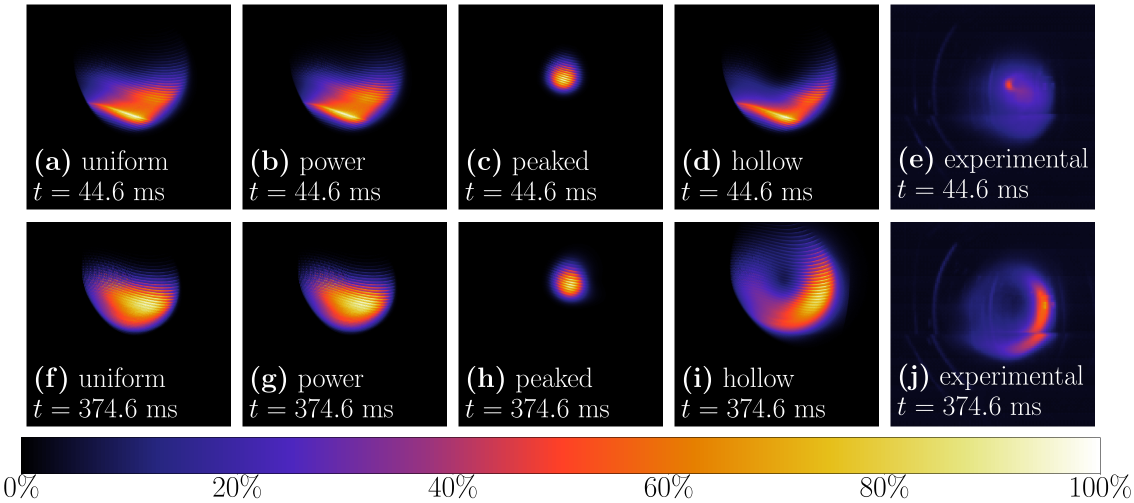

Figure 5.2: **(a)-(d)** and **(f)-(i)** show synthetic synchrotron images from SOFT, where different seed profiles were used in DREAM to obtain the runaway distribution functions. The corresponding experimental image is shown in **(e)** and **(j)**. Images in the top row are for $t = 44.6$ ms, while the bottom row shows images for $t = 374.6$ ms.

For $t = 374.6$ ms, we instead see that only the hollow runaway seed profile (Fig. 5.2i), described by Eq. (5.4), gives a synchrotron spot with a crescent shape similar to the experimental synchrotron spot in Fig. 5.2j. The synthetic synchrotron data thus reveals what the plasma current alone could not: out of the uniform, power, peaked and hollow runaway seed density profiles, only the two latter give synchrotron spots similar to the corresponding experimental image. If we assume a peaked seed density profile, SOFT gives a synchrotron spot similar to that in the experimental image captured at $t = 44.6$ ms (Fig. 5.2e), while the hollow runaway seed gives a synchrotron spot with a crescent shape similar to that in the experimental image captured at $t = 374.6$ ms (Fig. 5.2j).

5.2 Using simulated and model distribution functions as input to SOFT

A numerical runaway distribution function from DREAM is not necessary to generate synthetic synchrotron data: there are various model runaway distribution functions available in SOFT. For instance, the distribution function can be assumed to be mono-energetic:

$$f_{\mathrm{RE}}(\rho, p, \theta_p) = f(\theta_p) f(\rho) \delta(p - \tilde{p}), \tag{5.5}$$

where $\tilde{p}$ is some given value for the momentum. To see how well such a simplified model distribution function holds up against its numerical counterpart from DREAM, a SOFT synchrotron image simulation with the EFIT reconstructed magnetic field from $t = 374.6$ ms was performed with a mono-energetic model distribution function as in Eq. (5.5). Here, we let $\tilde{p}$ be the dominant particle from the SOFT synchrotron image simulation for $t = 374.6$ ms where we used a distribution function from the DREAM disruption simulation with the hollow seed profile (see Fig. 4.9h for the synthetic synchrotron image and Fig. 4.10h for the corresponding Green's function): $\tilde{p} = 27\ m_e c$. Assuming a mono-energetic expression for the distribution function can be motivated by the fact that the synchrotron radiation is expected to be dominated by the remnant seed population (which will be narrowly distributed in energy) [47], and that the synchrotron spot shape depends relatively weakly on the energy of the particles—the energy distribution does not significantly impact the spot shape.

We choose a pitch angle distribution $f(\theta_p)$ according to

$$f(\theta_p) = \exp\left[33\cos\theta_p\right], \tag{5.6}$$

which is the pitch component of a steady-state solution to the kinetic equation (i.e. with $\partial f/\partial t = 0$) where $E > E_c$ [52].

Next, we let the model distribution function in Eq. (5.5) have the same radial dependence as the hollow runaway seed density profile:

$$f(\rho) = \exp\left[-\left(\frac{\rho - 0.8\rho_{\max}}{0.4\rho_{\max}}\right)^2\right]. \tag{5.7}$$

Above, ρ is the normalized minor radial coordinate used in Soft: $\rho = r/a$ where a is the radial extension of the plasma obtained from the EFIT reconstructed magnetic field used to generate the synchrotron data, so that $\rho_{\max} = 1$ is the maximum value of ρ.

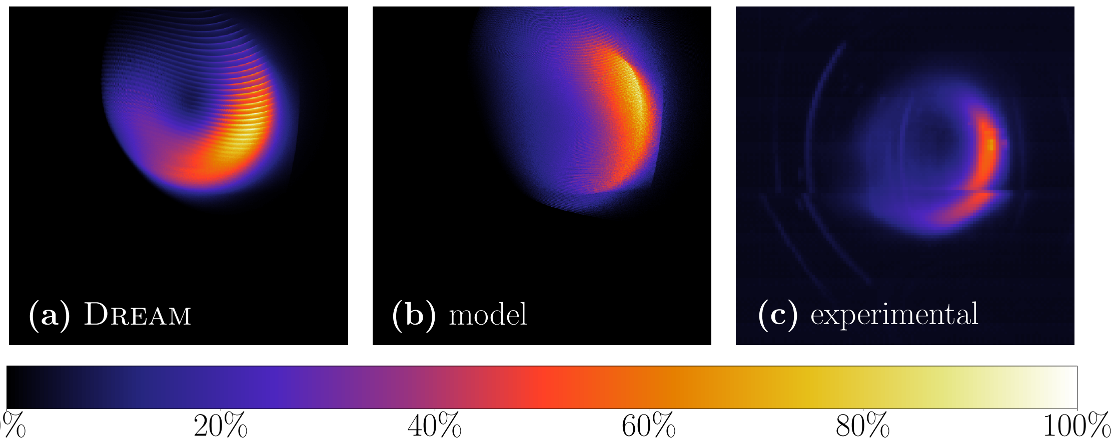

Figure 5.3: Synthetic synchrotron images from Soft together with the corresponding experimental image, for $t = 374.6$ ms. To generate **(a)**, a distribution function from Dream was used, while **(b)** was created using a mono-energetic model distribution function. In **(c)** is the experimental image.

In Fig. 5.3a is a synchrotron image from Soft created with a distribution function from the Dream disruption simulation where the hollow seed density profile was used, while Fig. 5.3b shows the synchrotron image generated with the model distribution function described by Eq. (5.5): the pitch angles where distributed according to Eq. (5.6) and the radial dependence was as in Eq. (5.7). Figure 5.3c shows the corresponding experimental image.

Figure 5.3 shows that both the distribution function from the Dream disruption simulation (Fig. 5.3a) and the model distribution function (Fig. 5.3b) resulted in crescent shaped synchrotron spots. With a Dream distribution function, Soft also gave a region seemingly void of synchrotron radiation in the middle of the spot, similar to what can be seen in the experimental image in Fig. 5.3c. This 'hole' is not present in the synthetic synchrotron spot shown in Fig. 5.3b.

The synthetic synchrotron images in Fig. 5.3 indicate that the model distribution function is capable of reproducing the qualitative features of the experimental synchrotron spot, but that the distribution function from Dream gives an even better agreement with the experimental data. This could be due to the fact that for the Dream distribution function, the dependencies on energy and pitch angle are not separable. The agreement between the experimental and the simulated images will also depend on how well the free parameters ($\tilde{p}$ and the constant in the exponent in Eq. (5.6) for the model distribution function, and parameters such as the amount of assimilated argon and the runaway seed density profile for Dream) can be fitted.

In Ref. [45], a model distribution function with uniform spatial energy and pitch angle distributions was used to generate a synthetic synchrotron image from JET discharge #95135. A hollow radial distribution of the runaways was assumed, similar to the hollow profile used in this thesis. As in Section 5.1, Ref. [45] found that a runaway population which was peaked around the magnetic axis was unable to reproduce a synchrotron spot similar to that seen in the later experimental camera images.

5.3 Simulation parameters and the plasma current

As we have previously established, the plasma current evolution in Dream depends on a variety of variables available for adjustment. Some of these parameter values can be obtained from experimental data, while some—such as the post-disruption temperature and amount of assimilated injected material—had to be fitted. In this thesis, we also made a number of assumptions when modeling the disruption in JET discharge #95135; we used $\tau_{\text{wall}} = 5\,\text{ms}$, we let the initial plasma current density be completely uniform (flat), and we assumed that Dreicer generation contributed most during the thermal quench, which is why this contribution was only accounted for via the prescribed runaway seed. In this section, we investigate how changing some of the fitted parameters and assumptions impacts the resulting plasma current from Dream: the amount of assimilated argon is treated in Section 5.3.1, the temperature in Section 5.3.2, the characteristic wall time in Section 5.3.3 and the Dreicer generation and initial plasma current density in section 5.3.4.

5.3.1 The amount of assimilated argon

Parameter scans performed for this thesis showed that for a given value of the post-disruption T_f, increasing the amount of assimilated argon gave shorter current quench times; more injected material means increased collisionality and as a result, higher resistivity. To illustrate the effect of increasing the amount of argon, four simulations where the post-disruption temperature was $T_f = 10\,\text{eV}$, but which each had different n_{Ar}, were performed. These simulations all used the hollow runaway seed density profile described by Eq. (5.4), but they each had different seed scaling factors A_{RE}.

Figure. 5.4a shows the total plasma currents, as well as the runway currents, from DREAM. Figure 5.4a shows that all four simulations gave the local minimum in the plasma current before the runaway plateau. Furthermore, an increased amount of assimilated argon gave shorter current quench times. With shorter current quench times, the electric field induced during the current quench will be stronger, yielding higher avalanche generation rates and thus a more rapid runaway population growth. The data in Fig. 5.4a supports this: the shortest current quench and fastest growing I_{RE} is achieved with $n_{\mathrm{Ar}} = 1.00 n_{\mathrm{Ar0}}$.

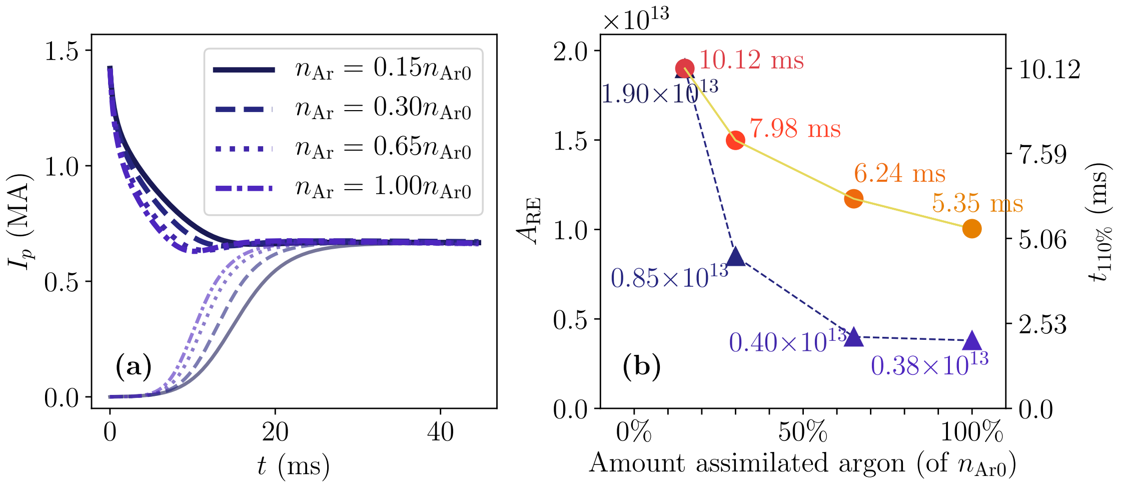

Figure 5.4: DREAM results from simulations with different amounts of assimilated argon. In **(a)** are the plasma currents and their respective runaway components while **(b)** shows the scaling factors A_{RE} (triangles) and $t_{110\%}$ (circles) as functions of the assimilated argon.

Figure 5.4b shows the runaway seed scaling factors A_{RE} and $t_{110\%}$—the time it takes for the plasma current to decay from the current spike to a value which is 10% above the runaway plateau—as a function of the fraction of the injected argon assumed to have assimilated into the plasma. Here, where we see that the required seed size appears to be exponentially decaying with the fraction of assimilated argon, and that $t_{110\%}$ also decreases as n_{Ar} increases.

The results in Fig. 5.4b reveal why the amount of assimilated argon was fitted to 15% of n_{Ar0} in the simulations in Section 4.3.1 where $T_f = 10\,\mathrm{eV}$; more argon would have resulted in a smaller $t_{110\%}$, and since the parameter t_{CQ} decreases as $t_{110\%}$ does so, both these $t_{110\%}$ and t_{CQ} would have been too small to match the experimental data with more assimilated argon. With 15% assimilated argon, the peaked seed profile gave $t_{110\%}$ matching the experimental value, while the same amount of argon in the disruption simulation with the hollow seed profile resulted in a thermal quench time t_{CQ} matching that from the experimental data.

More argon in the plasma means more target electrons for avalanche multiplication: if we increase the number of electrons susceptible to being knocked over the critical momentum p_c, we must decrease the number of runaway seed electrons capable of transferring that momentum if we want to achieve the same runaway plateau current as for lower amounts of argon. The higher avalanche generation rates (due to the shorter current quench times) also contribute to the need to decrease the size of the runaway seed if we add more argon.

5.3.2 Post-disruption temperature

We saw in Section 5.3.1 (Fig. 5.4) that increasing the amount of assimilated argon gave a faster current quench for a given temperature. To instead illustrate how the post-disruption temperature impacts the plasma current evolution, five simulations with different T_f and the same $n_{\mathrm{Ar}} = 0.15 n_{\mathrm{Ar0}}$ were performed. These simulations all used the hollow runaway seed density profile described by Eq. (5.4), but again the scaling factors A_{RE} differed. The resulting plasma currents, together with their respective runaway currents, are shown in Fig. 5.5a, while Fig. 5.5b shows A_{RE} and $t_{110\%}$ as functions of the temperature.

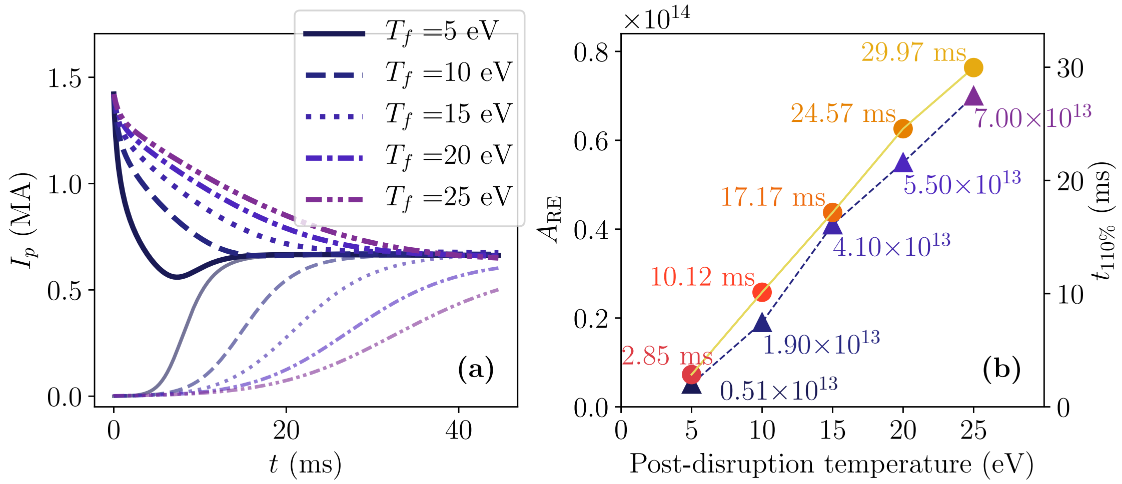

Figure 5.5: DREAM results from simulations with different post-disruption temperatures. In **(a)** are the total plasma currents and their respective runaway components, while **(b)** shows $t_{110\%}$ (circles)—the time where the plasma current is 10% above the plateau current—and the seed scaling factors A_{RE} (triangles) as functions of T_f.

In Fig. 5.5a we see that higher temperatures gave slower current quenches and monotonically decaying total plasma currents. Only $T_f = 5\,\mathrm{eV}$ and $T_f = 10\,\mathrm{eV}$ gave the local minimum after the current quench. With $T_f = 5\,\mathrm{eV}$ we also get a much larger dip than if $T_f = 10\,\mathrm{eV}$. Since plasma resistivity scales with the temperature as $T^{-3/2}$, a higher temperature gives lower resistivity. This in turn results in a slower current quench and a weaker induced electric field, leading to less avalanche multiplication and a slower growth of the runaway component of the plasma current. Since the induced electric field is weaker in a slower current quench, higher post-disruption temperatures will also result in less energy stored in the conducting wall. This means that the energy boost to the plasma from the wall will be smaller, and we do not obtain a net increase in plasma current after the current quench. In contrast, a lower T_f gives a more rapid current quench, yielding a larger induced electric field and as a result, a larger energy boost from the wall.

In Fig. 5.5b we see that the seed current required to obtain the correct plateau current increases almost linearly with the post-disruption temperature. Since a lower T_f gives a stronger induced electric field, we must decrease the runaway seed size if we decrease the post-disruption temperature in order to still obtain the desired plateau current.

5.3.3 The characteristic wall time

The results in Section 5.1 and Section 5.3.2 indicate that the conducting wall is closely connected to the dip in the total plasma current sometimes seen before the runaway plateau. To verify this, the plasma current from three simulations with different τ_{wall} were compared. These simulations all had $T_f = 10\,\text{eV}$, $n_{\text{Ar}} = 0.15 n_{\text{Ar0}}$ and used the hollow seed profile given by Eq. (5.4). The only difference between the simulations was τ_{wall} and the seed profile scaling factors:

$$A_{\text{RE}} = \begin{cases} 1.9 \times 10^{13} \implies I_{\text{seed}} \sim 0.52\,\text{kA}, & \tau_{\text{wall}} = 5\,\text{ms} \\ 2.1 \times 10^{13} \implies I_{\text{seed}} \sim 0.58\,\text{kA}, & \tau_{\text{wall}} = 10\,\text{ms} \\ 5.5 \times 10^{15} \implies I_{\text{seed}} \sim 151.21\,\text{kA}, & \tau_{\text{wall}} = \infty. \end{cases} \tag{5.8}$$

As show above, the magnitude of the runaway seed must be increased along with τ_{wall}, yielding higher seed currents. For a perfectly conducting wall (i.e. with $\tau_{\text{wall}} = \infty$), the seed current was one order of magnitude larger than when the disruption was modeled with $\tau_{\text{wall}} = 5\,\text{ms}$ and the peaked seed density profile in section 5.1.

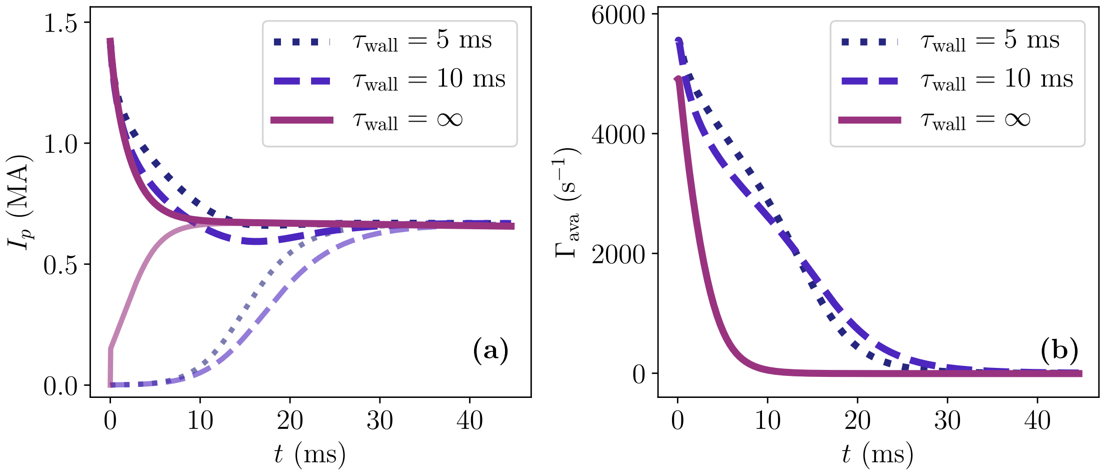

Figure 5.6: In **(a)** are the resulting plasma currents, plus the respective runaway components, from DREAM current simulations with the hollow runaway seed profile and different characteristic wall times, while **(b)** shows the avalanche multiplication factors from the three simulations.

The resulting plasma currents, and the respective runaway components, from the simulations with different wall times are shown in Fig. 5.6a. Here, we see that when the wall is assumed to be perfectly conducting, the current decays monotonically, and that I_{RE} is already large at the beginning of the simulation (note that the sharp transition from $I_{\mathrm{RE}} = 0$ at $t = 0$ for the simulation with $\tau_{\mathrm{wall}} = \infty$ is due to the large runaway seed prescribed). A perfectly conducting wall cannot act as an energy reservoir (since no electric fields can be induced in it), and therefore there will not be a net increase in the total plasma current if $\tau_{\mathrm{wall}} = \infty$.

In Fig. 5.6b, we see that with $\tau_{\mathrm{wall}} = \infty$, the avalanche multiplication factor (solid line) begins at a lower value and quickly goes to zero, while for $\tau_{\mathrm{wall}} \neq \infty$, the avalanche multiplication factor decreases much more slowly (the dashed and dotted lines)—the energy stored in the conducting wall enables avalanche generation to continue longer into the simulation.

In Fig. 5.6a we also see that $\tau_{\mathrm{wall}} = 10\,\mathrm{ms}$ gives a more pronounced dip in I_p than $\tau_{\mathrm{wall}} = 5\,\mathrm{ms}$. With a shorter τ_{wall}, the wall is slower to respond to changes in the plasma. This means that with $\tau_{\mathrm{wall}} = 5\,\mathrm{ms}$, more of the electric field induced during the current quench will have been 'consumed' by runaway generation before the wall reacts—this is corroborated by the fact that the runaway currents in Fig. 5.6a grow more rapidly when $\tau_{\mathrm{wall}} = 5\,\mathrm{ms}$ (dotted) than if $\tau_{\mathrm{wall}} = 10\,\mathrm{ms}$ (dashed). Since more of the energy has been used to create runaways, there is less energy left to store in the wall. The opposite is true for $\tau_{\mathrm{wall}} = 10\,\mathrm{ms}$: the wall responds faster, so the electric field induced during the current quench will both fill the energy reservoir the conducting wall poses as, and be used to create runaway electrons. Therefore, more energy will be stored in the wall, yielding a larger energy boost and thus a larger net increase in the total plasma current after the current quench.

5.3.4 Dreicer generation and the initial current density profile

In Chapter 4, we did not include Dreicer generation rates in the Dream simulations, since this type of runaway generation was expected to contribute most during the thermal quench, which we approximated to be instantaneous. Any Dreicer generated runaways were thus accounted for via the prescribed runaway seed density profile. Furthermore, we assumed a completely flat initial plasma current density profile. In the experiment, the plasma current density is likely *not* completely flat during the disruption, and from experimental data we know that before the disruption, the current density is peaked around the magnetic axis; the experimental pre-disruption current density profile is shown in Fig. 5.7. During the disruption, this profile is flattened to some extent, resulting in the current spike in the experimental data (Fig. 4.2a). Exactly how much the profile is flattened during the disruption is not clear—there are no post-thermal quench measurements of the current density available. Therefore, in order to determine the effect of the initial current density profile on the plasma current dynamics in Dream, we considered two extremes:

1. The current profile remains unchanged during the thermal quench.
2. The current profile is completely flattened to a uniform profile during the thermal quench.

In this section, we will compare results from simulations where we either assumed a flat current density profile, or used the experimental profile shown in Fig. 5.7. For each of the respective current density profiles, we also examined how the inclusion of Dreicer generation impacted the resulting plasma currents from Dream.

Experimental current density profile

To see how the experimental current density profile affected the disruption simulation results, two simulations with initial current density profiles as in Fig. 5.7 were performed in Dream. Both simulations used the hollow seed profile described by Eq. (5.4), but with different seed scaling factors.

The first simulation did *not* include Dreicer generation, and had $T_f = 10\,\mathrm{eV}$, $n_{\mathrm{Ar}} = 0.15 n_{\mathrm{Ar0}}$ and $A_{\mathrm{RE}} = 1.75 \times 10^{13}$, yielding a seed current of $I_{\mathrm{seed}} \sim 0.48\,\mathrm{kA}$. The second simulation *did* model Dreicer generation. With Dreicer generation, the seed scaling factor was $A_{\mathrm{RE}} = 6.27 \times 10^{12}$, and the temperature and amount of assimilated argon were fitted to $T_f = 25\,\mathrm{eV}$ and $n_{\mathrm{Ar}} = 0.57 n_{\mathrm{Ar0}}$, resulting in a seed current of $I_{\mathrm{seed}} \sim 0.17\,\mathrm{kA}$.

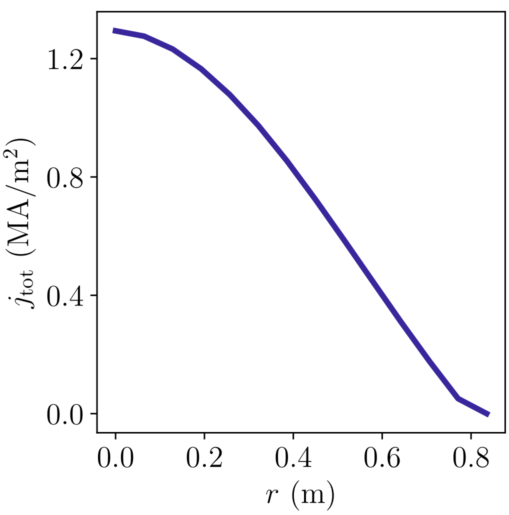

Figure 5.7: Experimental pre-disruption current density profile from JET discharge #95135. The magnetic axis is located at $r = 0$.

The total plasma currents, as well as the runaway components, from the two simulations are presented in Fig. 5.8a, while Fig. 5.8b shows the normalized runaway density profiles at $t = 44.6\,\mathrm{ms}$. Figure 5.8a shows that including Dreicer generation gave a slower growth of I_{RE} (dashed blue): the higher temperature required for this simulation resulted in a slower current quench, and a lower induced electric field. As a result, there was no net increase in the total plasma current after the current quench when Dreicer generation was included, since the energy boost from the wall was not large enough to yield this feature.

In Fig. 5.8b we see that with Dreicer generation, the runaway density has been redistributed at $t = 44.6\,\mathrm{ms}$ (dashed blue). This means that many more runaways have been generated close to the center of the plasma than at the plasma edge, resulting in a runaway electron density that is peaked around the magnetic axis. With the experimental current density profile, we get a plasma where more current is carried close to the magnetic axis, which is why the Dreicer generation will also contribute most here—Dreicer generation is strongest in the regions of the plasma where the plasma current decreases most, since that is where the electric field increases most.

In contrast, if no Dreicer generation was included, using the experimental pre-disruption current density profile still gave the local minimum in the plasma current (Fig. 5.8a, solid red), and resulted in a the runaway density profile which remained hollow (Fig. 5.8b, solid red).

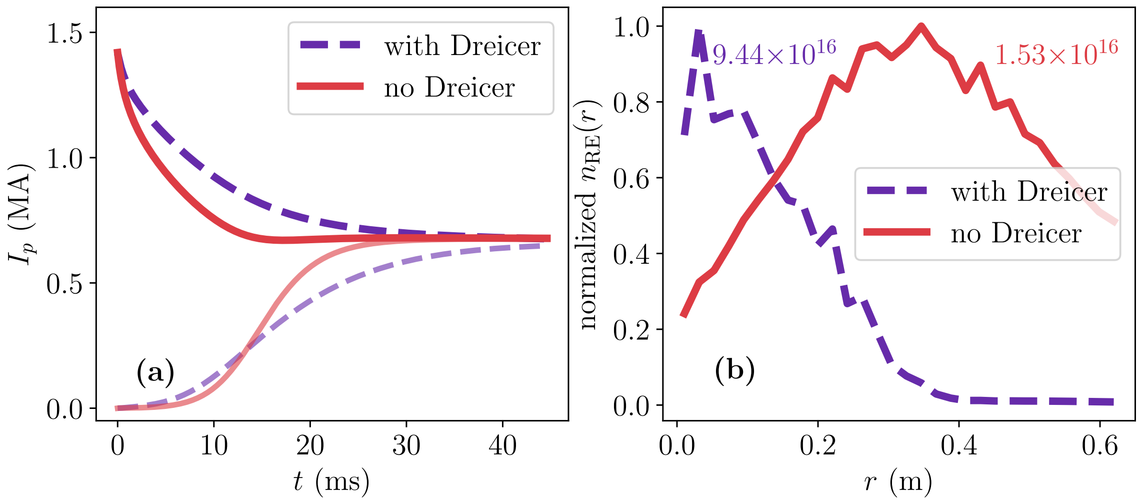

Figure 5.8: Data from DREAM simulations where the experimental current density profile was used. In **(a)** are the total plasma currents, plus the runaway components, while **(b)** shows the (normalized) runaway population density profiles at $t = 44.6\,\mathrm{ms}$ from the two simulations where the experimental plasma current density was used. In dashed blue is data from the simulation with Dreicer generation.

Uniform current density profile

To see how including Dreicer generation might impact the plasma current from DREAM under the assumption that the initial current density profile was flat, a simulation with a uniform initial current density distribution and including Dreicer generation was performed. This simulation used the hollow seed profile with a scaling factor $A_{\mathrm{RE}} = 3.26 \times 10^{12}$, yielding a seed current of $I_{\mathrm{seed}} \sim 0.11\,\mathrm{kA}$. The post-disruption temperature and amount of assimilated argon were fitted to $T_f = 12\,\mathrm{eV}$ and $n_{\mathrm{Ar}} = 0.9 n_{\mathrm{Ar}0}$.

The resulting total plasma current from the simulation with Dreicer generation can be seen in Fig. 5.9a (dashed orange) where it is shown together with I_p from a simulation without Dreicer generation (solid yellow). Figure 5.9a also shows the runaway currents I_{RE} for both simulations. In Fig. 5.9b are the normalized runaway electron densities at $t = 44.6\,\mathrm{ms}$ in the respective simulations.

In Fig. 5.9a we see that with the uniform current density profile, we were able to recreate the local minimum in I_p no matter if we included Dreicer generation or not, although the slightly higher T_f required if Dreicer generation was included gave a smaller net increase in plasma current after the current quench.

We see in Fig. 5.9b that if we include Dreicer generation, the runaway density profile is redistributed to a profile which is peaked around the magnetic axis (just as it was when the experimental current density profile was used, see Fig. 5.8b): the total plasma current will decay most in the center of the plasma since there are runaways which will carry some current at the plasma edge with the hollow seed profile, yielding stronger Dreicer generation closer to the magnetic axis.

From the results shown in Fig. 5.8 and Fig. 5.9 we conclude that no matter which initial current density profile is used, the inclusion of Dreicer generation results in a runaway density profile which is centered around the magnetic axis after the current quench. Such a profile could be consistent with the experimental synchrotron spot at $t = 44.6\,\mathrm{ms}$, shown in Fig. 4.9i. However, we saw in both Section 4.3.1 and Section 5.1 that runaway density profile which is peaked around the magnetic axis could not yield the synchrotron spot we see in the experimental synchrotron images shown in Fig. 4.9j-l; the runaway electrons would need to be redistributed into a hollow shape to reproduce the synchrotron spots seen in the later experimental camera images. Furthermore, if the experimental current density profile was used, the inclusion of Dreicer generation meant we had to increase the post-disruption temperature to $T_f = 25\,\mathrm{eV}$. This resulted in a slower current quench and lower induced electric field, which in turn lead to a monotonically decaying plasma current. In contrast, with the uniform initial current density profile we could reproduce the local minimum in I_p even if we included Dreicer generation since the temperature was lower: $T_f = 12\,\mathrm{eV}$.

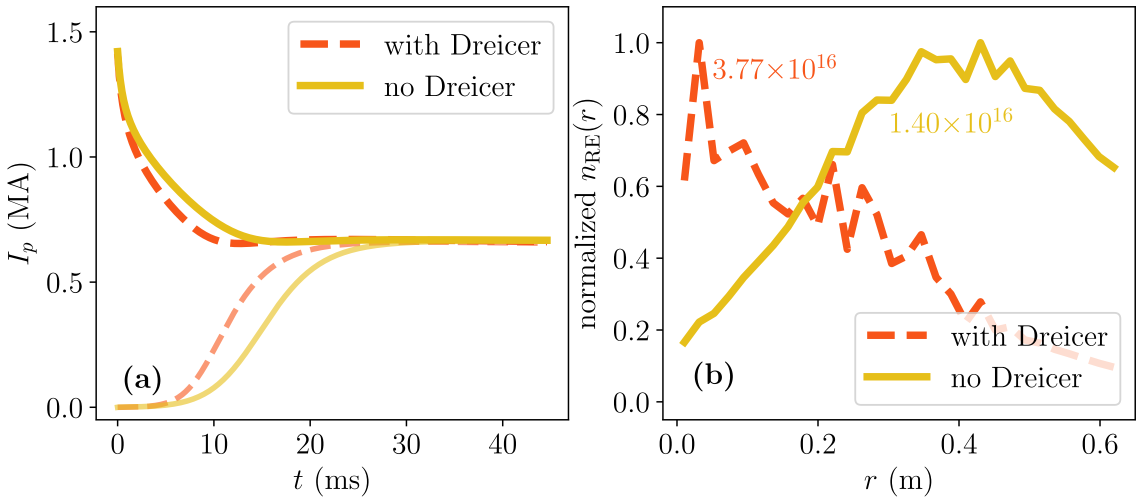

Figure 5.9: Data from DREAM simulations where a uniform initial current density profile was used. In **(a)** are the total plasma currents, and runaway components, from DREAM current quench simulations with (dashed orange) and without (solid yellow) Dreicer generation and **(b)** normalized runaway densities at $t = 44.6\,\mathrm{ms}$ in the simulations.

If we did not include Dreicer generation, both the experimental and the uniform current density profile gave a runaway distribution which remained hollow throughout the current quench. Both initial current density profiles also gave the local minimum in the total plasma current when we did not include Dreicer generation in the simulations.

5.4 Remaining issues and prospects

Since we in this thesis were mainly interested in what happened after the thermal quench, assuming $t_{\mathrm{TQ}} = 0$ and prescribing a runaway seed was an excellent approach. This approximate thermal quench model enabled efficient simulations while still reproducing the experimental plasma current dynamics quite well. Using a fluid model for the cold electron population further reduced the computational cost, and the results in this thesis indicate that this approximate electron model was valid when modeling a JET disruption. Furthermore, since the runaway seed density profile was a free parameter, the impact of the runaway density profile on the synthetic diagnostic signals could be examined.

Although we were able to reproduce the evolution of the total plasma current in JET discharge #95135 with Dream using the thermal quench model described in Section 4.2.1.1, the synthetic synchrotron data from Soft indicated that there is substantial radial transport of the runaway electrons taking place during the disruption. To model the disruption in an even more self-consistent manner in Dream, we would thus require knowledge about the transport coefficients so that the radial transport of the runaway electrons could be accounted for.

Using distribution functions from Dream as input to Soft provided additional information about the fit of the runaway seed density profile; without synthetic synchrotron data from Soft, it would be much more difficult to discern whether or not a certain radial distribution of the runaway population was an accurate representation of the runaways generated in the disruption.

In this thesis, we used numerical magnetic data from EFIT. Because of inherent difficulties in reconstructing magnetic fields in post-disruption plasmas, this data is not entirely accurate, and using some other magnetic fields (numerical or analytical) would impact the resulting synthetic synchrotron data from Soft. However, the numerical magnetic fields used in thesis were elongated, somewhat triangular and Shafranov shifted, why the EFIT magnetic fields were likely a more realistic representation of the magnetic fields in discharge #95135 than for instance an analytical circular magnetic field would be.

All in all, the simplified models used in this thesis proved successful and efficient, although the simulations revealed that in order to better capture the disruption dynamics, radial transport of the runaway population must be modeled. This promises a bright future for Dream as a disruption modeling tool, for present and planned machines.

6
Conclusion

We were able to reproduce the current quench time and runaway plateau from the experimental data from JET discharge #95135 using an approximate electron model—where only the runaway electrons were modeled kinetically—and a thermal quench model where we assumed $t_{\mathrm{TQ}} = 0$ and prescribed a runaway seed density profile. This approach gave computationally efficient simulations: the simulations performed for this thesis took about one day to run on a desktop computer, while similar simulations performed with Go+Code for Ref. [47] took about a week to run on a small cluster.

Depending on which runaway seed profile was prescribed, the approximate thermal quench model was also successful in reproducing the dip seen in the plasma current before the experimental runaway plateau. To obtain this feature, we found that we must account for the finite wall resistivity, and that the ohmic component of the plasma current must decay fast enough. For JET discharge #95135, this required a post-disruption temperature such that $T_f \leq 12\,\mathrm{eV}$.

When examining the effect of the initial current density profile on the resulting data from Dream, we found that as long as Dreicer generation was not included in the simulation, both the pre-disruption experimental initial current density profile (which was peaked around the magnetic axis) and a uniform initial current density profile were able to reproduce the desired plasma current dynamics and preserve the hollow shape of the runaway density profile throughout the simulation. If Dreicer generation was included, the runaway population was instead redistributed into a density profile which was peaked around the magnetic axis.

Results from Soft showed that none of the runaway seed profiles used in this thesis were able to, on their own, reproduce all experimental synchrotron images; the peaked seed profile resulted in a synchrotron spot with similar appearance to the synchrotron spot seen in the earliest of the experimental synchrotron images considered in this thesis, while the hollow seed profile gave a synchrotron spot with a crescent shape similar to that in experimental images captured later in the discharge. This indicates that radial transport of the runaways plays an important role during the current quench and runaways plateau: the density profile of the runaway population begins as a narrow beam centered around the magnetic axis and gets redistributed into a profile with its maximum close to the plasma edge as the disruption progresses.

The synthetic MSE diagnostic data showed that there was no synchrotron light present on the outer channels of the MSE diagnostic in JET. When comparing synthetic and experimental intensity data I, this MSE signal supported the conjecture that there is a transition from a peaked runaway density profile to a hollow runaway density profile. Similar to the experimental data, the synthetic synchrotron radiation was mainly polarized in the horizontal direction. When considering the fraction of linearly polarized light f_{pol}, the agreement between simulated and experimental MSE diagnostic data was found to be poor; this might be due to polarized light pollution from unknown background sources in the measurements.

Bibliography

[1] A. D. Barnosky, N. Matzke, S. Tomiya, G. O. U. Wogan, B. Swartz, T. B. Quental, C. Marshall, J. L. McGuire, E. L. Lindsey, K. C. Maguire, B. Mersey, and E. A. Ferrer. Has the Earth's sixth mass extinction already arrived? *Nature*, 471, 2011. doi:10.1038/nature09678.

[2] G. Ceballos, P. R. Ehrlich, A. D. Barnosky, A. García, R. M. Pringle, and T. M. Palmer. Accelerated modern human–induced species losses: Entering the sixth mass extinction. *Science Advances*, 1(5), 2015. doi:10.1126/sciadv.1400253.

[3] M. R. Allen, O. P. Dube, W. Solecki, F. Aragón-Durand, W. Cramer, S. Humphreys, M. Kainuma, J. Kala, N. Mahowald, Y. Mulugetta, R. Perez, M. Wairiu, and K. Zickfeld. Framing and context. In V. Masson-Delmotte, P. Zhai, H.-O. Pörtner, D. Roberts, J. Skea, P. R. Shukla, A. Pirani, W. Moufouma-Okia, C. Péan, R. Pidcock, S. Connors, J. B. R. Matthews, Y. Chen, X. Zhou, M. I. Gomis, E. Lonnoy, T. Maycock, M. Tignor, and T. Waterfield, editors, *Global Warming of* 1.5 °C*. An IPCC Special Report on the impacts of global warming* 1.5 °C *above pre-industrial levels and related global greenhouse gas emission pathways, in the context of strengthening the global response to the threat of climate change, sustainable development, and efforts to eradicate poverty*, chapter 1. 2018.

[4] P. Shabecoff. Global Warming Has Begun, Expert Tells Senate. *The New York Times*, 1988. `https://www.nytimes.com/1988/06/24/us/global-warming-has-begun-expert-tells-senate.html`. Accessed: 2021-02-24.

[5] J. Hansen, I. Fung, A. Lacis, D. Rind, S. Lebedeff, R. Ruedy, G. Russell, and P. Stone. Global climate changes as forecast by Goddard Institute for Space Studies three-dimensional model. *Journal of Geophysical Research*, 93, 1988. doi:10.1029/JD093iD08p09341.

[6] Energimyndigheten. Ökning av förnybar elproduktion under 2020. `https://www.energimyndigheten.se/nyhetsarkiv/2021/okning-av-fornybar-elproduktion-under-2020`. Accessed: 2021-04-09.

[7] IRENA (2020). Renewable Power Generation Costs in 2019, . International Renewable Energy Agency, Abu Dhabi. `https://www.irena.org/-/media/Files/IRENA/Agency/Publication/2020/Jun/IRENA_Power_Generation_Costs_2019.pdf`. Accessed: 2021-05-25.

[8] IEA (2020). SDG7: Data and Projections, . IEA, Paris. `https://www.iea.org/reports/sdg7-data-and-projections`. Accessed: 2021-02-26.

[9] M. N. Rosenbluth and S. V. Putvinski. Theory for avalanche of runaway electrons in tokamaks. *Nuclear Fusion*, 37, 1997. doi:10.1088/0029-5515/37/10/I03.

[10] M. Hoppe, O. Embreus, and T. Fülöp. Dream: a fluid-kinetic framework for tokamak disruption runaway electron simulations. *Submitted to Comp. Phys. Comm.*, 2021. `https://arxiv.org/abs/2103.16457`.

[11] M. Hoppe, O. Embreus, R. A. Tinguely, R. S. Granetz, A. Stahl, and T. Fülöp. Soft: a synthetic synchrotron diagnostic for runaway electrons. *Nuclear Fusion*, 58, 2018. doi:10.1088/1741-4326/aa9abb. URL `https://arxiv.org/abs/1709.00674`.

[12] F. F. Chen. *Introduction to Plasma Physics and Controlled Fusion*. Springer International Publishing, 3 edition, 2018.

[13] N. J. Peacock, D. C. Robinson, M. J. Forrest, P. D. Wilcock, and V. V. Sannikov. Measurement of the Electron Temperature by Thomson Scattering in Tokamak T3. *Nature*, 244, 1969. doi:10.1038/224488a0.

[14] JET's salient features. `https://www.euro-fusion.org/devices/jet/jets-salient-features/`. Accessed: 2021-05-28.

[15] The ITER tokamak, . `https://www.iter.org/mach`. Accessed: 2021-04-09.

[16] What is ITER?, . `https://www.iter.org/proj/inafewlines`. Accessed: 2021-04-09.

[17] Commonwealth Fusion Systems. `https://cfs.energy/`. Accessed: 2021-05-22.

[18] A. J. Creely, M. J. Greenwald, S. B. Ballinger, D. Brunner, J. Canik, J. Doody, T. Fülöp, D. T. Garnier, R. Granetz, T. K. Gray, C. Holland, N. T. Howard, J. W. Hughes, J. H. Irby, V. A. Izzo, G. J. Kramer, A. Q. Kuang, B. LaBombard, Y. Lin, B. Lipschultz, N. C. Logan, J. D. Lore, E. S. Marmar, K. Montes, R. T. Mumgaard, C. Paz-Soldan, C. Rea, M. L. Reinke, P. Rodriguez-Fernandez,

K. Särkimäki, F. Sciortino, S. D. Scott, A. Snicker, P. B. Snyder, B. N. Sorbom, R. Sweeney, R. A. Tinguely, E. A. Tolman, M. Umansky, O. Vallhagen, J. Varje, D. G. Whyte, J. C. Wright, S. J. Wukitch, J. Zhu, and the SPARC Team. Overview of the SPARC tokamak. *Journal of Plasma Physics*, 86, 2020. doi:10.1017/S0022377820001257.

[19] P. Helander and D. J. Sigmar. *Collisional Transport in Magnetized Plasmas*. Cambridge University Press, 2002.

[20] J. W. Connor and R. J. Hastie. Relativistic limitations on runaway electrons. *Nuclear Fusion*, 15(3), 1975. doi:10.1088/0029-5515/15/3/007.

[21] S. Sridhar, C. Reux, P. Beyer, M. Lehnen, I. Coffey, R. Guirlet, and N. Fedorczak and. Characterization of cold background plasma during the runaway electron beam mitigation experiments in the JET tokamak. *Nuclear Fusion*, 60 (9):096010, 2020. doi:10.1088/1741-4326/ab9dd0.

[22] H. Dreicer. Electron and Ion Runaway in a Fully Ionized Gas. I. *Physical Review*, 115:238–249, 1959. doi:10.1103/PhysRev.115.238.

[23] O. Embréus, A. Stahl, and T. Fülöp. On the relativistic large-angle electron collision operator for runaway avalanches in plasmas. *Journal of Plasma Physics*, 84, 2018. doi:10.1017/S002237781700099X. URL `https://arxiv.org/abs/1708.08779`.

[24] The ITER tokamak: magnets, . `https://www.iter.org/mach/Magnets`. Accessed: 2021-04-27.

[25] H. Smith and E. Verwichte. Hot tail runaway electron generation in tokamak disruptions. *Physics of Plasmas*, 15:072502–072502, 2008. doi:10.1063/1.2949692.

[26] W. D. Jackson. *Classical Electrodynamics*. John Wiley & Sons, Inc., 3 edition, 1999.

[27] V. L. Ginzburg and S. I. Syrovatskii. Developments in the Theory of Synchrotron Radiation and its Reabsorption. *Annual Review of Astronomy and Astrophysics*, 7, 1969. doi:10.1146/annurev.aa.07.090169.002111.

[28] K. C. Westfold. The Polarization of Synchrotron Radiation. *Astrophysical Journal*, 130, 1959. doi:10.1086/146713.

[29] N. C. Hawkes, K. Blackler, B. Viaccoz, C. H. Wilson, J. B. Migozzi, and B. C. Stratton. Design of the Joint European Torus motional stark effect diagnostic. *Review of Scientific Instruments*, 70(1):894–897, 1999. doi:10.1063/1.1149415.

[30] R. A. Tinguely, M. Hoppe, R. S. Granetz, R. T. Mumgaard, and S. Scott. Experimental and synthetic measurements of polarized synchrotron emission from runaway electrons in Alcator C-Mod. *Nuclear Fusion*, 59, 2019. doi:10.1088/1741-4326/ab2d1d. URL `http://arxiv.org/abs/1906.11304`.

[31] M. Lehnen, K. Aleynikova, P.B. Aleynikov, D. J. Campbell, P. Drewelow, N. W. Eidietis, Yu. Gasparyan, R. S. Granetz, Y. Gribov, N. Hartmann, E. M. Hollmann, V. A. Izzo, S. Jachmich, S.-H. Kim, M. Kočan, H. R. Koslowski, D. Kovalenko, U. Kruezi, A. Loarte, S. Maruyama, G. F. Matthews, P. B. Parks, G. Pautasso, R. A. Pitts, C. Reux, V. Riccardo, R. Roccella, J. A. Snipes, A. J. Thornton, and P. C. de Vries. Disruptions in ITER and strategies for their control and mitigation. *Journal of Nuclear Materials*, 463:39–48, 2015. doi:10.1016/j.jnucmat.2014.10.075.

[32] L. Hesslow, O. Embréus, O. Vallhagen, and T. Fülöp. Influence of massive material injection on avalanche runaway generation during tokamak disruptions. *Nuclear Fusion*, 59, 2019. doi:10.1088/1741-4326/ab26c2. URL `http://arxiv.org/abs/1904.00602`.

[33] O. Vallhagen, O. Embreus, I. Pusztai, L. Hesslow, and T. Fülöp. Runaway dynamics in the DT phase of ITER operations in the presence of massive material injection. *Journal of Plasma Physics*, 86, 2020. doi:10.1017/S0022377820000859. URL `https://arxiv.org/abs/2004.12861`.

[34] G. Papp, T. Fülöp, T. Fehér, P. C. de Vries, V. Riccardo, C. Reux, M. Lehnen, V. Kiptily, V. V. Plyusnin, B. Alper, and JET EFDA contributors. The effect of ITER-like wall on runaway electron generation in JET. *Nuclear Fusion*, 53, 2013. doi:10.1088/0029-5515/53/12/123017.

[35] H. Smith, P. Helander, L.-G. Eriksson, D. Anderson, M. Lisak, and F. Andersson. Runaway electrons and the evolution of the plasma current in tokamak disruptions. *Physics of Plasmas*, 13, 2006. doi:10.1063/1.2358110.

[36] M. Landreman, A. Stahl, and T. Fülöp. Numerical calculation of the runaway electron distribution function and associated synchrotron emission. *Computer Physics Communications*, 185, 2014. doi:10.1016/j.cpc.2013.12.004. URL `http://arxiv.org/abs/1305.3518`.

[37] A. Stahl, O. Embreus, G. Papp, M. Landreman, and T. Fülöp. Kinetic

modelling of runaway electrons in dynamic scenarios. *Nuclear Fusion*, 56, 2016. doi:10.1088/0029-5515/56/11/112009. URL `http://arxiv.org/abs/1601.00898`.

[38] A. Stahl, M. Landreman, G. Papp, E. Hollmann, and T. Fülöp. Synchrotron radiation from a runaway electron distribution in tokamaks. *Physics of Plasmas*, 20, 2013. doi:10.1063/1.4821823.

[39] B. J. Braams and K. F. F. Charles. Conductivity of a relativistic plasma. *Physics of Fluids B: Plasma Physics*, 1(7):1355–1368, 1989. doi:10.1063/1.858966.

[40] H. P. Summers. The ADAS User Manual, version 2.6, 2004. `https://www.adas.ac.uk/manual.php`.

[41] M. Hoppe. Soft v2 documentation. `https://soft2.readthedocs.io/en/latest/intro.html`.

[42] I. M. Pankratov. Analysis of the Synchrotron Radiation Emitted by Runaway Elelctrons. *Plasma Physics Report*, 22, 1996.

[43] R.J. Zhou, I.M. Pankratov, L.Q. Hu, M. Xu, and J.H. Yang. Synchrotron radiation spectra and synchrotron radiation spot shape of runaway electrons in Experimental Advanced Superconducting Tokamak. *Physics of Plasmas*, 21 (6):063302, 2014. doi:10.1063/1.4881469.

[44] M. Hoppe, G. Papp, T. Wikjamp, A. Perek, J. Decker, B. Duval, O. Embreus, T. Fülöp, U. A. Sheikh, the TCV Team, and the EUROfusion MST1 team. Runaway electron synchrotron radiation in a vertically translated plasma. *Nuclear Fusion*, 60, 2020. doi:10.1088/1741-4326/aba371. URL `https://arxiv.org/abs/2003.10512`.

[45] C. Reux, C. Paz-Soldan, P. Aleynikov, V. Bandaru, O. Ficker, S. Silburn, M. Hoelzl, S. Jachmich, N. Eidietis, M. Lehnen, S. Sridhar, and JET contributors. Demonstration of Safe Termination of Megaampere Relativistic Electron Beams in Tokamaks. *Physical Review Letters*, 126:175001, 2021. doi:10.1103/PhysRevLett.126.175001.

[46] D. P. O'Brien, L. L. Lao, E. R. Solano, M. Garribba, T. S. Taylor, J. G. Cordey, and J. J. Ellis. Equilibrium analysis of iron core tokamaks using a full domain method. *Nuclear Fusion*, 32(8):1351–1360, 1992. doi:10.1088/0029-5515/32/8/i05.

[47] M. Hoppe, L. Hesslow, O. Embreus, L. Unnerfelt, G. Papp, I. Pusztai, T. Fülöp, O. Lexell, T. Lunt, E. Macusova, P. J. McCarthy, G. Pautasso, G. I. Pokol, G. Por, P. Svensson, the ASDEX Upgrade team, and the EUROfusion MST1 team. Spatiotemporal analysis of the runaway distribution function from synchrotron images in an ASDEX Upgrade disruption. *Journal of Plasma Physics*, 87, 2021. doi:10.1017/S002237782000152X. URL `https://arxiv.org/abs/2005.14593`.

[48] K. Insulander Björk, O. Vallhagen, G. Papp, C. Reux, O. Embreus, E. Rachlew, T. Fülöp, the ASDEX Upgrade team, JET contributors, and the EUROfusion MST1 team. Modelling of runaway electron dynamics during argon-induced disruptions in ASDEX Upgrade and JET. *Plasma Physics and Controlled Fusion*, 2021. URL `http://arxiv.org/abs/2101.02575`.

[49] M. Hoppe, O. Embréus, C. Paz-Soldan, R. A. Moyer, and T. Fülöp. Interpretation of runaway electron synchrotron and bremsstrahlung images. *Nuclear Fusion*, 58, 2018. doi:10.1088/1741-4326/aaae15.

[50] H. Strauss, E. Joffrin V., Riccardo, J. Breslau, and R. Paccagnella. Comparison of JET AVDE disruption data with M3D simulations and implications for ITER. *Physics of Plasmas*, 24(10):102512, 2017. doi:https://doi.org/10.1063/1.5004692.

[51] M. M. Hoppe, R.A. Tinguely, B. Brandström, O. Embreus, N.C. Hawkes, E. Rachlew, T. Fülöp, and JET contributors. Polarized synchrotron radiation as a tool for studying runaway electrons. In *28th IAEA Fusion Energy Conference*, number TH/P1-623, 2021.

[52] B. N. Breizman, P. Aleynikov, E. M. Hollmann, and M. Lehnen. Physics of runaway electrons in tokamaks. *Nuclear Fusion*, 59(8):083001, 2019. doi:10.1088/1741-4326/ab1822.

A
Initialization simulations

Before modeling a disruption in DREAM, a so called *initialization simulation* had to be performed. Such simulations were not intended to model any part of the disruption, but were merely a way of ensuring that the current quench started from the correct plasma current value.

By prescribing a constant temperature and electric field, a sort of "steady state" plasma—in the sense that no plasma parameters or quantities were evolving in time—was modeled; the current quench simulations were then initiated from output at the last timestep of the initialization simulation.

For the thermal quench model used in this thesis (as in 4.2.1.1), the temperature was prescribed to be uniformly the post-thermal quench temperature T_f for the total duration of all simulations. This included the initialization simulations, but note that the pre-disruption temperature might as well have been used for these simulations. Since the temperature was T_f from the start of the disruption simulation, and since it is the electric field induced from the current quench which will be of importance in the disruption simulation, letting $T = T_f$ for the initialization simulation is fine.

The initial electric field, E_{init}, was prescribed to be constant in time and was such that the desired plasma current was obtained at the end of the simulation. For the purposes of this thesis, this meant that the plasma current at the final timestep of the initialization simulation, I_p^{final}, should be such that $I_p^{\text{final}} = 1.0 I_{\text{spike}}$.

Assuming that E_{init} was uniform throughout the plasma resulted in a uniform (flat) initial plasma current density profile $j(r)$. Before a disruption, the current density is typically peaked around the magnetic axis, but this profile is flattened during the disruption, giving rise to the characteristic current spike seen before the current quench. The impact of the current density profile on the plasma current evolution in DREAM is discussed further in section 5.3.4.

Finding the E_{init} that would give $I_p^{\text{final}} = 1.0 I_{\text{spike}}$ was done by performing a (fluid) initialization simulation using some arbitrary (but reasonable) electric field strength. The final plasma current I_p^{final} of that simulation was then used to re-scale the electric field if needed:

$$E'_{\text{init}} = \left(\frac{I_{\text{spike}}}{I_p^{\text{final}}} \right) \cdot E_{\text{init}}. \tag{A.1}$$

An initialization simulation with the new electric field E'_{init} would then yield the desired final plasma current value.

For the initialization simulations, the wall was assumed to be perfectly conducting (so that $E_{\text{wall}} = 0$). Furthermore, the injected material was added, but was prescribed to be neutral for the duration of the simulation.

B

Simulation scripts

B.1 DREAM

Here, the Python scripts used in each of the respective simulation stages in DREAM described in section 4.2.1 are presented. In the scripts presented below, the hollow seed profile was used—for simulations with the peaked seed profile, $n_{\mathrm{RE}}(r)$ was instead defined as `n_re = Are*(np.exp(-(r/0.1)**2))`, where `r` was an array with radial coordinates, and `Are` the seed scaling factor.

B.1.1 Initialization simulation

```
import numpy as np
import sys
sys.path.append('/path/to/DREAM/py')

import DREAM
from DREAM.DREAMSettings import DREAMSettings
import DREAM.Settings.Equations.DistributionFunction as DistFunc
import DREAM.Settings.Equations.IonSpecies as Ions
import DREAM.Settings.Equations.RunawayElectrons as Runaways
import DREAM.Settings.Solver as Solver
import DREAM.Settings.CollisionHandler as Collisions
import DREAM.Settings.Equations.ElectricField as Efield
import DREAM.Settings.Equations.ColdElectronTemperature as T_cold
import DREAM.Settings.Equations.HotElectronDistribution as FHot
from DREAM.Settings.Equations.ElectricField import ElectricField
from DREAM.Settings.Equations.ColdElectronTemperature import ↩
    ColdElectronTemperature
import DREAM.Settings.TimeStepper as TimeStepper
import DREAM.Settings.XiGrid as XiGrid


##############
# PARAMETERS #
##############

# ---- Machine/experimental data ----
R = 2.643                                  # (m) Magnetic axis
B0 = 3.0                                   # (T) Toroidal B-field on magnetic ↩
    axis
data = sio.loadmat('ne_data_JET95135.mat')  # Load experimental electron density
dNe = data['dNe']
ne_profile = dNe[:,2]
nAr0 = 7.9862e18                           # (m^-3) Injected argon density


# ---- Radial grid ----
nr = 30                                    # Number of radial grid points
a = 0.63                                   # (m) Plasma minor radius
```

```
wallRadius = 0.73                            # (cm) Machine (wall) minor radius
r = np.linspace(0,a,nr)                      # (m) Radial coordinates
r_exp = dNe[:,0]- dNe[0,0]                   # (m) Experimental radial coordinates


# ---- Fitted parameters ----
T_f = 10                                     # (eV) Post-disruption temperature
nAr = 0.15*nAr0                              # (m^-3) Amount of assimilated argon
E_init = 20.8104                             # (V/m) Initial electric field


# ---- Time resolution ----
tMax = 10e-3                                 # (s) Duration of simulation
nt = 100                                     # Number of time steps


###############################
# Create DREAMSettings object #
###############################

ds=DREAMSettings()


# Set collision type
ds.collisions.collfreq_type = Collisions.COLLFREQ_TYPE_PARTIALLY_SCREENED


# Set electric field
ds.eqsys.E_field.setPrescribedData(E_init,radius=r)


# Set effective critical electric field (Eceff) mode
ds.eqsys.n_re.setEceff(Runaways.COLLQTY_ECEFF_MODE_FULL)


# Set temperature
ds.eqsys.T_cold.setPrescribedData(T_f, radius=r)


# Set ions
ds.eqsys.n_i.addIon(name='D2', Z=1, T=T_f, iontype=Ions.↩
    IONS_DYNAMIC_FULLY_IONIZED, n=ne_profile, r=r_exp)
ds.eqsys.n_i.addIon(name='Ar', Z=18, iontype=Ions.IONS_PRESCRIBED_NEUTRAL, n=nAr)


# Hot-tail grid settings
ds.hottailgrid.setEnabled(False)


# Runaway grid settings
ds.runawaygrid.setEnabled(False)


# Set up radial grid
ds.radialgrid.setB0(B0)
ds.radialgrid.setNr(nr)
ds.radialgrid.setMinorRadius(a)
ds.radialgrid.setWallRadius(wallRadius)


# Set solver type
ds.solver.setType(Solver.NONLINEAR)


# Save fluid quantities to output
ds.other.include('fluid')


# Set time stepper
ds.timestep.setTmax(tMax)
```

```
ds.timestep.setNt(nt)


# Set file name of output file
ds.output.setFilename(init_outname)


# Save settings to HDF5 file
ds.save(init_settingsname)
```

B.1.2 Current quench simulation

```
import numpy as np
import sys
sys.path.append('/path/to/DREAM/py')

import DREAM
from DREAM.DREAMSettings import DREAMSettings
import DREAM.Settings.Equations.DistributionFunction as DistFunc
import DREAM.Settings.Equations.IonSpecies as Ions
import DREAM.Settings.Equations.RunawayElectrons as Runaways
import DREAM.Settings.Solver as Solver
import DREAM.Settings.CollisionHandler as Collisions
import DREAM.Settings.Equations.ElectricField as Efield
import DREAM.Settings.Equations.ColdElectronTemperature as T_cold
import DREAM.Settings.Equations.HotElectronDistribution as FHot
from DREAM.Settings.Equations.ElectricField import ElectricField
from DREAM.Settings.Equations.ColdElectronTemperature import ↩
    ColdElectronTemperature
import DREAM.Settings.TimeStepper as TimeStepper
import DREAM.Settings.XiGrid as XiGrid


##############
# PARAMETERS #
##############

# ---- Machine/experimental data ----
R = 2.643                    # (m) Magnetic axis
B0 = 3.0                     # (T) Toroidal B-field on magnetic axis
nAr0 = 7.9862e18             # (m^-3) Injected argon density
walltime = 5e-3              # (s) Characteristic wall time


# ---- Radial grid ----
nr = 30                      # Number of radial grid points
a = 0.63                     # (m) Plasma minor radius
wallRadius = 0.73            # (m) Machine (wall) minor radius
r = np.linspace(0,a,nr)      # (m) Radial coordinates


# ---- Fitted parameters ----
# Runaway seed profile
Are = 1.9e13                 # Scaling factor
n_re = [Are*np.exp(-((rs-0.8)/0.4)**2) for rs in r]

T_f = 10                     # (eV) Post-disruption temperature
nAr = 0.15*nAr0              # (m^-3) Amount of assimilated argon


# ---- Time resolution ----
tMax = 44.6e-3               # (s) Duration of simulation
nt = 2000                    # Number of time steps


# ---- Runaway grid resolution parameters ----
```

```
pMax_re = 160               # (m_e*c) Maximum momentum
np_re   = 160               # Number of p-grid points
Nxi_re  = 120               # Number of pitch grid points


###############################
# Create DREAMSettings object #
###############################

# Copy DREAMSettings from initialization simulation
ds2 = DREAMSettings('/path/to/init_settings')


# Get data from last timestep of initialization simulation
ds2.fromOutput('/path/to/init_output', ignore = ['n_i','n_re'])


# Change to self-consistent E-field
ds2.eqsys.E_field.setType(Efield.TYPE_SELFCONSISTENT)
ds2.eqsys.E_field.setBoundaryCondition(bctype = Efield.BC_TYPE_SELFCONSISTENT, ↩
    inverse_wall_time = 1/walltime, R0=R)


# Get ions, set to self-consistently modelled
ds2.eqsys.n_i.getIon('Ar').initialize_dynamic_neutral(interpr=ds2.eqsys.n_i.↩
    getIon('Ar').r, n=nAr)


# Set time stepper
ds2.timestep.setTmax(tMax)
ds2.timestep.setNt(nt)


# Set initial runaway density profile
ds2.eqsys.n_re.setInitialProfile(density=n_re,radius=r)


# Runaway generation
ds2.eqsys.n_re.setAvalanche(Runaways.AVALANCHE_MODE_FLUID)
ds2.eqsys.n_re.setDreicer(Runaways.DREICER_RATE_DISABLED)


# Hot-tail grid settings
ds2.hottailgrid.setEnabled(False)


# Runaway grid
ds2.solver.tolerance.set('j_re', abstol=1)
ds2.runawaygrid.setEnabled(True)

# Runaway grid resolution parameters
ds2.runawaygrid.setNxi(nxi_re)
ds2.runawaygrid.setNp(np_re)
ds2.runawaygrid.setPmax(pMax_re)
ds2.runawaygrid.setBiuniformGrid(thetasep =0.4,nthetasep_frac=0.5)

# Initiate f_RE
f = np.zeros((1,1,1))
ds2.eqsys.f_re.setInitialValue(f,r=[0],p =[0],xi=[0])


# Collision mode
ds2.collisions.collfreq_mode = Collisions.COLLFREQ_MODE_ULTRA_RELATIVISTIC


# Flux limiter
ds2.eqsys.f_re.setAdvectionInterpolationMethod(ad_int=DistFunc.AD_INTERP_TCDF,↩
    ad_jac=DistFunc.AD_INTERP_JACOBIAN_UPWIND)
```

```
# Include synchrotron losses
ds2.eqsys.f_re.setSynchrotronMode(DistFunc.SYNCHROTRON_MODE_INCLUDE)


# Set file name of output file
ds2.output.setFilename(CQ_outname)


# Save settings to file
ds2.save(CQ_settingsname)
```

B.2 SOFT

Below are examples of the SOFT scripts used in this thesis. For the MSE script, only one line-of-sight has been included for brevity.

B.2.1 Synchrotron image and Green's function

```
magnetic_field      = numeric-field;
tools               = rad;
include_drifts      = True;
distribution_function = distFunc;


@MagneticField numeric-field (numeric) {
    filename = "/path/to/magnetic-field-file";
}


@ParticleGenerator PGen {
    a   = 0.0, 1, 100;                  # Normalized minor radius
    p   = 10, 100, 90;                  # (m_ec)
    ithetap = 0.0, 0.35, 40;            # ithetap = pi-thetap
    progress = 100;                     # Print progression info
}


@ParticlePusher PPusher {
    nt = 2000;                          # Resolution parameter
    force_numerical_jacobian = yes;
}


@DistributionFunction distFunc(dream) {
    name = "/path/to/DREAMOutput.h5";
    flippitchsign = yes;
    time = -1;                          # Timestep from which to get the distribution↩
         function
}


@Radiation rad {
    detector = det;
    ignore_trapped = yes;
    ntoroidal    = 7000;                # Resolution parameter
    model        = cone;                # Radiation model to use
    output       = image,green;         # List of outputs
}
```

```
@Detector det {
    aperture     = 1.4e-3;
    position     = -0.886, -4.002, -0.332;
    direction    = -0.503, 0.864, -0.01;
    vision_angle = 0.523 fov;
    spectrum     = 3.0e-6,3.5e-6,40;
}


@RadiationModel cone (cone) {
    emission = synchrotron;
}


@RadiationOutput image (image) {
    pixels = 600;
    output = "image.h5";

}


@RadiationOutput green(green){
    output = "greens.h5";
    format = "r12";
    with_f = yes;
    pixels = 400;
}
```

B.2.2 MSE simulation: the first line-of-sight

```
magnetic_field      = numeric-field;
tools               = rad;
include_drifts      = True;
distribution_function = distFunc;


@MagneticField numeric-field (numeric) {
    filename = "/path/to/magnetic-field-file.h5";
}


@ParticleGenerator PGen {
    a  = 0.0, 1, 50;         # Normalized minor radius
    p  = 50, 160, 100;       # (m_ec)
    ithetap = 0.0, 0.6, 60;
    progress = 100;
}


@ParticlePusher PPusher {
    nt = 2000;               # Resolution parameter
    force_numerical_jacobian = yes;
}


@DistributionFunction distFunc(dream) {
    name = "/path/to/DREAMOutput.h5";
    flippitchsign = yes;
    time = -1;               # Timestep from which to get the distribution ↩
        function
}


@Radiation rad {
    detector = det;
    ntoroidal   = 7000;      # Resolution parameter
    model       = cone;      # Radiation model to use
    output      = green;     # List of configuration of output
    ignore_trapped = yes;
}


@RadiationModel cone (cone) {
    emission = synchrotron;
}


@Detector det {
    aperture = 0.001;
    position = -4.175, 0.830, 0.280;
    direction = 0.62241149269680818, 0.78255742960601515, -0.014415378155204543;
    vision_angle = 0.01 fov;
    spectrum = 660e-9, 660e-9, 1;
}


@RadiationOutput green(green) {
    stokesparams = yes;      # Include Stokes parameters
    output = "MSE_LoS1.h5"
    format = "r12";
    with_f = yes;
    pixels = 400;
}
```